Tin (IV) Oxide Nanostructures: Controlled Synthesis, Properties and Applications in Dye-Sensitized Solar Cells

Dissertation

zur Erlangung des Grades
„Doktor der Naturwissenschaften“
im Promotionsfach Chemie

am Fachbereich Chemie,
Pharmazie und Geowissenschaften der

Johannes Gutenberg-Universität Mainz

Alexander Birkel
geboren in Trier

JOHANNES GUTENBERG UNIVERSITÄT MAINZ

Mainz, 2010

Dekan:	Prof. Dr. [redacted]
1. Berichterstatter:	Prof. Dr. [redacted]
2. Berichterstatter:	Prof. Dr. [redacted]
Tag der mündlichen Prüfung:	11. November 2010

Meinen [redacted] meiner [redacted] und meiner

[redacted] gewidmet.

Die schönsten Erinnerungen sammelt man

immer zu zweit.

The work for this thesis was carried out at the Johannes Gutenberg - University of Mainz and the Seoul National University, Korea in the period between October 15th, 2007 and October 7th 2010, under the guidance of Prof. [redacted] and Prof. [redacted].

Diese Arbeit wurde an der Johannes Gutenberg - Universität Mainz und an der Staatlichen Universität in Seoul, Korea in der Zeit vom 15. Oktober 2007 bis zum 07. Oktober 2010 angefertigt. Die Arbeit wurde von den Professoren [redacted] und [redacted] betreut.

Acknowledgements

First, I would like to thank [redacted] **Prof. Dr.** [redacted] He provided me with a very interesting task for my PhD studies. Additionally, he gave me the guidance and advice I needed during this work. Furthermore, I would like to express my thanks to the *International Research Training Group 1404 - Self-Organized Materials for Optoelectronics* and **Prof. Dr.** [redacted] for the financial support during the last three years. The IRTG made the exchange stay in Seoul possible. I would also like to express my thanks to **Prof.** [redacted] and his group at Seoul National University for hosting me during my stays in Korea. They made working and living there a truly unique experience.

The second biggest thank you is reserved for the members of the Grätzel-mafia a.k.a. Wednesday morning "small-group", [redacted] and [redacted] During our work, we learned a lot from each other (in many, many different fields) and in the end everybody profited from the shared knowledge. Both of them are great labmates and made working in 03-124 a very pleasant experience. Of course, the whole [redacted] is responsible for that as well, each member in his/her own way...

A thank you to **Dr.** [redacted] who taught me a lot about X-ray powder diffraction and the analysis of the obtained data. All of my discussions with him substantially improved my knowledge about this field of science and significantly improved my thesis through both refining the data and crafting effective scientific language..

Many thanks also to the Electron Microscopy Group at the University of Mainz. Here, I would like to thank in particular [redacted] (who should be really happy that microscopy skills outperform his soccer abilities) and also [redacted] Both of them helped me a lot with everything related to TEM. This extends to [redacted] the technician in charge of the EM 420. Whenever there was something wrong with the instrument, he took care of it. Additionally, he was a good tutor when it came to correctly operating the microscope. I would also like to thank [redacted] in the MPI-P as he provided me with some of the SEM images used in chapter 6.

Another thank you to [redacted] who (usually) always measured all my XRD samples, no matter how many, what time and what compound. Although I think other members of the [redacted] caused her even more "trouble" I am sure, she had a lot to do with me research, too.

I would like to express my gratitude to all interns that have worked with me over the course of my PhD. Here, however, in particular [redacted] who has done a lot of beautiful work on the anodic oxidation project. He was always coming up with his own ideas and helped that the project moved on; Not to forget [redacted] who came as a rise student and left as a computer genius although, according to him, I did not teach him anything. Thank you anyway.

Many thanks also to [redacted] who (as Prof. [redacted]) helped me with anything related to official paperwork. She was a good source of advice, especially outside the realm of science.

This thank you extends to [redacted] and [redacted] from the IRTG office for their help and support for our exchange stay in Seoul.
Also: Thank you very much to [redacted] from the MAINZ coordination office. He was always very helpful when it came to "bureaucracy" or anything else concerning the *Graduate School of Excellence MAINZ*. I bet he is happy now that I cannot bring him any more "Reiseaufträge" because the final payment of those related to the [redacted] were usually complicated, to say the least.

Thank you to [redacted] who was in charge of all the measurements of the solar cells in Seoul. He is probably the biggest Korean guy in his group, not just in size but also scientific abilities. Working with him was a real pleasure and made the 75 minute journey (one-way) from SNU to Hanyang University worth the trip.

A huge [redacted] thanks to [redacted] our good friend from Seoul. Not only did we have the most fun with her, going out in Hongdae, but she also is responsible for the translation of the abstract into Korean. Oh, and her boyfriend [redacted] is also a nice guy.

[redacted]; he provided me with a lot of useful suggestions and is probably the greatest VfB Stuttgart-fan alive. But despite this problem, he is also very good when it comes to crystallography and also helped me many times with problems related to that.

I would like to thank [redacted] (as my mentor) and [redacted] for their continuous support and help over the last years.

Finally I want to thank **my** [redacted], especially [redacted]. They have been a great support during my dissertation although I doubt that any member of my family remotely knows what I have been doing.

Last but of course not least: my girlfriend-turned-fiancée-turned-wife [redacted] who not only was a great personal help, but also a great partner to talk (and argue) about science and lab attitude with. I am looking forward to the many years to come that we can spend together!

For I dipt into the future, far as
human eye could see,
saw the visions of the world and all
the wonder that would be.

Lord Alfred Tennyson

Contents

Abstracts

Abstract - English

Among the most studied topics in modern chemistry, nanoparticles play a dominating role. Due to their broad range of applications, the need for tailor-made materials is greater than ever. Therefore, a profound and detailed understanding of the synthesis and growth processes that lead to nanostructures is necessary. Only with this knowledge, reliable preparation-protocols are available and open the path to the desired nanomaterials in bulk amounts. The work presented in this thesis focuses on this challenge with special attention given to the synthesis and characterization of SnO_2 nanomaterials.

In **chapter 2**, it has been examined how a simple change in precursor cation (i.e. replacing Na^+ with Li^+, K^+, Rb^+, Cs^+, TMAH and NH_4^+) used in a template-free, solvothermal preparation of SnO_2 nanoparticles drastically changes the morphology of the resulting products. With a combination of molecular dynamics simulations and careful transmission electron microscopy investigations, a relationship between the adsorption energies of the different cations onto certain crystal faces of SnO_2, the reaction temperature and the observed morphology is established.

Additionally, **chapter 3** demonstrated that $SnO_2/Na_2Sn(OH)_6$ "core-shell" nanorods can be fabricated in a simple one-step reaction.

After it has become more plausible how the growth of anisotropic SnO_2 nanostructures can be managed on solvothermal conditions, **chapter 4** deals with the investigation of the formation of SnO_2 nanorods, obtained during a microwave-assisted solvothermal reaction. Microwave preparations offer drastically decreased reaction times, due to the very short heating times and ramps. By performing a careful time-dependent study, X-ray powder diffraction data and high-resolution transmission electron microscopy investigations provided a much more detailed insight into the actual growth process of the nanorods. Finally, a morphological reaction scheme is presented.

A combination of the results obtained in the previous chapters is presented in **chapter 5**. Here, with the use of different precursor cations in a microwave-assisted synthesis, a variety of nanostructures, ranging from purely anisotropic materials (SnO_2 nanorods) to purely isotropic spheres, have been prepared. Subsequently, a very easy and cheap way to incorporate these particles into a paste was developed. This paste can then be used to prepare semiconducting photoanodes for a dye-sensitized solar cell, applying the so-called "doctor-blading" technique. Electron microscopy was used to investigate the particle morphology and the quality of the sintered SnO_2 films. BET measurements helped to determine the surface area of the various nanostructures. The characteristics of the solar cell device were investigated in strong collaboration with Seoul National University, Korea. Solar cells with efficiencies reaching 2.8% could be fabricated and a link between the particle morphology, the paste-preparation process and the performance of the cell was proposed.

In addition to the investigations of the controlled solvothermal syntheses of SnO_2 nanorods, the search for porous structures or, as a next step, ordered arrays of one-dimensional tubes, consisting of SnO_2 is of great interest; **Chapter 6** summarizes the work done in this area of research. As a first step, commercially available tin foil was successfully smoothed using a multi-step electropolishing procedure. Subsequently, different reaction parameters were varied systematically and the observed structures were characterized using laser microscopy and scanning electron microscopy. The search for the optimum conditions to obtain ordered, porous SnO_2 films is the topic of ongoing research.

To summarize, a more detailed insight into the factors which control the growth of SnO_2 nanomaterials shall be gained and the performance of some of those materials in dye-sensitized solar cells is investigated. Additionally, electrochemical pathways to obtain porous SnO_2 nanostructures were investigated as a first step in the search for ordered arrays of SnO_2 nanotubes.

Abstract - Korean

초록

현대 화학에서 뜨거운 이슈인 것 중 하나가 나노입자에 관한 것이다. 나노입자는 활용 영역 또한 넓기 때문에 맞춤물질 합성에 대한 연구가 활발히 이루어지고 있다. 따라서, 나노구조체를 만드는 합성법과 나노구조체의 형성 과정에 대해 이해하는 것이 중요하다. 본 논문은 SnO_2 나노입자의 합성 및 특성 분석에 대해 서술한 것이다.

제 3장에서는 템플레이트를 사용하지 않고 전구체의 양이온(예를 들면 Na^+를 Li^+, K^+, Rb^+, Cs^+, TMAH, NH_4^+로 대체)만 간단하게 바꿔서 SnO_2 나노입자를 합성하면 입자의 형태가 급격히 바뀐다는 것을 확인하였다. 분자 동역학 시뮬레이션과 투과전자현미경 분석을 통해 SnO_2 결정 표면 위의 각각 다른 양이온의 흡수에너지와 반응온도, 관찰된 형태 사이의 관계를 알 수 있었다.

제 4장에서는 $SnO_2/Na_2Sn(OH)_6$로 이루어진 코어-쉘 나노로드를 간단한 한 단계 반응을 통해 합성하였다.

제 5장에서는 이방성 SnO_2 나노구조체가 어떻게 성장하는지에 대한 연구를 수행하고, 용매열합성을 통해 형성되는 SnO_2 나노로드에 대한 특성을 분석하였다. 용매열합성은 열처리 온도와 반응 패스가 아주 짧기 때문에 반응 시간을 급격히 단축시킬 수 있었다. 시간-의존성 연구와 분말 엑스선 회절 분석, 고배율 투과전자현미경 분석을 통해 나노로드의 구체적인 성장 과정을 관찰하였으며, 형성 과정에 대한 모식도를 제시하였다.

제 6장에는 앞 장에서의 연구결과를 정리하였다. 극초단파를 이용한 합성에서 각각 다른 전구체 양이온의 사용으로 순수한 이방성 모양(SnO_2 나노로드)부터 순수한 등방성의 모양까지 다양한 나노구조체를 합성할 수 있었다. 또한 이러한 입자를 페이스트 형태로도 쉽고 저렴하게 만드는 방법을 개발하였다. 페이스트는 닥터-블레이딩 기술을 통해 염료 감응 태양전지의 반도체 광음극을 만들 때 필요한 형태이므로 중요한 연구이다. 입자의 형태와 신터링 된 SnO_2 필름의 질을 전자현미경을 통해 관찰하였으며, 다양한 나노구조체의 비표면적을 BET 측정을 통해 조사하였다. 태양전지 소자의 특성분석은 한국의 서울대학교와 공동연구를 통해 진행하였다.

개발된 태양전지는 2.8%의 효율을 나타내는 것을 확인하였으며, 입자 형태와 페이스트 형성 과정, 전지 성능 간의 관계를 제시하였다.

용매열합성으로 형성된 SnO_2 나노로드에 대한 연구와 더불어, SnO_2로 이루어진 다공성 구조나 1차원으로 정렬된 배열에 대한 연구도 진행하였으며, 그 결과를 제 7장에 요약하였다. 우선, 시판되고 있는 틴 포일(tin foil)을 여러 단계의 전자연마 과정을 통해 매끄럽게 만들었다. 그 후, 반응 파라미터들을 체계적으로 다양하게 조절하여 반응시켰으며, 레이저 현미경과 주사전자현미경을 통해 구조를 관찰하였다. 정렬된, 다공성의 SnO_2 필름을 생산하기 위한 반응조건을 최적화 시키는 실험은 진행 중이다.

요약하면, 본 연구에서는 SnO_2 나노구조체의 성장을 조절하는 요소와 SnO_2 소재가 염료 감응 태양전지에 사용되었을 때의 성능에 대한 연구를 구체적으로 진행하였다. 또한 정렬된 배열의 SnO_2 나노튜브를 생산하기 위한 첫 단계인 다공성 SnO_2 나노구조체를 전기화학적 방법을 통해 개발하였다.

Zusammenfassung - Deutsch

Für viele Anwendungen von Nanomaterialien sind maßgeschneiderte Produkte wünschenswert, weswegen ein tiefgreifendes und genaues Wissen der Reaktionsabläufe, die zu diesen Produkten führen, unabdingbar ist. Um dies im Fall von SnO_2 zu erreichen, behandelt diese Arbeit die kontrollierte Synthese und genaue Charakterisierung von Nanopartikeln von Zinn(IV) Oxid.

Kapitel 2 beschreibt, wie das gezielte Austauschen eines Kations in einer Solvothermal-Synthese die Morphologie der erhaltenen Partikel drastisch verändern kann. Hierfür wurden Molekular Dynamik-Simulationen und umfangreiche Elektronen-mikroskopische Untersuchungen durchgeführt. Es konnte ein Zusammenhang zwischen den Adsorptionsenergien der Kationen auf exponierten Kristallflächen der erhaltenen Nanopartikel und der entstandenen Morphologie nachgewiesen werden. Zusätzlich wurde in **Kapitel 3** eine „Eintopfreaktion“ von $SnO_2/Na_2Sn(OH)_6$ „Kern-Schale“ Materialien betrachtet.

In **Kapitel 4** wird der Wachstums-Prozess von SnO_2 Nanostäben genauer beleuchtet. Mit Hilfe einer Mikrowellen-Reaktionstechnik, die sehr kurze Heiz- und Abkühlzeiten erlaubt, konnte der morphologische Reaktionsablauf genauer aufgeklärt werden: Das Wachstum startet von kristallinen, anisotropen Strukturen und schreitet solange schnell voran, wie ein Reservoir bestehend aus amorphem SnO_2 vorhanden ist. Es konnte gezeigt werden, dass nach Aufbrauchen dieses Reservoirs nur noch Um- und Rekristallisierungvorgänge stattfinden, bis die endgültige Form der Stäbe erreicht ist. Die spektroskopischen Eigenschaften der Nanostäbe in den einzelnen Wachstumsstufen wurden untersucht.

Die Anwendung der SnO_2 Partikel in Farbstoffsolarzellen ist das Thema von **Kapitel 5**. Durch das in den vorhergehenden Kapiteln gewonnene Wissen, konnten Nanopartikel mit verschiedenen Morphologien in einer einfachen und energiesparenden Mikrowellen-Synthese hergestellt werden. Anschließend wurden diese Partikel als Anodenmaterial in Farbstoffsolarzellen getestet. Es konnten Effizienzen von bis zu 2.8% erreicht werden. Dies ist einer der höchsten Werte, die für Zellen auf Basis von SnO_2 Nanopartikeln bis jetzt gemessen wurden, was für die hohe Qualität der Partikel und der Solarzellenherstellung spricht.

Eine andere Art von Synthese von SnO_2 Nanostrukturen wird in **Kapitel 6** beschrieben. Es sollten mit Hilfe von elektrochemischen Reaktionswegen, (selbst-organisierte) geordnete Felder von Nanoröhren hergestellt werden. Hier konnte eine einfache Methode zur Elektropolitur von Zinn erarbeitet werden. Weiterhin wurden erste poröse Filme hergestellt, jedoch ist die Optimierung der Reaktionsbedingungen zur Synthese geordneter Strukturen das Thema laufender Forschungsarbeiten.

Zusammenfassend lässt sich sagen, dass ein genauerer Einblick in die Faktoren, die das Wachstum und die Morphologie von SnO_2 Nanomaterialien bestimmen, gewonnen werden konnte. Die Güte dieser Substanzen als Anodenmaterialien in Farbstoffsolarzellen wurde untersucht, wobei bisher kaum erreichte (in Solarzellen basierend auf unmodifiziertem SnO_2) 2.8% Effizienz beobachtet worden sind. Zusätzlich wurde ein erster Schritt auf dem Weg zur elektrochemischen Synthese geordneter Felder von porösen Zinn(IV) Oxid Nanostrukturen gemacht.

1 Introduction

In this chapter, a brief overview of the general interest in solar cells and in particular dye-sensitized solar cells will be given. The material that has been studied in this work, i.e. SnO_2 will shortly be introduced. To conclude, the motivation and task for this thesis work is presented.

1.1 General Interest

The quest for replacements of fossil fuels is the ultimate goal that motivates a great number of material scientists [1]. The search for new materials that are capable of helping to create a new "energy-landscape" is one of the biggest challenges of the forthcoming years. The growth of our industries and societies cannot rely on the endless abundance of natural resources such as oil, gas and coal. Especially with the so-called peak oil, i.e. the year with the maximum production of oil, coming closer and closer, the urge for a replacement of carbon-based energy sources is crucial. To further limit (or eventually even decrease) pollution and with that hopefully the (potential) anthropogenic influence on the earths climate, a drastic change to alternative power sources is necessary. Opportunities for a change in energy production and consumption

lie in many fields. Firstly, and most easily, each person can try to consume less power. Optimizations of electrical grids and decentralized power creation are further options. However, especially with an expected growth of both, population and prosperity of the world, there is an increasing need for energy.

Possible alternative or regenerative energy sources include hydroelectricity (although here other issues arise), wind and biogas energy production. Another promising part of the solution of the energy problem are solar cells, i.e. devices that transform light energy directly into electrical energy. Although their share of the total energy production [2] is still only slightly above 1% in Germany (worldwide even less), this field has seen a dramatic increase over past years, mostly (at least in Germany) due to subsidation by the government. For the future, an impressive growth rate of more then 40% is predicted, helping to make solar cells a cheaper option than they are as of today. This is due to the fact that with increasing demand, the production costs can decrease faster.

Among the many varieties of solar cells, one can find silicon (amorphous [a-Si], poly-crystalline [pc-Si] and single-crystalline [sc-Si]) solar cells, thin film cells, such as CdTe or CIGS ($Cu(In,Ga)(S,Se)_2$) and organic photovoltaic cells. All of them rely on the principle of a p-*pn-junction*-n-type architecture. In all cases, the generation and transport of the carriers takes place in the same material.

1.1.1 Dye-Sensitized Solar Cells

A very promising part of the large field of organic cells are photoelectrochemical cells. The most popular one is the dye-sensitized solar cell, or "Grätzel"-Cell [3], named after the inventor Michael Grätzel. Although the concept this type of cells are using (i.e. mimicking photosynthesis) has been explored before,[1] it was the paper from Michael Grätzel and his co-worker Brian O´Regan [3] in 1991 that initialized a run onto these types of cells. Ever since, the number of publications and patents related to this topic has increased. The breakthrough of Grätzel was to achieve unprecedented efficiencies of $\sim 7\%$. This was made possible through the combination of a nanoscale porous TiO_2 layer sensitized with a ruthenium-based dye, sintered on top of a transparent conductive oxide layer [4].

1.1.1.1 Principle of Operation

The basic principle of operation of a dye-sensitized solar cell is the creation of electricity due to the absorption of a photon by a dye and subsequent transfer of an electron from the excited state into the conduction band of a semiconductor. A typical dye-sensitized solar cell consists of the following important parts:

- Two sheets of glass that are coated with a transparent conductive layer. The materials most widely used are ITO and FTO, see below.

- A working electrode (the anode), consisting of one of the two glass sheets, a nano-porous layer of semiconducting material, such as TiO_2 or SnO_2. This semiconductor is sensitized by (a monolayer of) a dye that absorbs in the desired wavelength range.

[1] It was as early as 1977 when the first patent has been filed that included all the characteristics of todays cells. It was called dye-sensitized solar cell.

- An electrolyte to close the electrical circuit with the counter electrode and to regenerate, i.e. to reduce the (oxidized) dye after electron injection. Most electrolytes consist of a redox couple dissolved in an organic matrix.

- The counter electrode, consisting of the second sheet of glass. Often, a thin layer of platinum is used as the cathode.

1.1.1.2 Transparent Conductive Oxide

The requirements for the conductive glass are a high conductivity to ensure the collection and transport of all carriers that are created as well as good thermal stability. The most widely used TCOs are ITO which stands for **i**ndium **t**in **o**xide and FTO, which is **f**luorine-doped **t**in **o**xide. Although ITO is superior in terms of conductivity, it is far more expensive and does not have the same thermal stability and processability that FTO possesses.

1.1.1.3 Semiconducting Layer

The most prominent material, that still shows the highest efficiency values is nanostructured TiO_2 [5–7]. Promising alternatives are ZnO [8, 9], Nb_2O_5 [10, 11] and SnO_2 [8, 12]. It is desirable to achieve the highest surface area possible since the dye adsorption increases with increasing area. However, a major drawback of nanoporous anode-materials, consisting of smaller particles, are the inefficient electron percolation-pathways towards the electrode. Oriented anisotropic structures, such as wires and rods, that exhibit defined electron passageway, are promising emerging materials to counter that issue [13–15].

1.1.1.4 Dye

The dye is perhaps the most interesting part of the dye-sensitized solar cell because it is not only responsible for the photosensitization, it also gives this type of solar cells some unique properties like a tunable color. In addition to this (possible) aesthetic advantage, the dye must of course fulfill other straight forward requirements, such as good adsorption behavior to the semiconductors surface, a broad absorption spectrum, a low toxicity and of course an outstanding long-term stability [16, 17]. Up to date, the most efficient dyes are the so called *black dye* and other ruthenium based pyridyl complexes, such as N3 ($RuL_2(NCS)_2$; L = 2,2'-bipyridine-4,4'- dicarboxylic acid) and N719 ($RuL_2(NCS)_2$:$(TBA)_2$; L = 2,2'-bipyridine-4,4'- dicarboxylic acid, TBA = Tetrabutylammonium). Their structures are shown in Figure 1.1, taken from Ref. [18].

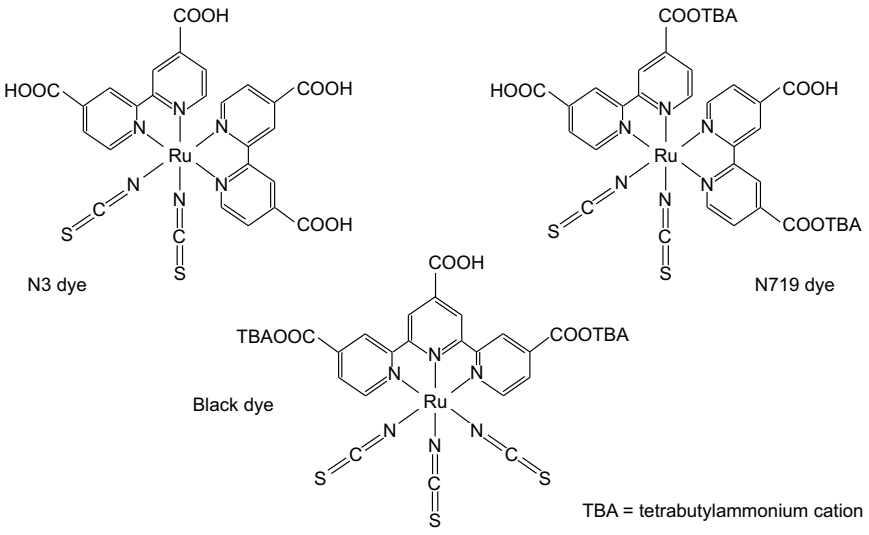

Figure 1.1: Various ruthenium-based dyes

1.1.1.5 Electrolyte

In liquid-type cells, the most common electrolytes are based on the I^-/I_3^- redox couple, usually dissolved in an organic solvent (e.g. acetonitrile). Although other alternatives (such as $(SeCN)_2/SeCN^-$ or $(SCN)_2/SCN^-$) have been examined [4, 16], the iodide as the reduced species and the triiodide (I_3^-) as the oxidized species still yield the highest efficiencies in liquid type cells. All solid-state dye-sensitized solar cells make use of holeconducting layers instead of a liquid electrolyte.[2]

The process of current generation works as follows:

- An incoming photon is absorbed by a dye-molecule and thus promoting an electron to an excited state.

- The dye in the excited state injects an electron into the conduction band (CB) of the used semiconductor. Undesirable sidereactions include non-radiative relaxation processes and reactions with e.g. the electrolyte.

- The electron travels through the network of semiconducting particles. Once it has reached the electrode, it can enter an electric circuit (E) and carry out electrical work.

- At the counter electrode (CE, the cathode), an electron reduces the redox couple (Red/Ox) that is included in the electrolyte.

- The reduced redox species transfers its electron to the positively charged dye, with that re-reducing the dye and getting oxidized itself.

[2]For a much more detailed description of the building parts, as well as the operating mechanism of a dye-sensitized solar cell please refer to Reference [4, 16] as they provide an excellent overview of the most important features of these devices.

It becomes evident, that through the redox cycle, there is solar energy converted into electrical energy without any net change in chemical composition. The overall reaction scheme can be expressed as follows:

$$\mathrm{h}\nu + \mathrm{Dye} \rightarrow \mathrm{Dye}^*$$

$$\mathrm{Dye}^* \rightarrow \mathrm{Dye}^+ + \mathrm{e}^- \ (\mathrm{CB})$$

$$\mathrm{e}^- \ (\mathrm{E}) \rightarrow \mathrm{e}^- \ (\mathrm{CE}) + \mathrm{Electrical\ Work}$$

$$\mathrm{Ox} + \mathrm{e}^- \rightarrow \mathrm{Red}$$

$$\mathrm{Red} + \mathrm{Dye}^+ \rightarrow \mathrm{Ox} + \mathrm{Dye}$$

$$\mathbf{h\nu \rightarrow Electrical\ Work}$$

1.1.2 J-V Characteristics of Dye-Sensitized Solar Cells

To describe the performance, i.e. the efficiency, of a solar cell the following values are of interest [19]:

A solar cell delivers power in the bias range from 0 to V_{oc}. In between these values, the power density of the cell is given by equation 1.1, where P represents the power, J and V represent the current density and the voltage respectively:

$$P = JV \tag{1.1}$$

The maximum of P (the maximum power point) is defined as the point where the product of J and V reaches the largest value, therefore this voltage and current density are referred to as J_m and V_m.

A quantity to describe the goodness of a cell is related to P_m and the open circuit voltage V_{oc} as well as the short circuit current J_{sc}. It is called the *fill factor* and given by equation 1.2:

$$FF = \frac{V_m J_m}{V_{oc} J_{sc}} \tag{1.2}$$

The higher the fill factor, the closer a J-V curve is to the optimum, see Figure 1.2.

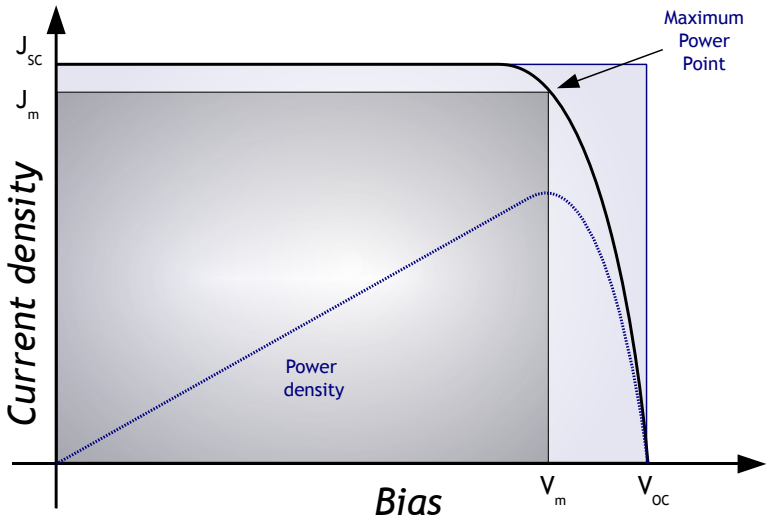

Figure 1.2: The J-V characteristics of a solar cell.

Finally, the efficiency of a cell is defined as the ratio of the power obtained at P_m and the incident light power:

$$\eta = \frac{P_{out}}{P_{in}} = \frac{V_m J_m}{P_{in}} = \frac{V_{oc} J_{sc} FF}{P_{in}} \tag{1.3}$$

It becomes evident that the four most important quantities are the open circuit voltage V_{oc}, the short circuit current J_{sc}, the fill factor FF and above all the efficiency η. To achieve a better comparability, standardized test conditions for measurements are common [20]. Please refer to chapter 5 for details.

1.2 Tin(IV) Oxide

The material of choice in this work was tin (IV) oxide. It is a wide (direct) band-gap, n-type semiconductor with a bandgap of $\sim 3.6\,\mathrm{eV}$ [21] at room temperature.

1.2.1 Structural Properties

The mineral form of SnO_2 is called cassiterite (in German, common names are *Kassiterite* or *Sperlingschnabel*). Cassiterite has its name derived from the term *Cassiterides* which means "islands off the western coast of Europe" in pre-Roman times (the exact location of these "islands" has been hotly debated over the years, current thought is that the source was probably mainland Spain and that even 2000 years ago, traders had a habit of providing misleading locality information to protect their sources)[3].

SnO_2 crystallizes in the tetragonal space group $P4_2/mnm$ with the lattice parameters being $a = 4.73820$ Å and $c = 3.18710$ Å. The unit cell contains two tin cations and four oxygen anions. The Sn^{4+} cations are coordinated by six O^{2-} - anions, forming slightly distorted octahedra, whereas the oxygens are surrounded by three tin ions, forming an almost regular triangle, see Figure 1.3. The SnO_6 - octahedra are connected by common vertices in the ab-plane and by common edges in the [001] direction. The electronic structure [21–23] of SnO_2, which is a key feature for optoelectronic applications, of both the bulk and several distinct surfaces has been investigated in great detail.. Figure 1.4 shows graphs of the band-structure (a) and the density of states (b) of SnO_2.

[3]Taken from: *www.mindat.org*, 2010

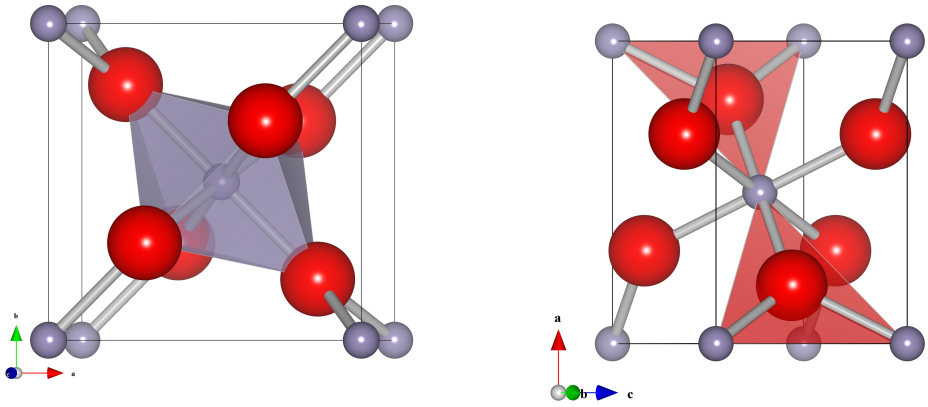

(a) **(b)**

Figure 1.3: The unit cell and coordination polyhedra of SnO_2. (a) Octahedral coordination of the tin cations; (b) Triangle around the oxygen anions.

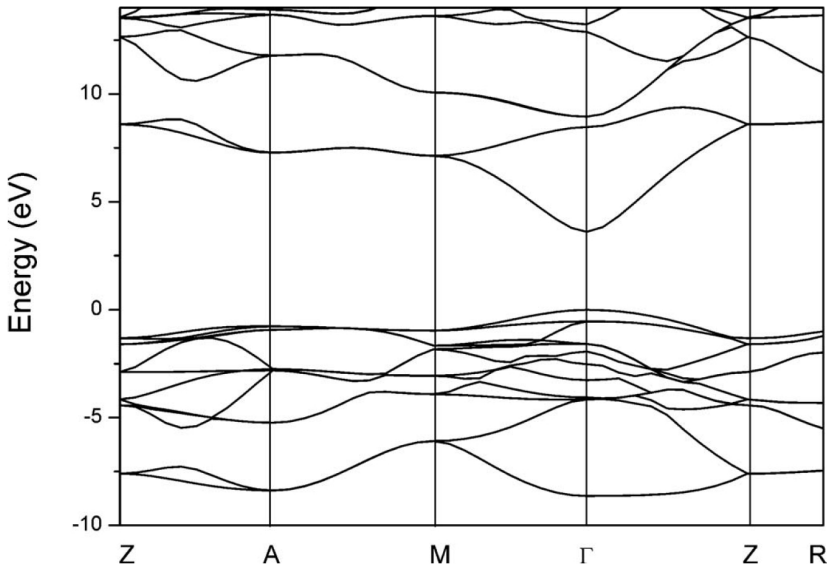

(a)

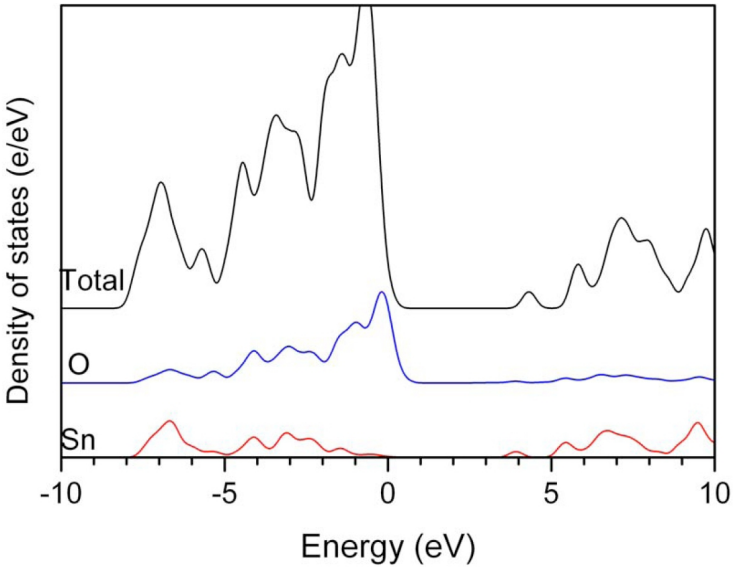

(b)

Figure 1.4: Band-structure and density of states (DOS) of SnO_2. Taken from Ref. [21]

1.3 Aims of the Project

The solvothermal, template-free synthesis of nanoparticles is very often a "black box" that does not allow any insight into the reaction mechanism or intermediate products, either chemically or morphologically. It is therefore of great importance to fully understand the parameters that influence the growth and the final morphology during this type of reaction. To gain further understanding, careful considerations of all reaction conditions is necessary. This is the exact objective target of this work:

With the help of extensive X-ray diffraction and electron microscopy studies, it shall be revealed how one can tune the morphology of SnO_2 nanomaterials. Therefore, careful parameter-dependent studies on the solvothermal and electrochemical syntheses of SnO_2 nanomaterials need to be carried out. Once it has become clear how to tune the morphology of the obtained nanoparticles, a more detailed insight into the morphological evolution of anisotropic nanostructures would be desirable. This can be achieved with the help of a microwave-reactor, due to the very fast heating and cooling times that are possible.

As a next step, the synthesized, now tailor-made materials will be used as the anode material of a dye-sensitized solar cell. Their performance depending on the morphology and the reaction pathway shall be investigated. This will be embedded in a collaboration with the group of Prof. K. Char (Seoul National University, Korea), supported by the *International Research Training Group 1404*.

References

[1] M. S. Dresselhaus and I. L. Thomas. Alternative energy technologies. *Nature*, 414(6861):332–337, 2001.

[2] Naturschutz und Reaktorsicherheit (BMU) Bundesministerium für Umwelt. Erneuerbare Energien in Zahlen. 2010.

[3] B. O'Regan and M. Grätzel. A low-cost, high-efficiency solar cell based on dye-sensitized colloidal TiO_2 films. *Nature*, 353(6346):737–740, 1991.

[4] A. Hagfeldt, G. Boschloo, L. Sun, L. Kloo, and H. Pettersson. Dye-Sensitized Solar Cells. *Chemical Reviews*, 2010.

[5] M. Grätzel. Photoelectrochemical cells. *Nature*, 414(6861):338–344, 2001.

[6] M. Grätzel. Dye-Sensitized Solar Cells. *Journal of Photochemistry and Photobiology C-Photochemistry Reviews*, 4(2):145–153, 2003.

[7] M. Grätzel. Solar Energy Conversion by Dye-Sensitized Photovoltaic Cells. *Inorganic Chemistry*, 44(20):6841–6851, 2005.

[8] K. Tennakone, G. R. A. Kumara, I. R. M. Kottegoda, and V. P. S. Perera. An efficient dye-sensitized photoelectrochemical solar cell made from oxides of tin and zinc. *Chemical Communications*, (1):15–16, 1999.

[9] M. Law, L. E. Greene, J. C. Johnson, R. Saykally, and P. Yang. Nanowire dye-sensitized solar cells. *Nature Materials*, 4(6):455–459, 2005.

[10] K. Sayama, H. Sugihara, and H. Arakawa. Photoelectrochemical Properties of a Porous Nb_2O_5 Electrode Sensitized by a Ruthenium Dye. *Chemistry of Materials*, 10(12):3825–3832, 1998.

[11] F. Lenzmann, J. Krueger, S. Burnside, K. Brooks, M. Grätzel, D. Gal, S. Rühle, and D. Cahen. Surface Photovoltage Spectroscopy of Dye-Sensitized Solar Cells with TiO_2, Nb_2O_5, and $SrTiO_3$ Nanocrystalline Photoanodes: Indication for Electron Injection from Higher Excited Dye States. *Journal of Physical Chemistry B*, 105(27):6347–6352, 2001.

[12] M. K. I. Senevirathna, P. Pitigala, E. V. A. Premalal, K. Tennakone, G. R. A. Kumara, and A. Konno. Stability of the SnO_2/MgO dye-sensitized photo electrochemical solar cell. *Solar Energy Materials and Solar Cells*, 91(6):544–547, 2007.

[13] S. Gubbala, V. Chakrapani, V. Kumar, and M. K. Sunkara. Band-Edge Engineered Hybrid Structures for Dye-Sensitized Solar Cells Based on SnO_2 Nanowires. *Advanced Functional Materials*, 18(16):2411–2418, 2008.

[14] D. Kim, A. Ghicov, S. P. Albu, and P. Schmuki. Bamboo-Type TiO_2 Nanotubes: Improved Conversion Efficiency in Dye-Sensitized Solar Cells. *Journal of the American Chemical Society*, 139(49):16454–16455, 2008.

[15] V. V. Kislyuk and O. P. Dimitriev. Nanorods and nanotubes for solar cells. *Journal of Nanoscience and Nanotechnology*, 8(1):131–148, 2008.

[16] L. M. Gonçalves, V. d. Z. Bermudez, H. A. Ribeiro, and A. M. Mendes. Dye-sensitized solar cells: A safe bet for the future. *Energy & Environmental Science*, 1(6):655–667, 2008.

[17] Y. Ooyama and Y. Harima. Molecular Designs and Syntheses of Organic Dyes for Dye-Sensitized Solar Cells. *European Journal of Organic Chemistry*, 2009(18):2903–2934, 2009.

[18] M. Ryan. PGM Highlights: Ruthenium Complexes for Dye Sensitised Solar Cells. *Platinum Metals Review*, 53:216–218(3), 2009.

[19] J. Nelson. *The Physics of Solar Cells*. Imperial College Press, London, 2007.

[20] G. P. Smestad, F. C. Krebs, C. M. Lampert, C. G. Granqvist, K. L. Chopra, X. Mathew, and H. Takakura. Reporting solar cell efficiencies in Solar Energy Materials and Solar Cells. *Solar Energy Materials and Solar Cells*, 92(4):371 – 373, 2008.

[21] B. Falabretti and J. Robertson. Electronic structures and doping of SnO_2, $CuAlO_2$, and $CuInO_2$. *Journal of Applied Physics*, 102(12):123703–1, 2007.

[22] Y. Watanabe, H. Endo, H. Semba, and M. Takata. Electronic structure and optical non-linearity of tin oxide thin films. *Journal of Non-Crystalline Solids*, 178:84 – 90, 1994. Proceding of the First PAC-RIM Meeting on Glass and Optical Materials.

[23] I. Manassidis, J. Goniakowski, L. N. Kantorovich, and M. J. Gillan. The structure of the stoichiometric and reduced $SnO_2(110)$ surface. *Surface Science*, 339(3):258 – 271, 1995.

2

Interaction of Alkaline Metal Cations with Oxidic Surfaces: Effect on the Morphology of SnO_2 Nanoparticles

2.1 Abstract

Reaction pathways to SnO_2 nanomaterials through the hydrolysis of hydrated tin tetrachloride precursors were investigated. The products were prepared solvothermally starting from hydrated tin tetrachloride and various (e.g. alkali) hydroxides. The influence of the precursor base on the final morphology of the nanomaterials was studied. X-ray powder diffraction data (XRD) indicated the formation of rutile-type SnO_2. Transmission electron microscopy (TEM) studies revealed different morphologies that were formed with different precursor base cations. Data from Molecular Dynamics (MD) simulations provide theoretical evidence that the adsorption of the cations of the precursor base to the faces of the growing SnO_2 nanocrystals is crucial for the morphology of the nanostructures.

2.2 Introduction

Tin (IV) dioxide (SnO_2) is a semiconducting material with a band gap of 3.6 eV at 300 K [1]. It is of considerable technological importance with a number of applications, especially for combustible and toxic gas detection, thin film coatings and sensor devices [2–7]. The basis of the sensor application is the modification of the conductivity of the metal oxide by adsorption of gases from the atmosphere. In this process, the conductivity of the material may be enhanced by introducing carriers into SnO_2, either by doping or by oxygen deficiency [8]. Indeed, the material shows high quasimetallic electrical conductivity but retains good optical transparency in the visible region [9, 10]. These properties can be used for transistors [11], or photovoltaic devices [12–14]. As many of these applications depend on the surface area and the chemisorption of gas molecules, a specific particle size and/or morphology is desired. Therefore synthetic pathways for preparing nanowires [15–17], -rods [18–21], or -tubes [22] have been devised using sol-gel [23, 24], thermal evaporation [17], template-assisted methods (such as micro emulsions) [21], laser ablation [25], magnetron sputtering [26], microwave irradiation processes [27–29], hydrothermal [30–35] or nonaqueous procedures [36].

Although the preparation of SnO_2 by hydrolysis of hydrated tin (IV) chloride has been reported before [37], a controlling effect of the precursor base cation has neither been observed nor considered so far, whereas for metals or ionic compounds the addition of extraneous ions or molecules is known to lead to pronounced changes in the crystal morphology [38]. In particular for ionic crystals such as $CaCO_3$ such morphology modification by anionic [39], neutral [40–42] or cationic [43–45] surface species has been reported. These changes can be rationalized in terms of binding of the additive to specific crystal faces, which influences the growth rates accordingly. Typically, the morphology change by cationic modifiers is caused by substituting the cations of the

"host" lattice by the cations of the growth modifier. For oxide nanoparticles, that are typically formed by polycondensation, cation substitution is rarely observed, and well defined colloidal particles are obtained in the presence of anionic (e.g. phosphate for α-Fe_2O_3) [46] or neutral surfactants (e.g. formamide for SnO_2) [47]. In this chapter, it will be demonstrated by varying the precursor base, that the cations are not merely spectator species in the polycondensation reaction of hydrated $SnCl_4$ with alkali bases, but rather play a crucial role during the formation of the nanorods. The experimental data are supported by results from Molecular Dynamics (MD) simulations.

2.3 Experimental

2.3.1 Materials

All starting materials were used without further purification or treatment. $SnCl_4 \cdot 5\ H_2O$ (98%) was purchased from Sigma Aldrich. $LiOH \cdot H_2O$ (99%, Aldrich), NaOH (99%, Aldrich), KOH (90%, Aldrich), $RbOH \cdot n\ H_2O$ (Sigma-Aldrich) and $CsOH \cdot H_2O$ (96%, ABCR) were used in solid form. Tetramethylammoniumhydroxide (25% w/w in water, Aldrich) and NH_4OH (25%, Aldrich) were used from solution.

2.3.2 Sample Preparation

SnO_2 nanoparticles were prepared using a solvothermal technique, modifying a reaction pathway reported before [20]. In a typical synthesis, 3.5 ml of 0.5 M aqueous $SnCl_4$ solution and 3.5 ml of 5 M base (except TMAH, here, due to the lower concentration, 6.25 ml were used) in water were mixed together with 25 ml of a water/ethanol mixture in the ratio 1:1. After several minutes of stirring the reaction mixture was transferred into a 50 ml Teflon vessel and finally sealed in a hydrothermal autoclave. The autoclave was heated to 200°C or 250°C, respectively, for 24 hours and allowed to cool down to room temperature radiatively. The resulting white-gray powder was separated by centrifugation (9000 rpm) and washed several times with water and ethanol. Finally, the powder was dried at 75°C overnight.

2.3.3 Characterization

Electron Microscopy

The products were characterized by means of transmission electron microscopy (TEM) using a Philips 420 instrument with an acceleration voltage of 120 kV or a Philips TEC-

NAI F30 electron microscope (field-emission gun, 300 kV extraction voltage) equipped with an Oxford EDX (energy-dispersive X-ray) spectrometer with a Si/Li detector and an ultrathin window for elemental analysis. Samples for TEM measurements were prepared from ethanolic suspensions of the samples. A few drops of the ultrasonicated suspension were administered onto a Cu grid coated with an amorphous carbon layer.

X-ray Powder Diffraction

X-ray diffraction patterns (XRD) were recorded using a Bruker AXS D8 Discover powder diffractometer (CuKα radiation, graphite monochromator) equipped with a 2D HiStar detector and a Siemens D5000 with CuKα_1 radiation (Ge (220) monochromator) and a Braun M50 position sensitive detector. Phase analyses were performed according to the PDF-2 using Bruker AXS EVA 10.0 [48]. Crystallites sizes, intensity alterations due to preferred orientation and anisotropic reflection profile broadening due to anisotropic morphologies were determined by means of LeBail fits [49] and Rietveld refinements, respectively, applying the fundamental parameter approach using TOPAS Academic V1.0 [50].

Molecular Dynamics Simulations

The geometry optimization and molecular dynamics simulations were carried out with the Materials Studio 4.4 program package from Accelrys [51]. SnO_2 surfaces were prepared by cleaving a SnO_2 unit cell (ICSD-52151). A depth of 5 layers was chosen to simulate the bulk properties. To provide enough room for the ions and to prevent ghost interactions due to the periodic boundary conditions, a supercell of this slab was built with lattice parameters of about 30 x 30 Å^2. The positions of Sn^{4+} and O^{2-} were constrained.

On top of this SnO_2 slab an amorphous cell of 50 ions (sodium, potassium, rubidium, cesium, ammonia or tetramethyl ammonium) was placed, prepared with the Amorphous Cell module within the Materials Studio program package. Subsequently, the geometry of this composite was optimized with the Forcite force field-package using the following parameters:

Ultrafine convergence criteria (energy change $\Delta E \leq 2.0 \times 10^{-5}\,kcal \cdot mol^{-1}$, force change $\Delta F \leq 0.001\,kcal \cdot mol^{-1}\ A^{-1}$, and displacement $\Delta r \leq 1.0 \times 10^{-5}\ A^{-1}$ per step and COMPASS force field [52], Ewald summation).

After the geometry optimization all ions that were not bonded directly to the surface were removed. The subsequent molecular dynamics simulation was carried out with the Forcite Quench module (NVT-ensemble, 298 K, 100.000 steps á 1 fs, ultra fine quality, COMPASS force field, Ewald-summation). Every 2000 steps the current conformation was saved and following this dynamic simulation the geometry of the resulting 51 frames was optimized. From this trajectory the approximated adsorption energy (E_{ad}) of the ions to the surfaces could be calculated according to

$$\overline{E_{ad}} = \frac{1}{n}\sum_{i=1}^{n} E_{total,i} - (E_{SnO_2,i} + E_{ions,i}) \tag{2.1}$$

In this expression $\overline{E_{ad}}$ are the averaged adsorption energy, n the total number of frames (normally 51), i number of the actual frame, $E_{total,i}$ the energy of the SnO_2 ion composite, $E_{SnO_2,i}$ the energy of the SnO_2 part without adsorbed ions, and $E_{ions,i}$ the energy of the pure ions without SnO_2, each time in the i-th frame. The energy was normalized to the number of adsorbed ions. Water was considered neither explicit nor implicit due to the fact, that the presence of water in earlier studies on systems of polymers and calcium carbonate only affected the absolute values of the adsorption energies but not the trend of these energies in the systems investigated in this study.

Since the absolute values of energies obtained with forcefield-methods are not of interest and the duration taken of a simulation can be decreased considerably, the simulations were done without water.

2.4 Results and Discussion

Before and after the reaction, the pH value of the obtained mixed solutions was measured. Due to the large excess of the base, no net change in the pH was observed, with the exception of TMAH. In addition, all precursor bases except NH_4OH led to a pH value of 14, before the solvothermal treatment, see Table 2.1. The decrease in pH in the reaction with TMAH is due to decomposition of TMAH, which was proven by a blind test where only TMAH with water and ethanol were kept at 200°C for 24 hrs. The pH-decrease in the blind test remained the same. It becomes evident that the pH value of the starting mixture itself has no influence of the morphology of the products, as discussed later.

Table 2.1: pH - values of the reaction mixtures before and after the solvothermal treatment.

Base	**pH before**	**pH after**
NaOH	14	14
KOH	14	14
RbOH	14	14
CsOH	14	14
TMAH	14	11
NH_4OH	11-12	11-12

To clarify the phase composition of the obtained products, X-ray powder diffraction data of all samples were collected. As shown in Figure 2.1 all bases except lithium hydroxide yield single phase, rutile type SnO_2. Products obtained with LiOH - due to the lower solubility of these compounds - contained LiCl and Li_2SnO_3 and LiOH.

Since these reactions did yield neither the desired anisotropic morphology nor the expected product, no computational studies were carried out on this system.

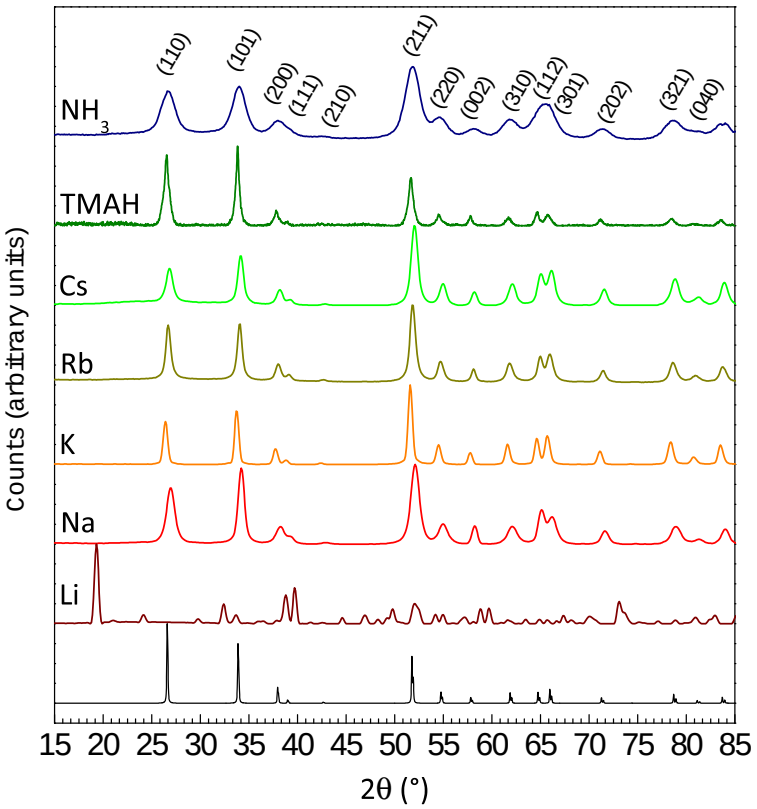

Figure 2.1: Powder X-ray diffraction patterns of SnO_2 nanoparticles obtained at 200°C in the presence of different (LiOH, NaOH, KOH, RbOH, CsOH, TMAH, NH_4OH) precursor bases. The bottom trace corresponds to the diffraction pattern of bulk SnO_2 (Cassiterite).

The Bragg positions and lattice parameters (data from LeBail fits) match well with the filed values (PDF-2, entry (41-1445)) for Cassiterite (a = 4.7456 Å, b = 3.1930 Å, space group No. 136 - $P4_2/mnm$). The broad reflection profiles are due to the very small crystallite size of the nanostructured materials.

The X-ray diffraction patterns of samples prepared with NH_4OH show broad reflection profiles without any intensity alterations due to preferred orientation, see Figure 2.2 (a). In contrast, the diffraction patterns of samples prepared with NaOH exhibit comparably narrow profiles for the (011), (002) and (112) reflections while the profiles of the remaining, 'low l-index', reflections are broad, see Figures 2.1, 2.2 (b) and 2.3. Rietveld refinements modeling this by two different rutile type SnO_2 phases with different crystallite sizes fit only to the experimental diffraction pattern, if preferred orientation is handled by means of spherical harmonics [53] in addition. Both, anisotropic peak broadening as well as intensity alterations due to preferred orientation are in good agreement with the anisotropic morphology of the nanocrystalline product.

Transmission electron microscopy (TEM) images show the particle morphologies obtained with different precursor bases. Figure 2.6 shows that only the Na^+ cation is capable of efficiently inducing a particle growth along the tetragonal axis [001] to yield anisotropic structures with a large aspect ratio (up to 30), see also Figures 2.4 and 2.5.

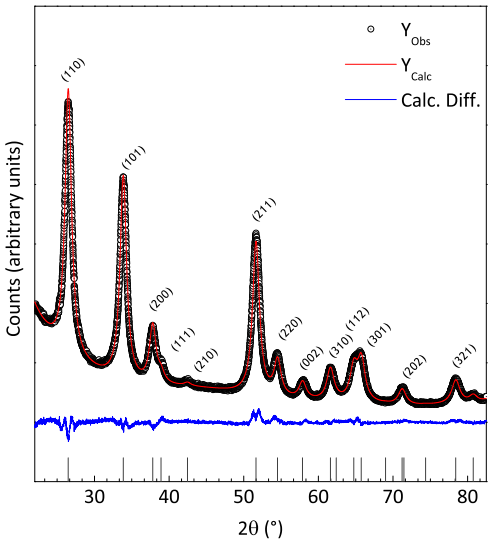

(a)

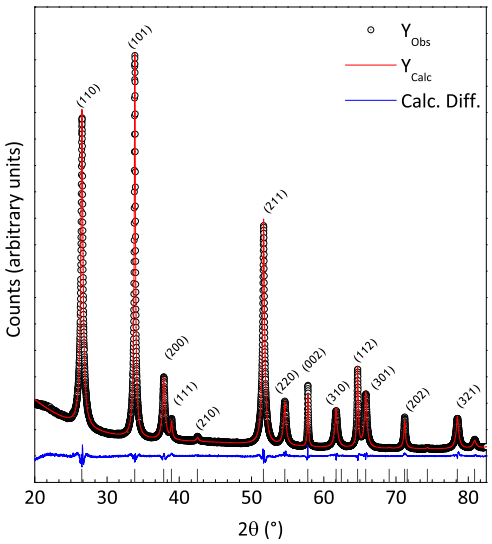

(b)

Figure 2.2: Rietveld refinements of the X-ray powder diffraction pattern of a sample prepared with (a) M = NH_4^+ and (b) M = Na^+ (black: experiment, red: fit, blue: difference curve)

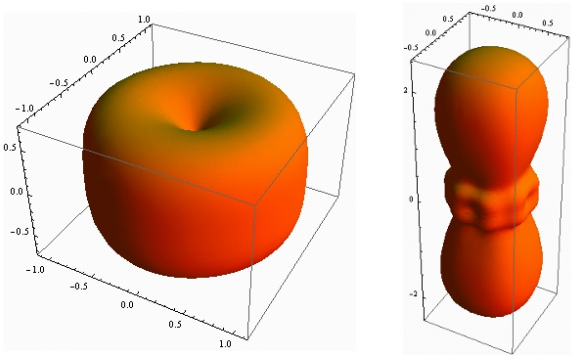

Figure 2.3: Graphical display of the orientation distribution function as derived from the Rietveld refinements. Left: NH_4OH, right: NaOH.

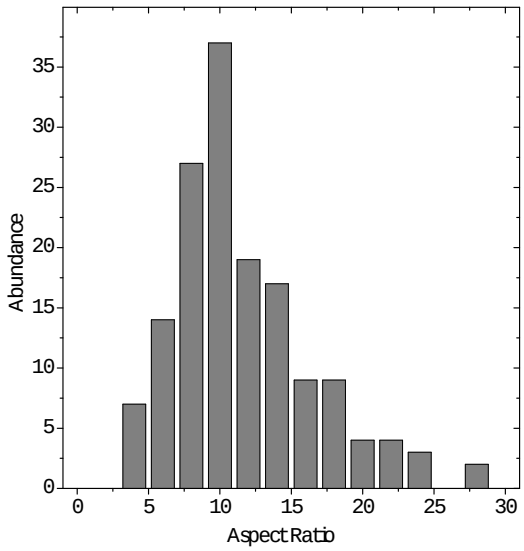

Figure 2.4: Frequency plot of the aspect ratios of SnO_2 nanorods. The sample was prepared with NaOH at 200°C.

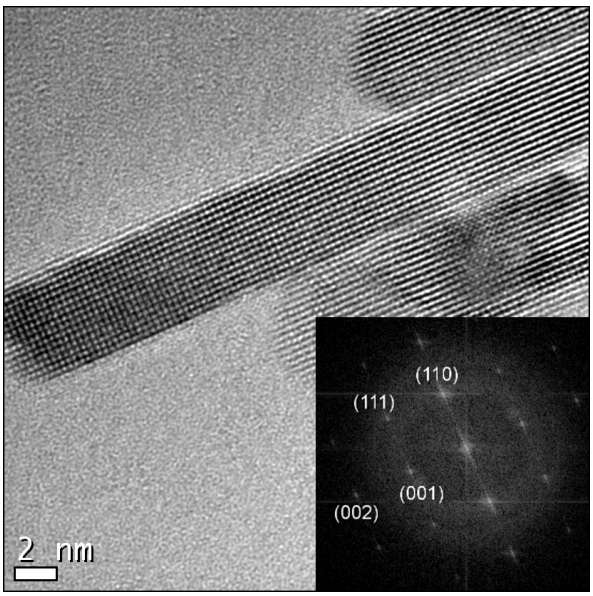

Figure 2.5: High resolution electron micrograph of a SnO_2 nanorod. The inset shows the FFT. The sample was prepared with NaOH at 200°C.

The width of the Bragg reflections (calculated crystallite size 15.9 ± 0.1 nm) in the XRD pattern of the sample prepared with KOH match well with the data derived from the TEM images which contain mostly particles or platelets with an average size of 14.2 ± 3.8 nm (75 particles). Only a very small fraction of the material may be considered as nanorods or one-dimensional. The next larger base cation, Rb^+, yields a mixture of various rod-like structures with a very low aspect ratio. In addition, the sample contained minor amounts of cubes and spheres. Samples prepared with CsOH as the precursor base consist of a mixture of spheres, cubes and rods with a very small aspect ratio.

The samples prepared with tetramethylammonium hydroxide (TMAH) exhibit a strong reflection profile broadening, according to a crystallite size of 13.1 ± 0.1 nm, which is in good agreement with the particle size determined from TEM micrographs (average size 13.4 ± 3.7 nm, derived from 50 particles). Here, a mixture of smaller particles (sphere-like mostly) and some anisotropic rod-like objects are obtained, but

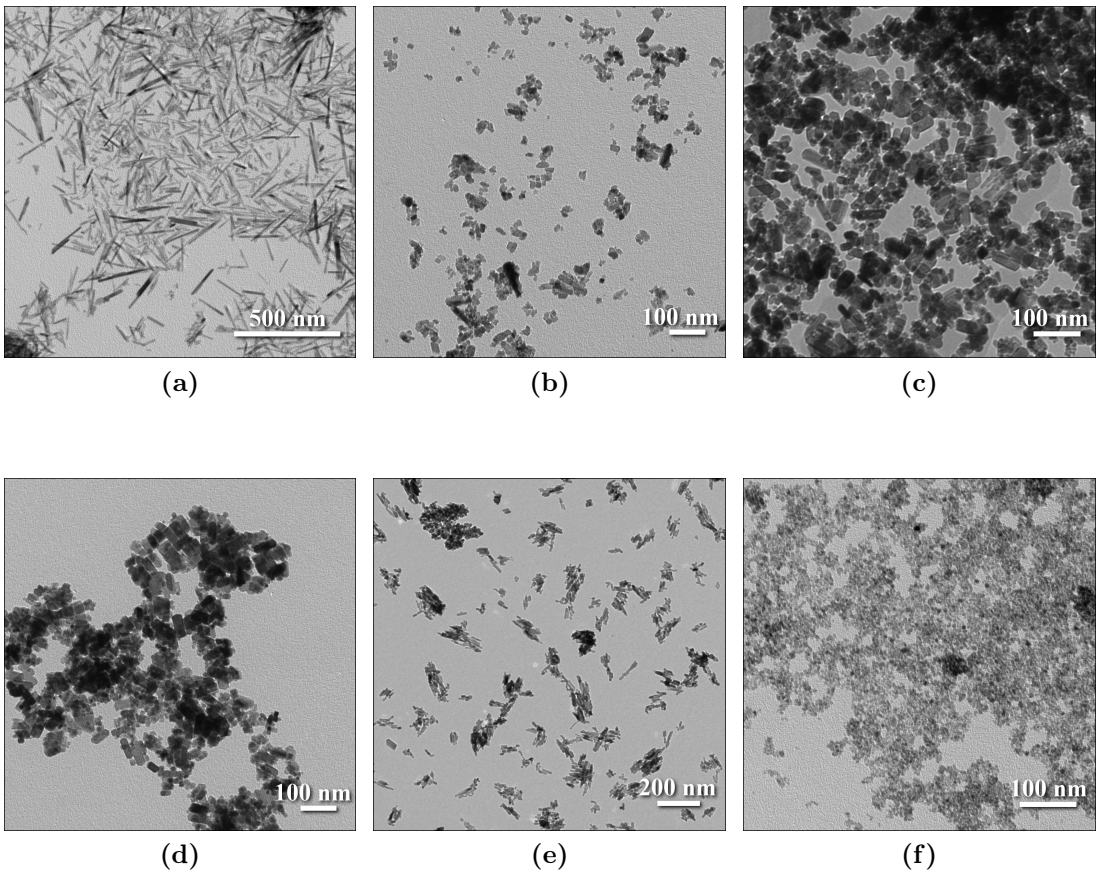

Figure 2.6: TEM images of the products obtained with different precursor bases: (a) NaOH, (b) KOH, (c) RbOH, (d) CsOH, (e) TMAH, and (f) NH_4OH. The samples were prepared at 200°C.

these particles are not well defined and exhibit a small aspect ratio. The width of the reflections of the NH_4OH batch is very broad due to the small crystallite size. The particle diameters derived from the X-ray diffraction data (5.8 ± 0.1 nm) compare well with the observed particle size distribution from the TEM samples, which is 5.2 ± 1.1 nm (average from 75 particles). High resolution micrographs indicate that the particles are single crystalline, and most of them are terminated by the 110 surface. However, some particles seem to show a different orientation (see Figure 2.7). Figure 2.6 (a) shows the obtained nanorod materials, prepared with NaOH as the precursor base.

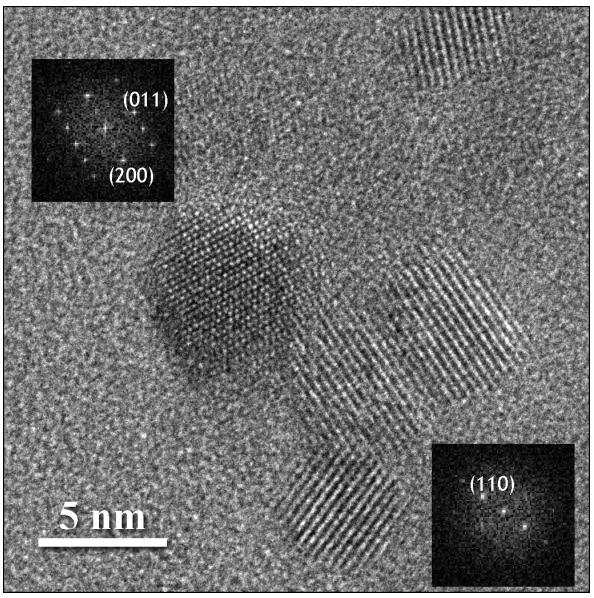

Figure 2.7: HR-TEM micrograph and corresponding Fourier transformation of SnO_2 nanoparticles prepared at 200°C with NH_4OH as precursor base.

The direction of growth is [001], all the observed rods lie on a 110 face, see also Figure 2.5. Since no other orientation was observed and SnO_2 belongs to the tetragonal system, it is likely that the nanorods are laterally delimited by the $\{1\bar{1}0\}$ zone. Actually this means that the crystallographic planes (110), $(\bar{1}\bar{1}0)$, $(\bar{1}10)$ and $(1\bar{1}0)$ are the terminating faces of the obtained nanorods.

These findings agree with comparisons of earlier theoretical studies with experimental data [54, 55]. The surface energies of SnO_2 follow the trend (110) < (100) < (101) < (001) indicating the c axis to be the preferential growth direction. However, our results show that the base precursor has a great influence on the one-dimensional growth. To further elucidate this influence, molecular dynamics simulations were carried out to determine the adsorption energy of the respective cations on the crystal faces that are important for the growth of one-dimensional SnO_2 nanostructures, i.e. the [001] direction as the growth axis and the (110) as the enclosing faces.

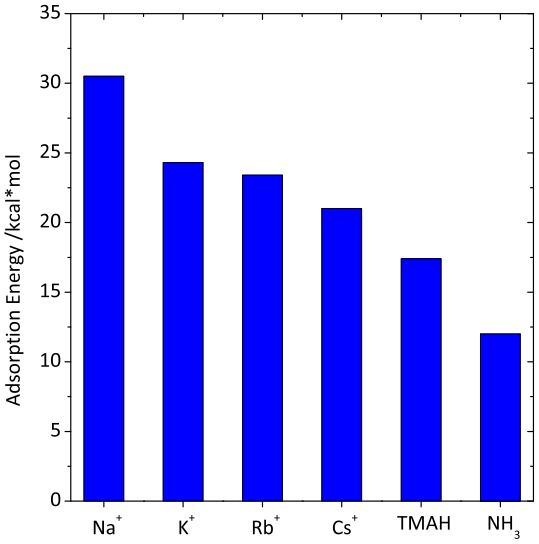

Figure 2.8: Calculated adsorption energies of univalent cations to the (110) face of rutile-type SnO_2.

It is a well known fact that the enclosing faces of a crystal are usually those with the lowest growth rate (i.e. the lowest surface energy) [56]. The surface energy is strongly affected by foreign ions adsorbed to the crystal faces. The adsorption energies of the alkali metal cations decrease with increasing atomic number, NH_3 and TMAH exhibit even smaller adsorption energies (Figure 2.8), Figure 2.9 shows a comparison of the number of adsorbed Na^+ cations onto the 110 and 100 surface of SnO_2. It is evident that also this number is much larger on the 110 surface.

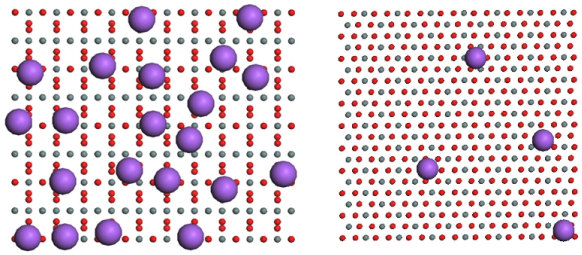

Figure 2.9: Top view onto a SnO_2 surface with adsorbed Na^+-cations (purple): Left (110) and right (100) surface. For clarity the adsorbed ions are shown in van der Waals-representation, the underlying SnO_2 only in a small ball representation (red: O, gray: Sn)

In general, the growth of Cassiterite-type SnO_2 is anisotropic, leading to a needle/column like morphology. The latter is only observed if crystallization conditions are proper, i.e. high temperature and long crystallization time. Upon the conditions leading to nanoparticles, one does typically not find these optimum growth conditions and, thus, very often spherical or at least non-anisotropic morphologies for compounds crystallizing in anisotropic structures are observed. In here, the high adsorption probability of Na^+ cations on the 110 face (also compared to the other crystal surfaces) facilitates the crystallization process already on *non-optimum* conditions, while the lower absorption probabilities of all the other tested cations are not sufficient.

SnO_2 synthesized in aqueous ammonia solution exhibits a nearly spherical morphology because the ratio for blocking the 110 and 001 face is ~ 1, i.e. there is no preferential growth direction. As it has been reported that an increase of the temperature leads to the formation of nanorods with different aspect ratios [57], all studies were repeated at higher temperatures. The results for samples obtained at 250°C are summarized below. The phase purity of the samples was checked and confirmed by means of X-ray powder diffraction. As a result of the higher reaction temperature, all samples display sharper reflection profiles which points to larger crystallite size, see Figure 2.10.

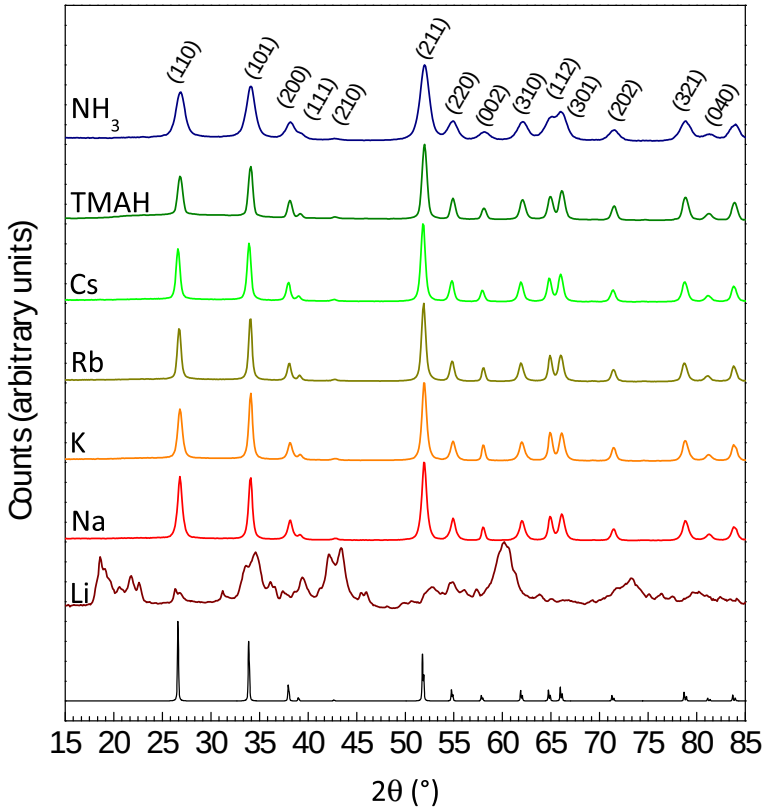

Figure 2.10: Powder X-ray diffraction patterns of SnO_2 nanoparticles obtained after 24 h at 250°C in the presence of different (LiOH, NaOH, KOH, RbOH, CsOH, TMAH, NH_4OH) precursor bases. The bottom trace corresponds to the diffraction pattern of bulk SnO_2 (Cassiterite).

TEM investigations (Figure 2.11) of the samples revealed that with Na^+ as the precursor cation, the rod-like morphology is maintained. The aspect ratio of the particles increases because their diameter remains almost constant whereas their length increases. Some much larger rods are obtained as well. However, in contrast to a previous report [57], all measured rods are terminated by the 110 face which is clearly observable in the Fourier transformation of the high resolution TEM images in Figure 2.12.

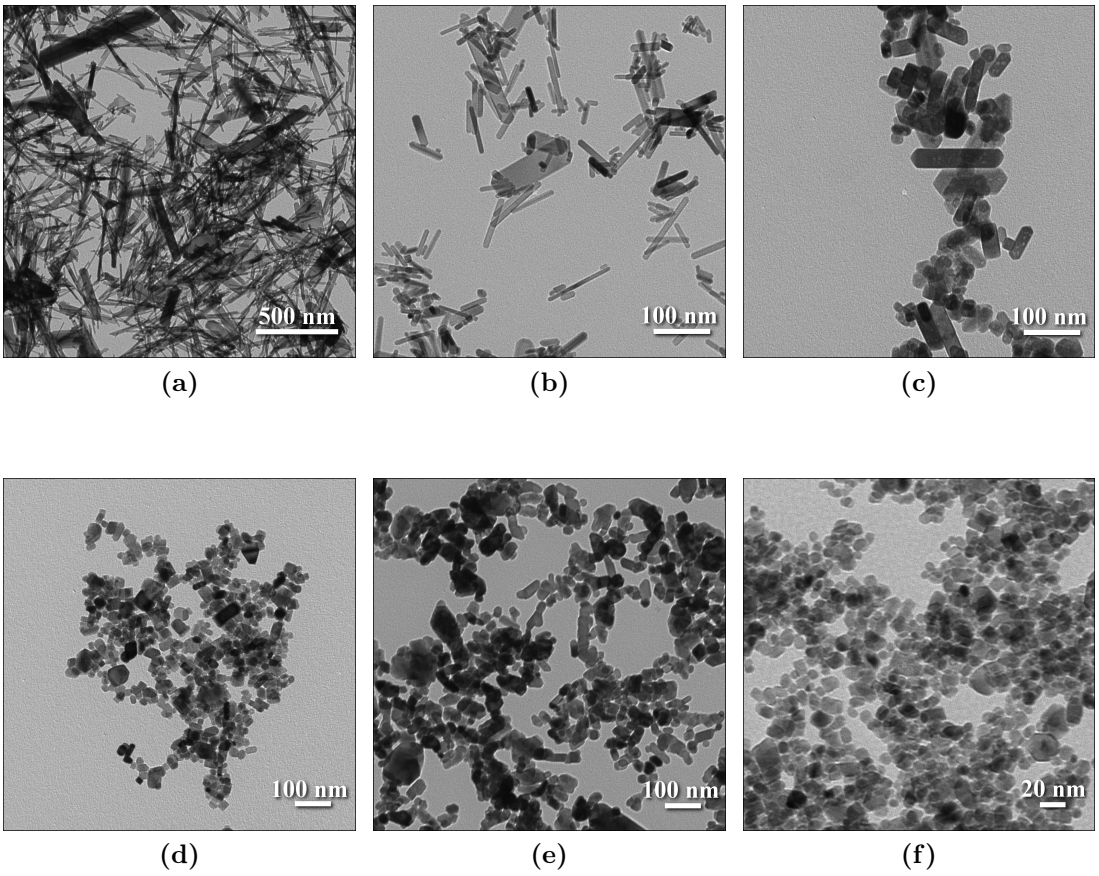

Figure 2.11: TEM images of the products obtained with different precursor bases: (a) NaOH, (b) KOH, (c) RbOH, (d) CsOH, (e) TMAH, and (f) NH_4OH. The samples were prepared at 250°C.

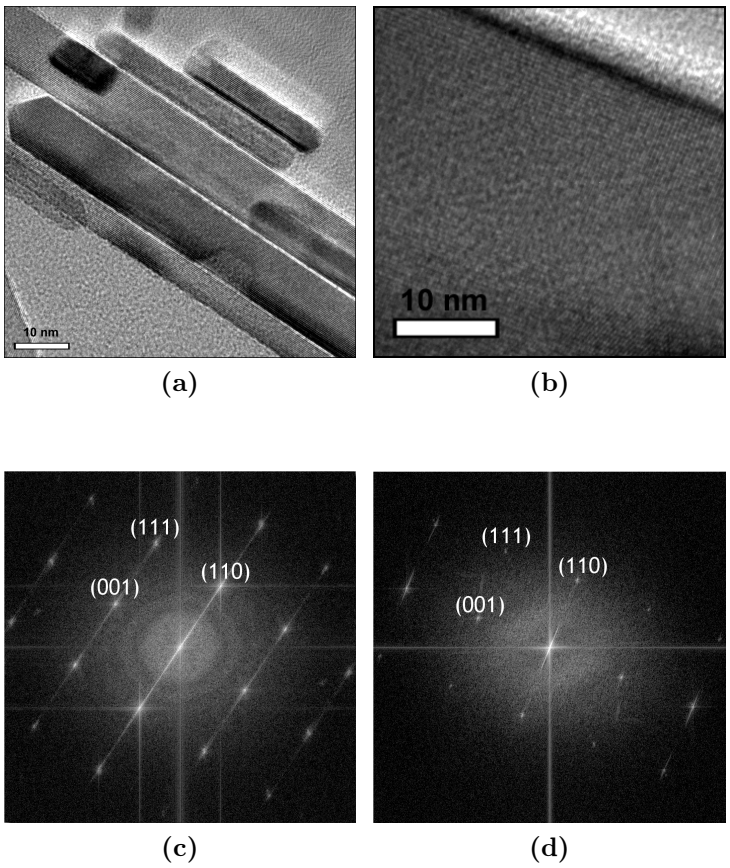

Figure 2.12: HR-TEM micrographs and Fast Fourier Transform (FFT) of SnO_2 nanorods, prepared with NaOH at 250°C. The rods lie on the (110) plane.

The samples synthesized at 250°C exhibit anisotropic morphologies not only in the presence of Na^+, but also with K^+ and Rb^+. This can be related to the more suitable crystallization conditions. Nevertheless the observed aspect ratios are smaller for K^+, Rb^+ and Cs^+ compared to Na^+, which -again- is in line with the trend of the adsorption energies. In order to make sure that the nanorods prepared with potassium, rubidium and, to some extent, cesium are also terminated by the 110 surface, HR-TEM measurements were carried out on these samples as well. As shown in Figure 2.13 (for K^+), these nanorods in different sizes are also enclosed by 110 faces and grow along [001]. Syntheses carried out in aqueous ammonia solution mostly yield isotropic particles.

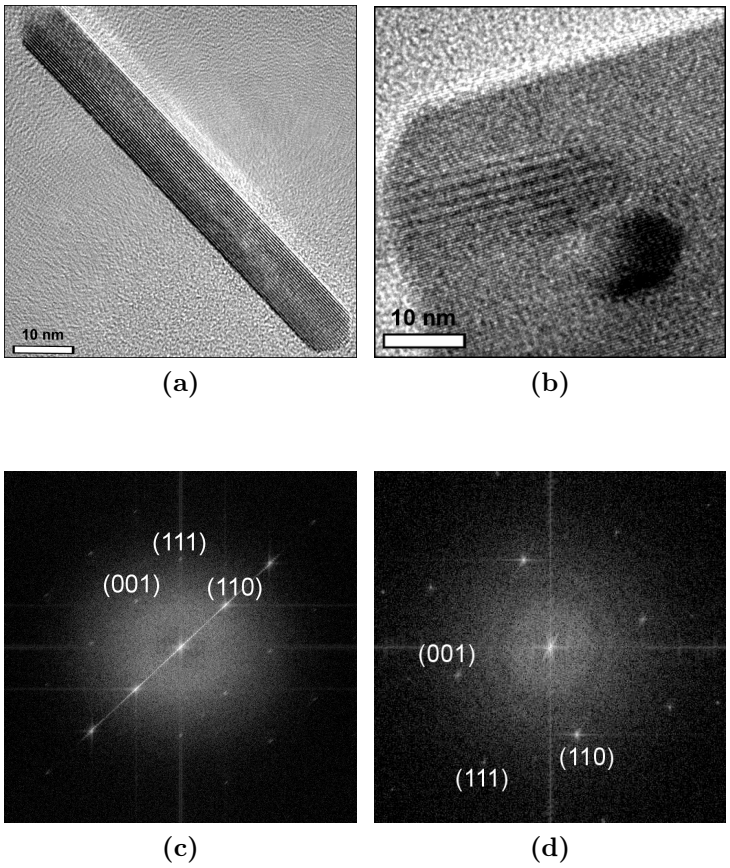

(a) **(b)**

(c) **(d)**

Figure 2.13: HR-TEM micrographs of nanorods prepared by hydrolysis of $SnCl_4$ with KOH at 250°C.

2.5 Conclusion

It was demonstrated that the morphology of anisotropic SnO_2 nanoparticles obtained by polycondensation of hydrated tin tetrachloride at a given pH (large excess of base) strongly depends on the cation of the precursor base, not only on other reaction parameters such as precursor concentration, temperature and time. It could be shown that the trend of decreasing aspect ratios, especially at a reaction temperature of 200°C, can be related to decreasing adsorption-energy E_{Ad} and -probabilities of the base cations on the 110 surface of SnO_2. At a reaction temperature of 250°C, more suitable crystallization conditions lead to the formation of anisotropic morphologies with the precursor cations potassium and rubidium as well, however with a much smaller aspect ratio than with sodium. This finding supports the effect of the counter cation on the morphology of the nanoparticles. The main interaction energy between the SnO_2 surfaces and the adsorbed cations is the coulomb interaction. This interaction is mainly determined by the charge-to-radius-ratio of the adsorbed ions and therefore explicable in terms of the Pearson [58–62] concept of hard and soft acids and bases (HSAB).

References

[1] B. Falabretti and J. Robertson. Electronic structures and doping of SnO_2, $CuAlO_2$, and $CuInO_2$. *Journal of Applied Physics*, 102(12):123703–1, 2007.

[2] P. G. Harrison and M. J. Willett. The Mechanism of Operation of Tin(IV) Oxide Carbon-Monoxide Sensors. *Nature*, 332(6162):337–339, 1988.

[3] W. Göpel. In W. Göpel, J. Hesse, and J.N. Zemel, editors, *Sensors: A Comprehensive Survey*. VCH, Weinheim, Germany, 1995.

[4] M. Law, H. Kind, B. Messer, F. Kim, and P. D. Yang. Photochemical sensing of NO_2 with SnO_2 nanoribbon nanosensors at room temperature. *Angewandte Chemie-International Edition*, 41(13):2405–2408, 2002.

[5] G. X. Wang, J. S. Park, M. S. Park, and X. L. Gou. Synthesis and high gas sensitivity of tin oxide nanotubes. *Sensors and Actuators B-Chemical*, 131(1, Sp. Iss. SI):313–317, 2008.

[6] H. Z. Wang, J. B. Liang, H. Fan, B. J. Xi, M. F. Zhang, S. L. Xiong, Y. C. Zhu, and Y. T. Qian. Synthesis and gas sensitivities of SnO_2 nanorods and hollow microspheres. *Journal of Solid State Chemistry*, 181(1):122–129, 2008.

[7] B. Wang, L. F. Zhu, Y.H. Yang, N. S. Xu, and G. W. Yang. Fabrication of a SnO_2 Nanowire Gas Sensor and Sensor Performance for Hydrogen. *Journal of Physical Chemistry C*, 112:6643–6647, 2008.

[8] P. A. Cox. *The electronic structure and chemistry of solids*. Oxford science publications. Oxford Univ. Press, Oxford, 1987.

[9] R. E. Aitchison. Transparent semiconducting oxide films. *Australian Journal of Applied Science*, 5:10–17, 1954.

[10] Y. S. He, J. C. Campbell, R. C. Murphy, M. F. Arendt, and J. S. Swinnea. Electrical and Optical Characterization of $SbSnO_2$. *Journal of Materials Research*, 8(12):3131–3134, 1993.

[11] X. F. Duan, C. M. Niu, V. Sahi, J. Chen, J. W. Parce, S. Empedocles, and J. L. Goldman. High-performance thin-film transistors using semiconductor nanowires and nanoribbons. *Nature*, 425(6955):274–278, 2003.

[12] L. Vayssieres and M. Grätzel. Highly ordered SnO_2 nanorod arrays from controlled aqueous growth. *Angewandte Chemie-International Edition*, 43(28):3666–3670, 2004.

[13] Y. Fukai, Y. Kondo, S. Mori, and E. Suzuki. Highly efficient dye-sensitized SnO_2 solar cells having sufficient electron diffusion length. *Electrochemistry Communications*, 9(7):1439–1443, 2007.

[14] G. R. A. Kumara, K. Tennakone, I. R. M. Kottegoda, P. K. M. Bandaranayake, A. Konno, M. Okuya, S. Kaneko, and K. Murakami. Efficient dye-sensitize photoelectrochemical cells made from nanocrystalline Tin(IV) oxide-zinc oxide composite films. *Semiconductor Science and Technology*, 18(4):312–318, 2003.

[15] Z. H. Zhong, D. L. Wang, Y. Cui, M. W. Bockrath, and C. M. Lieber. Nanowire crossbar arrays as address decoders for integrated nanosystems. *Science*, 302(5649):1377–1379, 2003.

[16] X. F. Duan, Y. Huang, R. Agarwal, and C. M. Lieber. Single-nanowire electrically driven lasers. *Nature*, 421(6920):241–245, 2003.

[17] Z. W. Pan, Z. R. Dai, and Z. L. Wang. Nanobelts of semiconducting oxides. *Science*, 291(5510):1947–1949, 2001.

[18] D. F. Zhang, L. D. Sun, J. L. Yin, and C. H. Yan. Low-temperature fabrication of highly crystalline SnO_2 nanorods. *Advanced Materials*, 15(12):1022–1025, 2003.

[19] D. L. Chen and L. Gao. Facile synthesis of single-crystal tin oxide nanorods with tunable dimensions via hydrothermal process. *Chemical Physics Letters*, 398(1-3):201–206, 2004.

[20] Y. J. Chen, X. Y. Xue, Y. G. Wang, and T. H. Wang. Synthesis and ethanol sensing characteristics of single crystalline SnO_2 nanorods. *Applied Physics Letters*, 87(23):3, 2005.

[21] S. Das, S. Kar, and S. Chaudhuri. Optical properties of SnO_2 nanoparticles and nanorods synthesized by solvothermal process. *Journal of Applied Physics*, 99(11):7, 2006.

[22] Z. R. Dai, J. L. Gole, J. D. Stout, and Z. L. Wang. Tin oxide nanowires, nanoribbons, and nanotubes. *Journal of Physical Chemistry B*, 106(6):1274–1279, 2002.

[23] E. R. Leite, I. T. Weber, E. Longo, and J. A. Varela. A New Method to Control Particle Size and Particle Size Distribution of SnO_2 Nanoparticles for Gas Sensor Applications. *Advanced Materials*, 12(13):965–968, 2000.

[24] G. Pang, S. Chen, Y. Koltypin, A. Zaban, S. Feng, and A. Gedanken. Controlling the Particle Size of Calcined SnO_2 Nanocrystals. *Nano Letters*, 1(12):723–726, 2001.

[25] J. Q. Hu, Y. Bando, Q. L. Liu, and D. Golberg. Laser-Ablation Growth and Optical Properties of Wide and Long Single-Crystal SnO_2 Ribbons. *Advanced Functional Materials*, 13(6):493–496, 2003.

[26] L. B. Fraigi, D. G. Lamas, and N. E. Walsöe Reca. Comparison between two combustion routes for the synthesis of nanocrystalline SnO_2 powders. *Materials Letters*, 47(4-5):262–266, 2001.

[27] A. Cirera, A. Vilà, A. Cornet, and J. R. Morante. Properties of nanocrystalline SnO_2 obtained by means of a microwave process. *Materials Science and Engineering: C*, 15(1-2):203–205, 2001.

[28] J. J. Zhu, J. M. Zhu, X. H. Liao, J. L. Fang, M. G. Zhou, and H. Y. Chen. Fabrication of a SnO_2 Nanowire Gas Sensor and Sensor Performance for Hydrogen. *Materials Letters*, 53:12–19, 2002.

[29] G. Xi, Y. He, Q. Zhang, H. Xiao, X. Wang, and C Wang. Synthesis of Crystalline Microporous SnO_2 via a Surfactant-Assisted Microwave Heating Method: A General and Rapid Method for the Synthesis of Metal Oxide Nanostructures. *Journal of Physical Chemistry C*, 112(31):11645–11649, 2008.

[30] V. Juttukonda, R. L. Paddock, J. E. Raymond, D. Denomme, A. E. Richardson, L. E. Slusher, and B. D. Fahlman. Facile Synthesis of Tin Oxide Nanoparticles Stabilized by Dendritic Polymers. *Journal of the American Chemical Society*, 128(2):420–421, 2006.

[31] Y. Wang, H. C. Zeng, and J.Y. Lee. Highly Reversible Lithium Storage in Porous SnO_2 Nanotubes with Coaxially Grown Carbon Nanotube Overlayers. *Advanced Materials*, 18(5):645–649, 2006.

[32] M. S. Park, G. X. Wang, Y. M. Kang, D. Wexler, S. X. Dou, and H. K. Liu. Preparation and Electrochemical Properties of SnO_2 Nanowires for Application in Lithium-Ion Batteries. *Angewandte Chemie-International Edition*, 46(5):750–753, 2007.

[33] Q. Dong, H. Su, D. Zhang, W. Cao, and N. Wang. Biogenic Synthesis of Tubular SnO_2 with Hierarchical Intertextures by an Aqueous Technique Involving Glycoprotein. *Langmuir*, 23:8108–9113, 2007.

[34] X. W. Lou, Y. Wang, C. L. Yuan, J. Y. Lee, and L. A. Archer. Template-free synthesis of SnO_2 hollow nanostructures with high lithium storage capacity. *Advanced Materials*, 18(17):2325–2329, 2006.

[35] V. Subramanian, W. W. Burke, H. Zhu, and B. Wei. Novel Microwave Synthesis of Nanocrystalline SnO_2 and Its Electrochemical Properties. *Journal of Physical Chemistry C*, 112(12):4550–4556, 2008.

[36] J. Ba, J. Polleux, M. Antonietti, and M. Niederberger. Non-aqueous Synthesis of Tin Oxide Nanocrystals and Their Assembly into Ordered Porous Mesostructures. *Advanced Materials*, 17(20):2509–2512, 2005.

[37] B. Cheng, J. M. Russell, W. S. Shi, L. Zhang, and E. T. Samulski. Large-scale, solution-phase growth of single-crystalline SnO_2 nanorods. *Journal of the American Chemical Society*, 126(19):5972–5973, 2004.

[38] G. Lagaly, O. Schulz, and R. Zimehl. *Dispersionen und Emulsionen: Eine*

Einführung in die Kolloidik feinverteilter Stoffe einschließlich der Tonminerale. Steinkopff, Darmstadt, 1997.

[39] K. Naka and Y. Chujo. Control of Crystal Nucleation and Growth of Calcium Carbonate by Synthetic Substrates. *Chemistry of Materials*, 13(10):3245–3259, 2001.

[40] C. P. Fenimore and A. Thrailkill. The Mutual Habit Modification of Sodium Chloride and Dipolar Ions. *Journal of the American Chemical Society*, 71(8):2714–2717, 1949.

[41] J. H. Palm and C. H. MacGillavry. Habit modification in the system rocksalt–urea–water. *Acta Crystallographica*, 16(10):963–968, Oct 1963.

[42] A. Singh and B. Ganguly. DFT study of urea interaction with potassium chloride surfaces. *Molecular Simulation*, 34(10):973–979, 2008.

[43] S. Rajam and S. Mann. Selective Stabilization of the (001) Face of Calcite in the Presence of Lithium. *Journal of the Chemical Society, Chemical Communications*, (24):1789–1791, 1990.

[44] I. V. Nefyodova, V. I. Lyutin, V. L. Borodin, P. P. Chvanski, and N. I. Leonyuk. Hydrothermal growth and morphology of calcite single crystals. *Journal of Crystal Growth*, 211(1-4):458–460, 2000.

[45] L. Pastero, E. Costa, M. Bruno, M. Rubbo, G. Sgualdino, and D. Aquilano. Morphology of Calcite ($CaCO_3$) Crystals Growing from Aqueous Solutions in the Presence of Li^+ Ions. Surface Behavior of the {0001} Form. *Crystal Growth & Design*, 4(3):485–490, 2004.

[46] M. Ocaña, M. P. Morales, and C. J. Serna. The Growth Mechanism of [alpha]-Fe_2O_3 Ellipsoidal Particles in Solution. *Journal of Colloid and Interface Science*, 171(1):85–91, 1995.

[47] M. Ocaña, C. J. Serna, and E. Matijević. Formation of "monodispersed" SnO_2 powders of various morphologies. *Colloid & Polymer Science*, 273(7):681–686, 1995.

[48] EVA 10.0, 2003.

[49] A. LeBail, H. Duroy, and J. L. Fourquet. Ab-initio structure determination of $LiSbWO_6$ by X-ray powder diffraction. *Materials Research Bulletin*, 23(3):447–452, 1988.

[50] A. Coelho. TOPAS Academic, V.1.0, 2004.

[51] Materials Studio 4.4, Accelrys Inc., San Diego, CA, 2008.

[52] H. Sun. COMPASS: An ab Initio Force-Field Optimized for Condensed-Phase Applications Overview with Details on Alkane and Benzene Compounds. *Journal of Physical Chemistry B*, 102(38):7338–7364, 1998.

[53] M. Järvinen. Application of symmetrized harmonics expansion to correction of the preferred orientation effect. *Journal of Applied Crystallography*, 26(4):525–531, 1993.

[54] B. Slater, C. R.A. Catlow, D. H. Gay, Williams, and V. Dusastre. Study of surface segregation of antimony on SnO_2 surfaces by computer simulation techniques. *Journal of Physical Chemistry B*, 103(48):10644–10650, 1999.

[55] J. Oviedo and M. J. Gillan. Energetics and structure of stoichiometric SnO_2 surfaces studied by first-principles calculations. *Surface Science*, 463(2):93–101, 2000.

[56] R. Gross. Zur Theorie des Wachstums- und Lösungsvorganges kristalliner Materie. In *Abh. d. math.-phys. Klasse der sächs. Ges. der Wiss.*, volume 35, pages 137–202. Leipzig, 1918.

[57] L. Qin, J. Xu, X. Dong, Q. Pan, Z. Cheng, Q. Xiang, and F. Li. The template-free synthesis of square-shaped SnO_2 nanowires: the temperature effect and acetone gas sensors. *Nanotechnology*, 19(18), 2008.

[58] R. G. Pearson. Absolute electronegativity and hardness: application to inorganic chemistry. *Inorganic Chemistry*, 27(4):734–740, 1988.

[59] S. Pal and K. R. S. Chandrakumar. Critical Study of Local Reactivity Descriptors for Weak Interactions: Qualitative and Quantitative Analysis of Adsorption of Molecules in the Zeolite Lattice. *Journal of the American Chemical Society*, 122(17):4145–4153, 2000.

[60] R. G. Pearson. Hard and soft acids and bases, HSAB, part 1: Fundamental principles. *Journal of Chemical Education*, 45:581–587, 1968.

[61] A. Alfarra, E. Frackowiak, and Béguin F. The HSAB concept as a means to interpret the adsorption of metal ions onto activated carbons. *Applied Surface Science*, 228(1-4):84–92, 2004.

[62] M. Wisniewski and P. A. Gauden. The HSAB principle as a means to interpret the reactivity of carbon nanotubes. *Applied Surface Science*, 255(9):4782 – 4786, 2009.

3

A simple One-step Reaction Pathway towards SnO_2 - $Na_2Sn(OH)_6$ "core-shell" Nanorods

3.1 Abstract

A simple reaction pathway to obtain core-shell nanorod type SnO_2 materials was investigated. The products could be prepared by a solvothermal technique starting from tin (IV) chloride and sodium hydroxide as the precursors. X-ray powder diffraction data (XRD) and energy dispersive X-ray spectroscopy (EDX) show the presence of SnO_2 and $Na_2Sn(OH)_6$. Transmission electron microscopy (TEM) pictures reveal the rod-shaped morphology with dimensions from 5-25 nm in width and up to 200 nm in length. High-resolution TEM micrographs clearly indicate the presence of a shell containing sodium and a higher amount of oxygen than the core. The influence of the shell on the optical properties of the core-shell nanorods has been examined.

3.2 Introduction

Among the many varieties of nanostructures, core-shell materials have been the subject of great attention over the last years [1]. Through careful preparation techniques, a wide-range of tunable properties is achievable, often improving the single properties of both, the core and the shell material. Applications include, but are not limited to, solar cells [2], here especially dye-sensitized solar cells (DSSC), catalysis, separations, and diagnostics [3, 4]. In this vast field, core-shell nano-"composites" with SnO_2 are of vivid interest.

Tin (IV) oxide is a wide band-gap semiconductor [5] (E_g = 3.6 eV) material that crystallizes in the rutile structure (SG: $P4_2/mnm$). Synthetic routes towards (1D)-nanostructures of SnO_2 include thermal evaporation [6], solution phase-growth [7–9] and template-assisted methods [10]. Those nanomaterials are prominently used e.g. in gas sensing devices [11] and in dye-sensitized solar cells. However, especially in solar cells, due to the high electron mobility [12] (which creates a lot of recombination problems), SnO_2 is often used in conjunction with other semiconductors or insulators, in most cases in the form of core-shell structures. Therefore, one-step reaction pathways towards these materials could offer a significant facilitation of the fabrication of those substances. The observed shell material in this contribution is $Na_2Sn(OH)_6$. Stannates such as Zn_2SnO_4 can also be found as electrode materials in solar cells [13, 14]. Thus, a combination between a SnO_2 core and a stannate shell, obtained in a simple one step reaction could establish a promising alternative for photoanodes in dye-sensitized solar cells.

3.3 Experimental

3.3.1 Sample Preparation

The obtained products were prepared by a facile solvothermal technique, modifying a reported reaction pathway [15]. In a typical synthesis, 3.5 ml 0.5 M $SnCl_4 \cdot 5H_2O$ solution and 3.5 ml 5 M NaOH were mixed together with 25 ml of an ethanol : water mixture with a ratio of 15 : 10. After several minutes of stirring, the reaction mixture was transferred into a 50 ml Teflon vessel and finally sealed in a hydrothermal autoclave. The autoclave was heated to 200°C for 24 hours and allowed to cool down to room temperature naturally. The obtained white-gray powders were separated by centrifugation (9000 rpm) and washed several times with water and ethanol. Finally, the powder was dried at 75°C.

3.3.2 Characterization

Electron Microscopy

The products were characterized using transmission electron microscopy (TEM) using a Philips 420 instrument with an acceleration voltage of 120 kV or a Philips TECNAI F30 electron microscope (field-emission gun, 300 kV extraction voltage) equipped with an Oxford EDX (energy-dispersive X-ray) spectrometer with a Si/Li detector and an ultrathin window for elemental analysis. Samples for TEM measurements were prepared from ethanolic suspensions of the samples. One to two drops of the ultrasonicated suspension were administered on a Cu grid coated with an amorphous carbon layer.

X-ray Powder Diffraction

X-ray diffraction patterns (XRD) were recorded using a Siemens D5000 with CuKα_1 radiation (Ge (220) monochromator) and a Braun M50 position sensitive detector. Phase analyses were performed according to the PDF-2 using Bruker AXS EVA 10.0 [16]. Crystallite sizes, intensity alterations due to preferred orientation and anisotropic reflection profile broadening due to anisotropic morphologies were determined by means of LeBail fits [17] and Rietveld refinements [18], respectively, applying the fundamental parameter approach using TOPAS Academic V4.1 [19].

Infrared Spectroscopy

Infrared spectroscopy was performed using a Mattson Instruments 2030 Galaxy-FT-IR spectrometer.

UV-VIS-Spectroscopy

UV-VIS diffuse reflectance spectroscopy (DRS) was performed on a Cary 5G UV-Visible-NIR spectrophotometer at room temperature in the wavelength range between 200 and 600 nm using $BaSO_4$ (Merck) as the white standard.

3.4 Results and Discussion

If the procedure described in the experimental part is used with a ethanol : water mixture in the ratio 1 : 1 (v/v), only phase pure tin (IV) oxide nanorods can be observed. However, a simple change of the ratio ethanol : water changes the phase composition of the obtained materials from SnO_2 (1 : 1) to $Na_2Sn(OH)_6$ (20 : 5). The intermediate ratio of ethanol : water (15 : 10) does not yield a simple phase mixture, but "core-shell" materials, see Figure 3.1. This is attributed to the different solubilities of the reaction products in the water-ethanol mixtures; The yield of stannate increases with increasing ethanol content, due to the higher solubility of $Na_2Sn(OH)_6$ in water.

To clarify the phase composition of the obtained core-shell materials, X-ray powder diffraction data were recorded and Rietveld refinement was performed to determine the crystallite sizes and the ratio of the two phases. The positions of the reflexes and the lattice parameters match well with the filed values in the literature [20]. For cassiterite, the lattice parameters were found to be $a = 4.7492(4)$ Å and $c = 3.1885(3)$ Å.

For the sodium stannate (SG: $R\bar{3}$), the lattice parameters were determined to be $a = 5.9690(9)$ Å and $c = 14.2380(32)$ Å. Figure 3.2 shows the data including the Rietveld refinement, applying two separate phases, with the first one being SnO_2 and the second one $Na_2Sn(OH)_6$. A quantitative analysis shows that $\approx 85\%$ of the material are SnO_2 with the remaining 15% being attributed to $Na_2Sn(OH)_6$. The computed reflection profiles of the SnO_2 phase do not exactly fit to the observed ones due to the anisotropic particle morphology.

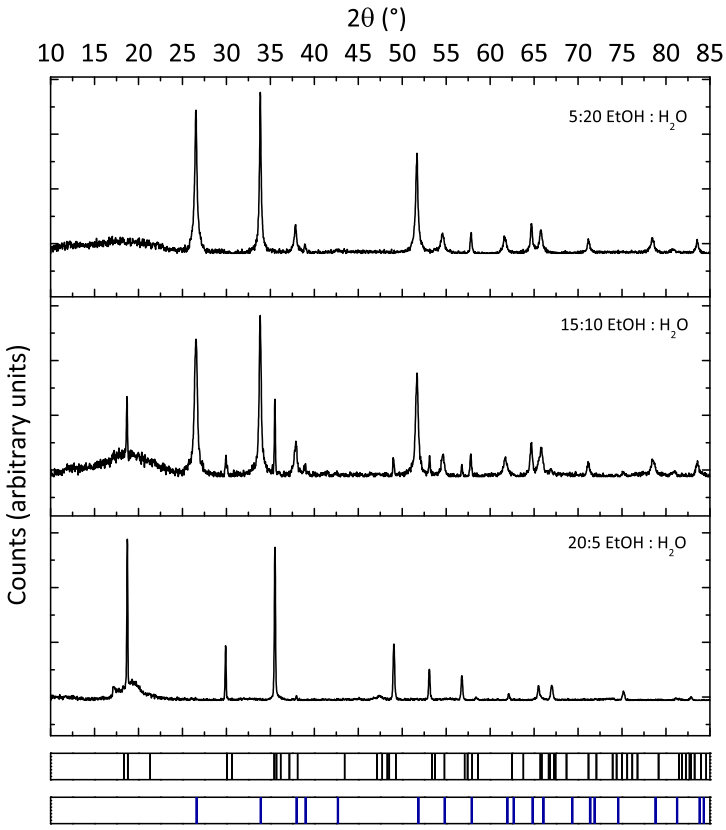

Figure 3.1: X-ray diffraction data of the samples obtained with different water : ethanol ratios. The blue and black bars represent the calculated 2θ-values for the reflexes of $Na_2Sn(OH)_6$ and SnO_2 respectively.

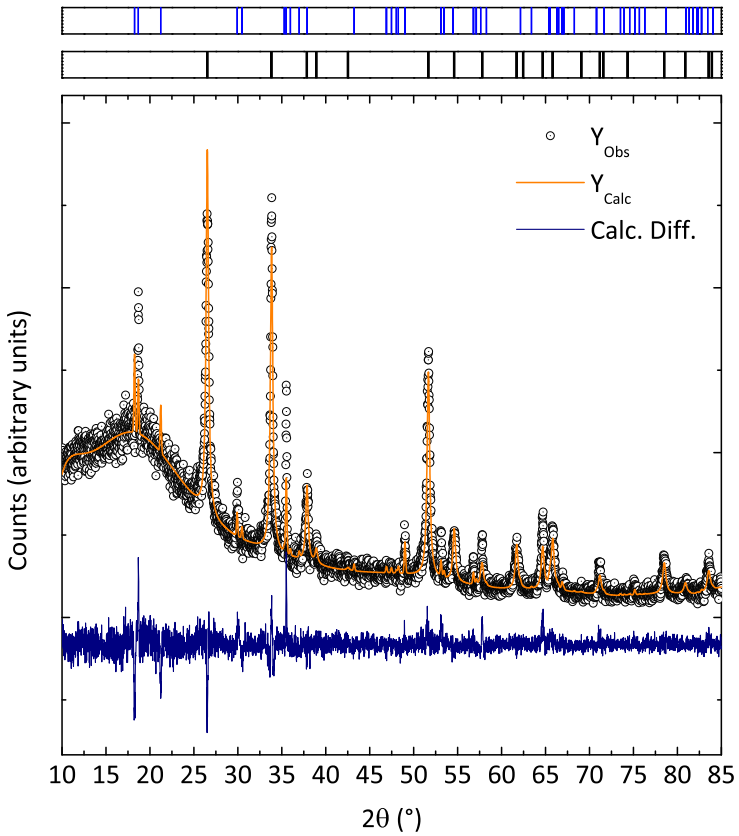

Figure 3.2: Rietveld refinement of the X-Ray diffraction data. The blue and black bars represent the 2θ-values for the reflexes of $Na_2Sn(OH)_6$ and SnO_2 respectively.

Further, due to the fact that the reflexion profiles attributed to the stannate phase are rather narrow, the X-ray data suggests that there are two separate crystalline phases: The SnO_2 nanorods (i.e. the origin of the broad reflexions that show anisotropy) and the stannate phase with a crystallite size that is "too large" for a nanostructured shell material. For such shell materials, especially a nanostructured one, one would expect the profiles to be much broader, due to the very small crystallite size.

Transmission electron micrographs reveal the presence of rod-shaped materials. Figure 3.3 shows a single core-shell nanorod. A shell consisting of a thin diffuse layer and sphere-shaped particles is clearly observable around the anisotropic core. The vast majority of rods found in a typical sample exhibits this structure, i.e. rod-like cores including a shell.

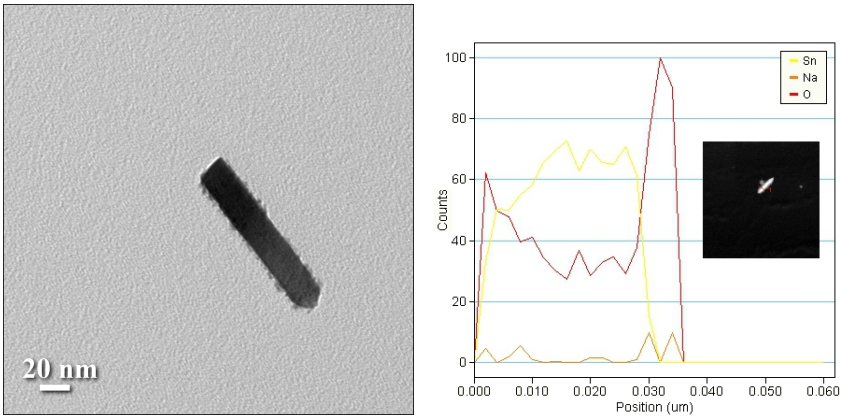

(a) **(b)**

Figure 3.3: TEM images of the obtained nanostructured core-shell material. (a) Low magnification image of a single core-shell nanorod; (b) EDX line-scan across one core-shell nanorod.

The HR-TEM micrograph (Figure 3.4) shows that the core of the materials is crystalline. Lattice fringes are clearly visible. Covering the anisotropic core, one can see a shell that seems to be amorphous since no clear lattice fringes are observable. This is, again, contradictory to the diffraction data. Firstly, because the stannate phase is supposed to exhibit a sufficient crystallinity to yield narrow reflexions (i.e. one should be able to observe lattice fringes, although this might also have a different origin such as the diffraction contrast of the stannate) and secondly, it is clearly observable that the shell is also in the range of nanometers, meaning that the reflexion profiles of this phase should be rather broad, as aforementioned.

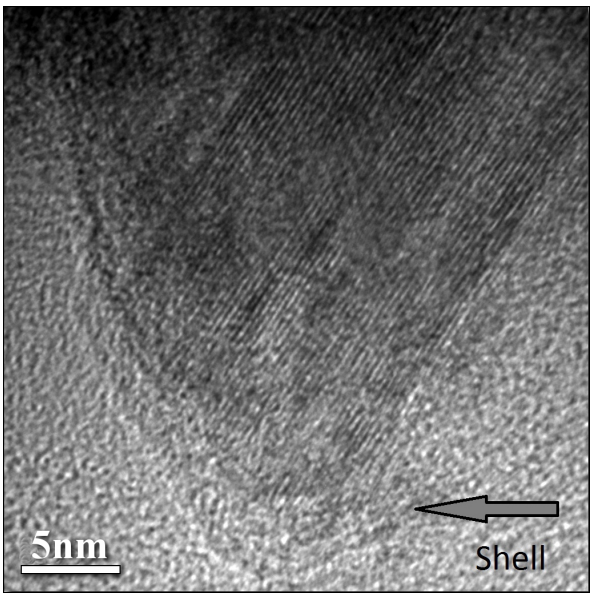

Figure 3.4: HR-TEM picture of a single core-shell nanorod. The arrow points out the shell layer.

To get a better insight into the chemical composition of the core-shell materials, energy dispersive X-ray spectroscopy (EDX) was employed. A line-scan across one core-shell particle (Figure 3.3 (b)) reveals that the elements tin (Sn - yellow line), oxygen (O - deep red line) and sodium (Na - orange line) are present. No other elements could be detected, proving again the purity of the prepared materials. Interestingly, the sodium (although very low in absolute values) and oxygen content are higher at the edges of the rod. The inner part consists almost entirely of tin and oxygen. This is pointing again towards the fact that the shell material is composed of $Na_2Sn(OH)_6$, although not necessarily crystalline.

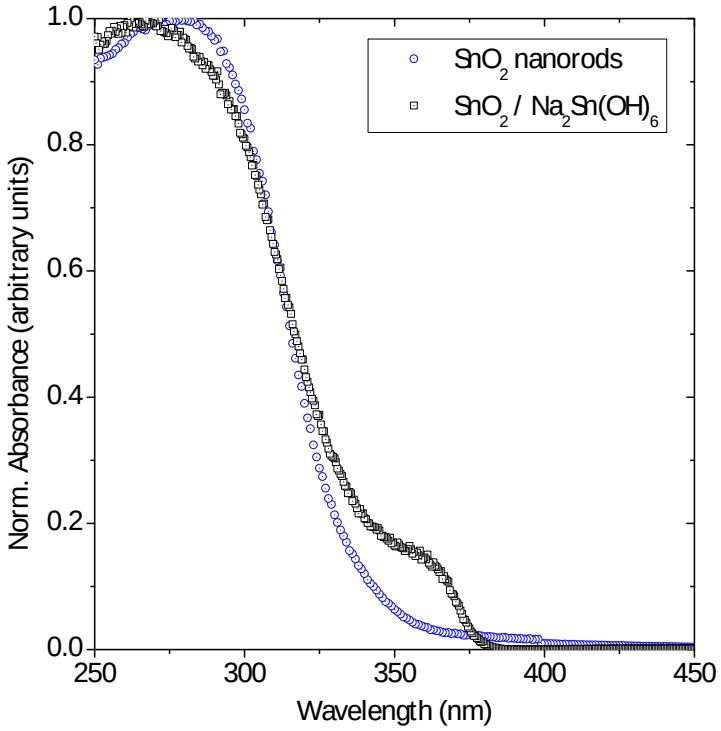

Figure 3.5: UV-Vis absorption spectra of pure SnO_2 nanorods and $SnO_2/Na_2Sn(OH)_6$ core-shell structures.

To investigate the influence of the core-shell structure onto the optical properties, UV-Vis absorption and FT-IR spectra were recorded. The optical absorbance is presented in Figure 3.5.

The onset of the absorption corresponds for the pure SnO_2 nanomaterials to a band-gap of $\sim$338 nm $\rightarrow$ 3.68 eV. For semiconducting nanoparticles, there is an expected shift of the absorption edge to higher energies (compared to bulk values) due to the quantum confinement when the particle size decreases below the electron Bohr radius. For SnO_2, this radius has been calculated to be 2.7 nm. Since in our case only the tip of the rods is smaller than that radius, we only observe a mild shift towards higher

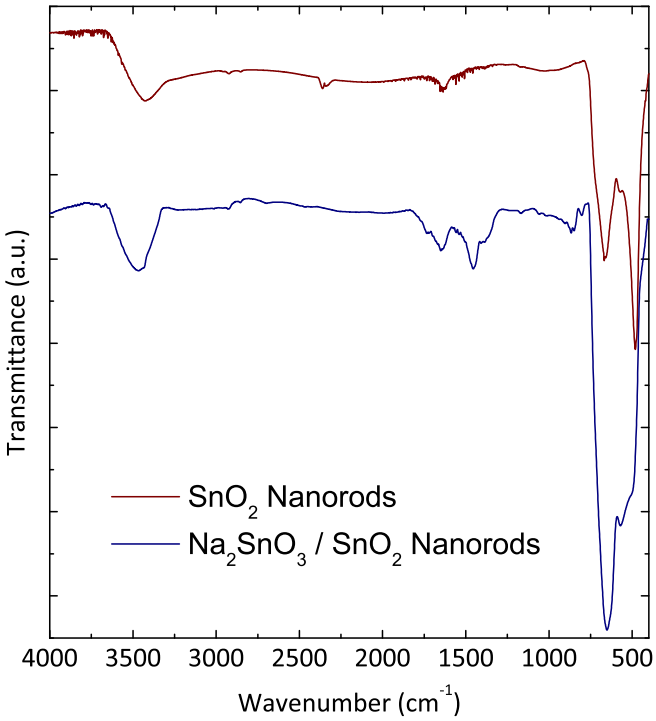

Figure 3.6: FT-IR spectra of pure SnO_2 nanorods and $SnO_2/Na_2Sn(OH)_6$ core-shell structures.

energies. It is obvious that the core-shell material exhibits an additional feature, leading to a second onset at around 380 nm, corresponding to an optical band-gap of 3.25 eV.

The infrared absorption spectra are shown in Figure 3.6. The FT-IR spectrum of "pure" SnO_2 nanorods shows two broad absorption bands around 480 cm^{-1} as well as around 630 until 700 cm^{-1}. These bands arise from stretching vibrations of geminal oxygen atoms (νSnOSn) [21, 22], with the band at 480 cm^{-1} being attributed to the symmetric and the bands at 630 cm^{-1} being attributed to the asymmetric vibration [23]. The metal-oxygen vibration in the bulk appears in the IR spectrum mostly between 200 and 800 cm^{-1}. However, this vibration in the surface lattice differs from

that in the bulk and appears usually at higher wave numbers. The absorption bands around 1615 cm^{-1} and 3400 cm^{-1} might be attributed to the δOH_2 stretching vibration of surface hydroxyl group or surface bound water which has been observed due to the re-adsorption of water molecules from ambient atmosphere. In comparison to that, the core-shell material exhibits the same bands plus one additional one, at around 870 cm^{-1}. This band can be attributed to OH-in-plane-bending vibrations [24] and is a distinct difference between the bare and the core-shell material.

3.5 Conclusion and open Questions

Core-shell nano-materials could successfully be prepared using a very simple one-step reaction pathway, starting from a tin precursor, a base and a water : ethanol mixture. The presence of two phases was verified using X-ray powder diffraction. Transmission electron microscopy was used to reveal the fact that a core-shell structure has formed. Energy dispersive X-ray spectroscopy suggests that the shell consists of a phase richer in oxygen and sodium than the core, which is only composed of tin and oxygen (i.e. SnO_2). However, the results from the TEM/EDX measurements and the XRD data on the other hand are somewhat contradictory (see below). The optical properties have been investigated using UV-Vis and FT-IR spectroscopy. It could be shown that the shell significantly changes the optical behavior.

Unfortunately, due to unknown reasons, the reproducibility of the reaction became insufficient, meaning that the results were not reproducible anymore in a satisfactory way. Therefore, the following important issues that arise from the processing of the data remain:

What is the exact origin of the diffraction reflexions of $Na_2Sn(OH)_6$? This has not been elucidated completely since the shell material that is observed in the HR-TEM pictures clearly contains sodium and a higher oxygen content than the SnO_2 - core, however it seems that the shell is mostly amorphous and possesses a very small crystallite size, and hence cannot be "responsible" for the occurrence of the sharp reflexes in the diffraction patterns.

Are the changes in the optical properties solely due to the core-shell structure of the materials or would a "nano-composite" show the same behavior?

A more detailed study of the infrared and raman behavior would also be necessary to elucidate the differences between a possible core-shell material, a "nano-composite" and the bare SnO_2 nanorods.

To summarize, evidence of a "nano-composite" of SnO_2 and $Na_2Sn(OH)_6$ have been found. HR-TEM and EDX analysis point towards the shell consisting of the stannate. However, the diffraction data are not in line with these findings and therefore a more careful investigation is necessary.

References

[1] F. Caruso. Nanoengineering of Particle Surfaces. *Advanced Materials*, 13(1):11–22, 2001.

[2] A. Kay and M. Grätzel. Dye-sensitized core-shell nanocrystals: Improved efficiency of mesoporous tin oxide electrodes coated with a thin layer of an insulating oxide. *Chemistry of Materials*, 14(7):2930–2935, 2002.

[3] L. M. Liz-Marzán, M. Giersig, and P. Mulvaney. Synthesis of Nanosized Gold-Silica Core-Shell Particles. *Langmuir*, 12(18):4329–4335, 1996.

[4] R. Davies, G. A. Schurr, P. Meenan, R. D. Nelson, H. E. Bergna, C. A. S. Brevett, and R. H. Goldbaum. Engineered Particle Surfaces. *Advanced Materials*, 10(15):1264–1270, 1998.

[5] B. Falabretti and J. Robertson. Electronic structures and doping of SnO_2, $CuAlO_2$, and $CuInO_2$. *Journal of Applied Physics*, 102(12):123703–1, 2007.

[6] Z. W. Pan, Z. R. Dai, and Z. L. Wang. Nanobelts of semiconducting oxides. *Science*, 291(5510):1947–1949, 2001.

[7] B. Cheng, J. M. Russell, W. S. Shi, L. Zhang, and E. T. Samulski. Large-scale, solution-phase growth of single-crystalline SnO_2 nanorods. *Journal of the American Chemical Society*, 126(19):5972–5973, 2004.

[8] L. Vayssieres and M. Grätzel. Highly ordered SnO_2 nanorod arrays from controlled aqueous growth. *Angewandte Chemie-International Edition*, 43(28):3666–3670, 2004.

[9] H. Z. Wang, J. B. Liang, H. Fan, B. J. Xi, M. F. Zhang, S. L. Xiong, Y. C. Zhu, and Y. T. Qian. Synthesis and gas sensitivities of SnO_2 nanorods and hollow microspheres. *Journal of Solid State Chemistry*, 181(1):122–129, 2008.

[10] D. F. Zhang, L. D. Sun, J. L. Yin, and C. H. Yan. Low-temperature fabrication of highly crystalline SnO_2 nanorods. *Advanced Materials*, 15(12):1022–1025, 2003.

[11] Y. L. Wang, X. C. Jiang, and Y. N. Xia. A solution-phase, precursor route to polycrystalline SnO_2 nanowires that can be used for gas sensing under ambient conditions. *Journal of the American Chemical Society*, 125(52):16176–16177, 2003.

[12] A. N. M. Green, E. Palomares, S. A. Haque, J. M. Kroon, and J. R. Durrant. Charge Transport versus Recombination in Dye-Sensitized Solar Cells Employing Nanocrystalline TiO_2 and SnO_2 Films. *Journal of Physical Chemistry B*, 109(25):12525–12533, 2005.

[13] V. Rajan Jose. Metal Oxides for Dye-Sensitized Solar Cells. *Journal of the American Ceramic Society*, 92(2):289–301, 2009.

[14] B. Tan, E. Toman, Y. G. Li, and Y. Y. Wu. Zinc stannate (Zn_2SnO_4) dye-sensitized solar cells. *Journal of the American Chemical Society*, 129(14):4162–4163, 2007.

[15] Y. J. Chen, X. Y. Xue, Y. G. Wang, and T. H. Wang. Synthesis and ethanol sensing characteristics of single crystalline SnO_2 nanorods. *Applied Physics Letters*, 87(23):3, 2005.

[16] EVA 10.0, 2003.

[17] A. LeBail, H. Duroy, and J. L. Fourquet. Ab-initio structure determination of $LiSbWO_6$ by X-ray powder diffraction. *Materials Research Bulletin*, 23(3):447–452, 1988.

[18] H. Rietveld. A profile refinement method for nuclear and magnetic structures. *Journal of Applied Crystallography*, 2(2):65–71, 1969.

[19] A. Coelho. TOPAS Academic, V.1.0, 2004.

[20] H. Jacobs and R. Stahl. Redetermination of the crystal structures of the hexahydroxometallates $Na_2Sn(OH)_6$, $K_2Sn(OH)_6$, and $K_2Pb(OH)_6$. *Zeitschrift für Anorganische und Allgemeine Chemie*, 626(9):1863–1866, 2000.

[21] W. W. Wendlandt and H. G. Hecht. *Reflectance Spectroscopy*. Wiley Interscience, New York, 1966.

[22] F. Gu, S. Fen Wang, C. Feng Song, M. Kai Lü, Y. Xin Qi, G. Jun Zhou, D. Xu, and D. Rong Yuan. Synthesis and luminescence properties of SnO_2 nanoparticles. *Chemical Physics Letters*, 372(3-4):451–454, 2003.

[23] D. N. Srivastava, S. Chappel, O. Palchik, A. Zaban, and A. Gedanken. Sonochemical Synthesis of Mesoporous Tin Oxide. *Langmuir*, 18(10):4160–4164, 2002.

[24] M. Maltese and W. J. Orville-Thomas. The infrared spectra and structure of some complex hydroxosalts. *Journal of Inorganic and Nuclear Chemistry*, 29(10):2533–2544, 1967.

4 Snapshots of the Microwave-Assisted Synthesis of SnO_2 - Nanorods

4.1 Abstract

A microwave-assisted reaction pathway to rutile SnO_2 nanorods was investigated. The microwave-treatment significantly reduces the reaction time compared to standard hydro-/ solvothermal techniques. By moving the overall process into a shorter time slot, the growth and crystal formation during the reaction could be monitored via snapshots by trapping the intermediates through quenching. To gain a better insight into the template-free growth of one-dimensional (1D) nanostructures, a parameter-dependent (various temperatures/pressures and times were investigated) study was carried out. For all materials, the phase purity and crystallite sizes were determined by X-ray powder diffraction (XRD). The growth-orientation and terminating crystal faces of the reaction intermediates were determined using HR-TEM measurements. A growth mechanism was proposed. The optical properties were studied by means of Raman and infrared spectroscopy.

4.2 Introduction

Inorganic nanostructures have attracted enormous research interest over the past years. One part of this huge field is the focus on semiconductor nanoparticles. Among these, SnO_2 has been studied extensively. Being a wide band-gap semiconductor [1] (E_g = 3.6 eV at 300 K), 1-D tin dioxide nanostructures like nanorods [2, 3], nano-wires [4–6] and nano-tubes [7] have found applications as gas sensors [8–11], transparent conducting surface layers and electrodes [12], transistors [6], as well as in photovoltaic applications [13]. Especially the use of SnO_2 as an electrode material in dye-sensitized solar cells is of great interest [14–16]. Synthetic routes to 1D SnO_2 nanoparticles include thermal evaporation [5], template-assisted methods [17] (such as micro emulsions) and solution-phase growth [3, 9, 13].

During the past decade, microwave-solvothermal methods have emerged as a powerful synthetic tool for metal oxide nanoparticles [18, 19]. Our information concerning the kinetics of the formation of ternary or even binary metal oxides under microwave conditions is limited for the following reasons: (*i*) The prediction of solvothermal products is mostly impossible due to a lack of general theoretical models. (*ii*) The structural chemistry of transition metal oxide systems is often complicated, because a variety of potential products can be formed. This renders the mechanistic investigation of solvothermal reactions a key task of modern materials research.

Therefore, the microwave-assisted formation of 1D tin dioxide nanostructures is a model reaction. By evaluating the kinetics of nanostructured SnO_2, the formation process of these materials was studied. By varying reaction parameters such as the reaction time and temperature, a detailed insight into the growth process of SnO_2 nanostructures under solvothermal conditions could be obtained. Compared to standard solvothermal techniques that rely on heating in conventional furnaces, the very

fast heating and cooling times in a microwave reactor provide the unique opportunity to take snapshots of the crystallization and morphological evolution of nanostructures that provide similar kinetic information as studies of the growth mechanism by in situ EXAFS and XRD [20].

4.3 Experimental

4.3.1 Sample Preparation

The obtained products were prepared by a facile microwave-assisted technique, modifying a reaction pathway reported before [2, 21]. In a typical synthesis, 3.5 ml 0.5 M $SnCl_4 \cdot 5\ H_2O$ (Sigma-Aldrich) solution in water and 3.5 ml 5 M NaOH (Sigma-Aldrich) were mixed together with 12.5 mL of an ethanol (Carl Roth, p.A.)/water mixture with a ratio of 1 to 1 (v/v). After several minutes of stirring, the reaction mixture was transferred into a 100 ml Teflon liner and finally sealed in a CEM XP-1500 microwave vessel. The mixture was allowed to react in the microwave at various pressures and times (the exact conditions can be found later in the text). After cooling down radiatively for a maximum of 30 min, the obtained white-gray powders were separated by centrifugation (9000 rpm) and washed several times with water and ethanol. Finally, the powder was dried at 70°C overnight.

4.3.2 Characterization

4.3.2.1 Electron Microscopy

The products were characterized by means of transmission electron microscopy (TEM) using a Philips EM 420 with an acceleration voltage of 120 kV and a Philips TECNAI F30 with a field-emission gun and 300 kV extraction voltage, equipped with an Oxford

EDX (energy-dispersive X-ray) spectrometer with a Si/Li detector and an ultrathin window for elemental analysis. Samples for TEM measurements were prepared from ethanolic suspensions of the samples. After treatment in an ultrasound bath, one to two drops of the suspension were administered on a Cu grid coated with an amorphous carbon layer. Scanning electron microscopy (SEM) pictures were obtained using high vacuum mode SEM (Quanta 200 FEG; FEI Company, Eindhoven, the Netherlands).

4.3.2.2 X-ray Powder Diffraction

X-ray diffraction patterns (XRD) were recorded using a Bruker AXS D8 Discover with HiStar detector operating with graphite monochromatized CuKα radiation in reflection mode (point focus) and a Siemens D5000 with CuKα_1 radiation (Ge (220) monochromator) and a Braun M50 position sensitive detector operating in transmission geometry. Samples were either glued with VP/VA copolymer on top of glass substrates or fixed between two strips of 3M Scotch Magic tape. Phase analyses were performed according to the PDF-2 database (PDF-2, Release 2004, JCPDS - International Centre for diffraction Data (2004)) using EVA 10.0 [22]. Crystallite sizes were determined according to the fundamental parameter [23] approach in course of whole pattern fitting (LeBail method) using TOPAS Academic [24].

4.3.2.3 Raman Spectroscopy

Raman spectra were recorded at room temperature using a Horiba Jobin Yvon LabRAM HR spectrometer equipped with a Si-based CCD-detector (Peltier-cooled) and an integrated Olympus BX41 optical microscope. The spectra were acquired by averaging a spectrum integrated over 60 s per window in multi-window acquisition mode twice, with 200 pixel overlap.

4.3.2.4 Infrared Spectroscopy

Infrared spectra were recorded at room temperature using a Jasco FT-IR 4200. The samples were measured as KBr-discs (Merck p.a.) in transmission mode. The spectra were analyzed by Spectra Manager (Version 1.53.00; Jasco Corporation) and corrected by baseline correction and smoothing (Means-Method; convolution width of 25). Due to different linear baseline corrections, no quantitative information can be drawn from the intensity of the absorption peaks.

4.4 Results and Discussion

4.4.1 Ultra-short Heating Ramp Synthesis

Samples were prepared using the following heating times: ultra-short heating was performed with 6 min (ramp: 1 min, dwell time: 5 min), and a series of reactions times (ramps: 2.5 min and dwell times of 0 min, 1 min, 2.5 min, 5 min, 10 min, 15 min, 20 min, 30 min, 45 min, 60 min and 90 min). The samples of the ultra-short heating batch (microwave power: 1600 W) reached a pressure of 44 bar, corresponding to a temperature of about 225°C within one minute. The sample was then kept at this pressure for 5 minutes. The phase identity of the as-prepared SnO_2 nanomaterials was determined by X-ray powder diffraction. Figure 4.1 shows the XRD pattern of the SnO_2 nanorods. All diffraction lines can be attributed to Cassiterite (PDF-2, entry (41-1445) SG: $P4_2/mnm$). The TEM micrographs (Figure 4.2) show that even after this very short period of heating time and the ultra-short heating ramp, rod-shaped structures were formed. Although these particles already exhibit an anisotropic shape and are enclosed by 110 faces (see Figure 4.2), the rods are not well defined and do not show clear tips. To enhance the anisotropy of the structures and because many other morphologies were observed, the reaction time was extended. An increase of the heating time to 10 minutes (total reaction time 11 minutes) lead to an increase in the yield of anisotropic nanoparticles, see Figure 4.3. These results indicate that SnO_2 nanorods can be formed after a reaction time of only 2-3 min.

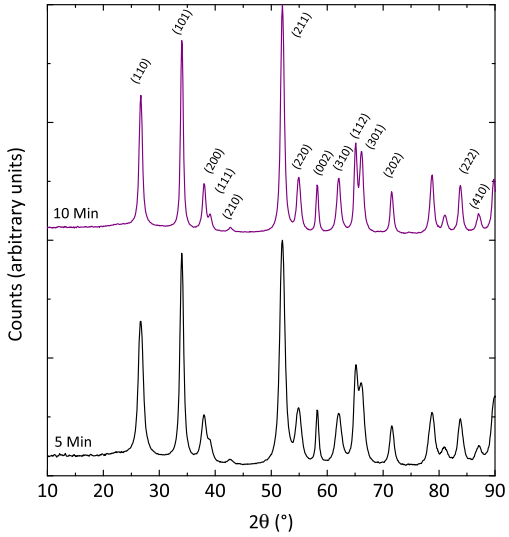

Figure 4.1: X-Ray diffraction pattern of the samples prepared with 1 minute heating ramp.

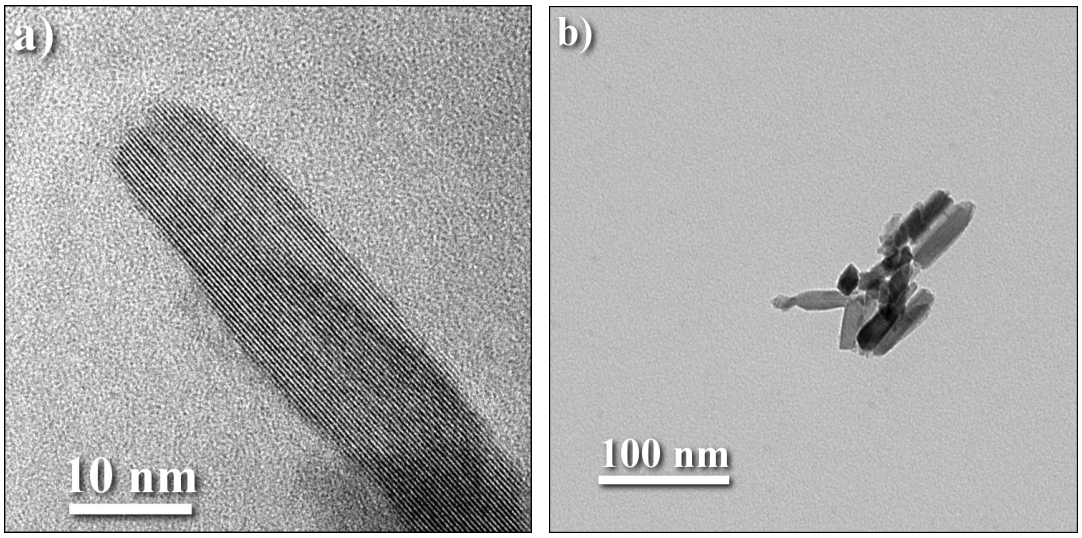

(a) **(b)**

Figure 4.2: (a) High resolution TEM image of a single SnO_2 nanorod. (b) Bundle of SnO_2 nanorods, obtained after 6 minutes of reaction time.

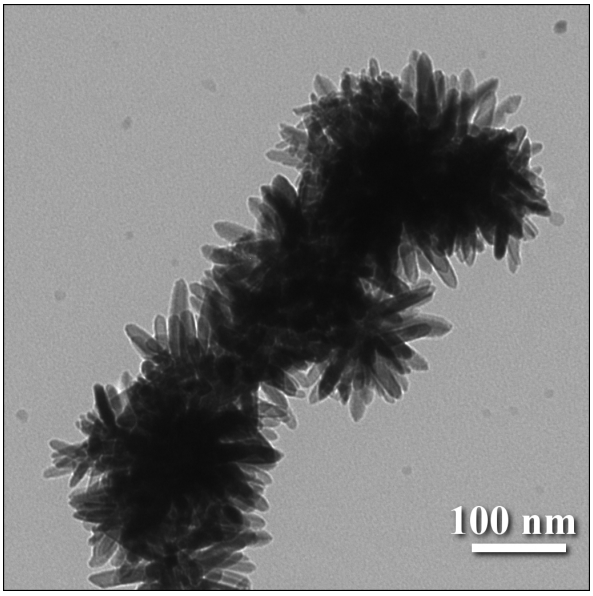

Figure 4.3: TEM image of the sample heated for 11 minutes.

4.4.2 Time-dependent Study

To enhance the yield of 1D nanostructures even further, the heating ramp was extended to 2.5 min (at 1600 W) and various reaction times (0 [i.e. only the heating ramp], 1, 2.5, 5, 10, 15, 20, 30, 45, 60 and 90 min) were investigated. The pressure was set to 46 bar, equivalent a temperature of approx. 240°C. The phase purity of all samples was confirmed by X-ray powder diffraction data (see Figure 4.4). All diffraction lines can be attributed to Cassiterite (PDF-2, entry (41-1445)). To compare the microwave reaction to a conventional solvothermal method (heated in a drying oven at 250°C), all mixtures were treated for the same amount of time in a Teflon-lined stainless steel autoclave. Even after 90 min reaction time, no nanorods were obtained from these reactions, proving that the microwave-assisted pathway provides a much faster reaction route towards one-dimensional nanostructures than conventional methods.

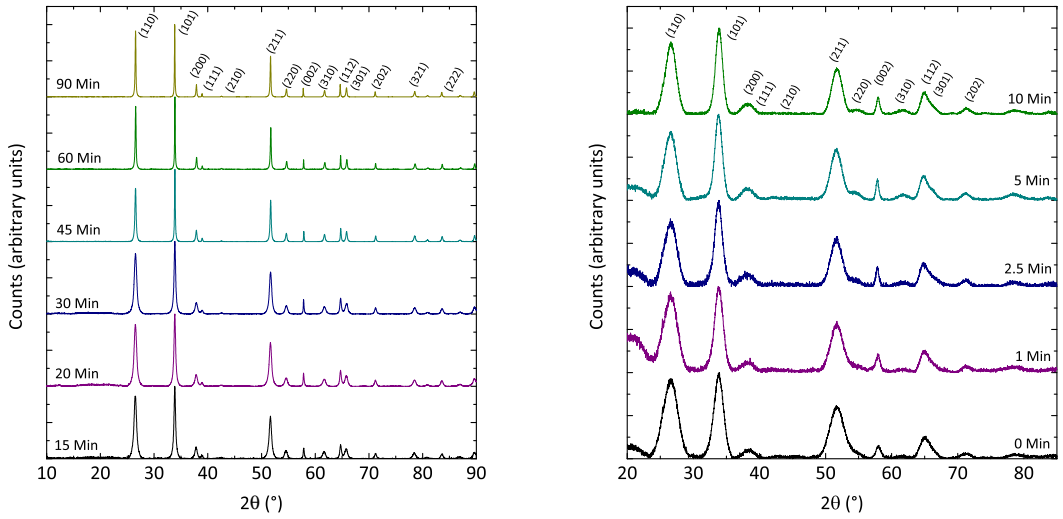

(a) **(b)**

Figure 4.4: X-Ray powder diffraction data of the as-prepared materials. (a) Diffraction data for the samples heated up to 10 min, (b) for samples heated for more than 15 min.

The powder diffraction data give a first hint towards the evolution of the growth process: The reflection profiles of samples of these early reactions are very broad and fit to one, crystallite size-dependent reflection profile broadening contribution exclusively, indicating very small, isotropic crystallites (see also Figures 4.6 (a)-(b)). Upon increasing the reaction time the profiles of all reflections narrow significantly. Furthermore, the high intensity cusp of the reflection profiles of all reflections (hkl) with $l \neq 0$ are narrower than expected for a Voigt-type profile, pointing to a crystallite size anisotropy. Thus, whole pattern fitting was performed by applying two different contributions from identical crystallographic phase information differing exclusively in the crystallite size and the individual reflection intensities. The determined values for the crystallite size are interpreted according to the short and long axis of the anisotropic, single crystalline nanoparticles (c.f. Figure 4.5).

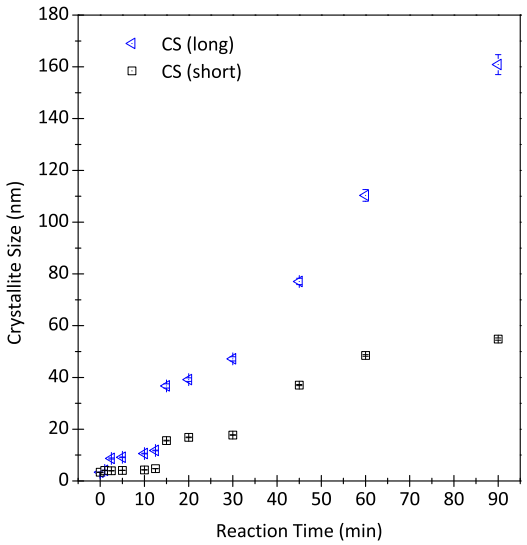

Figure 4.5: Crystallite size (CS) and anisotropy as a function of reaction time. The blue and black symbols represent the long and short axes of the anisotropic nanoparticles, respectively.

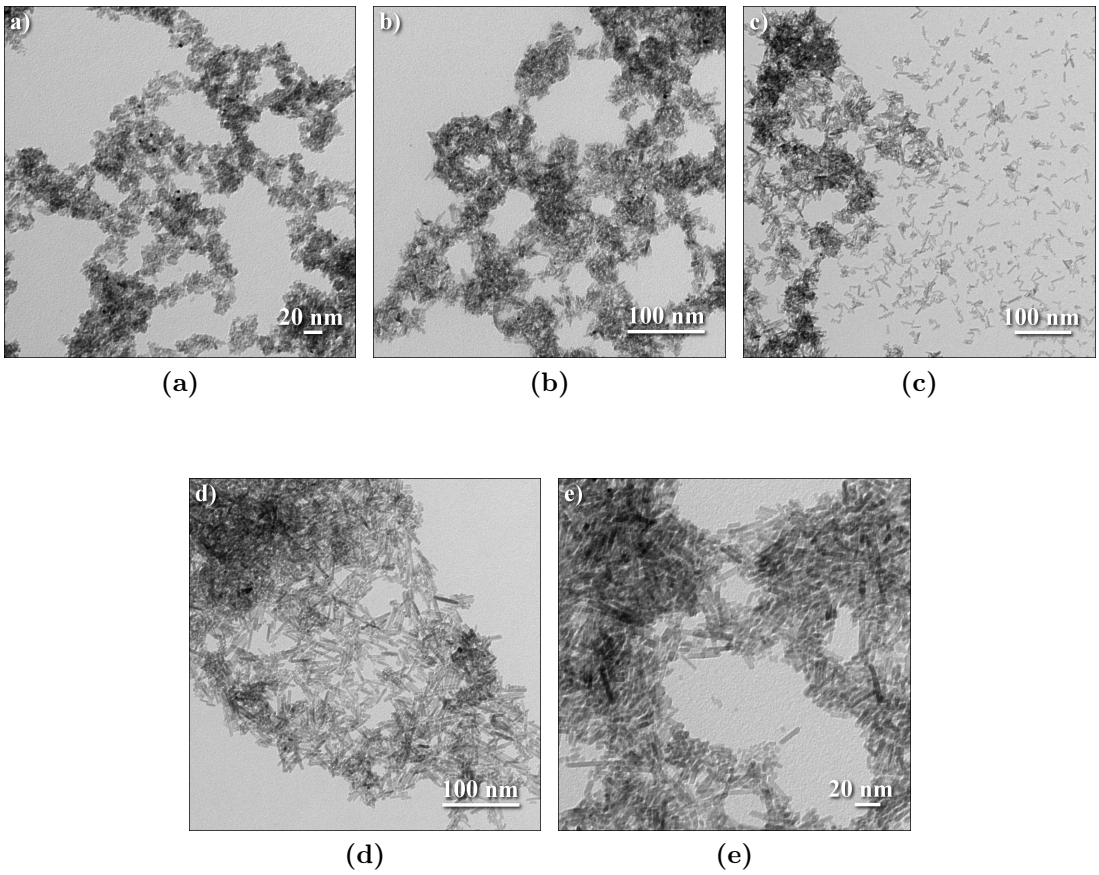

Figure 4.6: TEM micrographs of the obtained rod-shaped materials. The images correspond to reaction times of 0 (a), 1 (b), 2.5 (c), 5 (d) and 10 min (e).

To visualize the growth process of the nanorods, transmission electron microscopy images were recorded. The TEM micrographs (Figure 4.7 (a)-(f), Figure 4.6 (a)-(e)) show the morphologies of the nanorods prepared after different periods of heating.

(*i*) The TEM image of the sample heated for "0" minutes (i.e. only the heating ramp was carried out, subsequently the sample was allowed to cool down radiatively) shows very small particles with isotropic morphology. No nanorods are found yet. (*ii*) After one minute of heating time, the first anisotropic particles begin to form. Although the vast majority of the sample still contains isotropic particles, some rod-shaped particles with a small aspect ratio are observed already (Figure 4.6 (b)).

(*iii*) Reaction times of 2.5 minutes yield an increasing amount of SnO_2 nanorods (in good agreement with the X-ray diffraction data). However, the particle size is still very small (up to 20 nm in length and around 4 nm in diameter). (*iv,v*) A further increase of the reaction time to 5 and 10 minutes leads only to an increase in the amount of the anisotropic particles. (*vi*) The actual growth of the nanorods (indicated by the "jump" of the particle size in the time slot between 10 and 15 minutes in Figure 4.5) begins after a total reaction time of 17.5 min [2.5 min ramp and 15 min at 46 bar]. Now the majority of the particles is rod-shaped, see Figure 4.7. However, particles with other morphologies (cubes and irregular particles) are still present.

Tin dioxide nanorods are formed only, when sodium counter ions are present in the reaction medium, whereas potassium rubidium or cesium lead to the formation of platelets, mixtures of various rod-like structures with a very low aspect ratio or spheres. Thus, the discussion about the mechanism of morphology control have to include also the adsorption-energy E_{Ad} and -probabilities of the base cations on the 110 surface of SnO_2 [25]. The interaction between the SnO_2 surfaces and the adsorbed cations is dictated by the coulomb interaction. This interaction is mainly determined by the charge-to-radius-ratio of the adsorbed ions and therefore explicable in terms of the Pearson concept [26–30] of hard and soft acids and bases (HSAB).

In addition to the morphological heterogeneity, the TEM pictures show that the enclosing crystal faces are not yet well defined. Although the anisotropic morphology is clearly visible and the enclosing faces of most rods belong to the {110} zone, the rods do not possess very sharp and distinct tips (see Figure 4.8). Furthermore, rods with different growth orientations are observed after rather short reaction times (15 and 20 minutes [17.5 and 22.5 min including the heating ramp]).

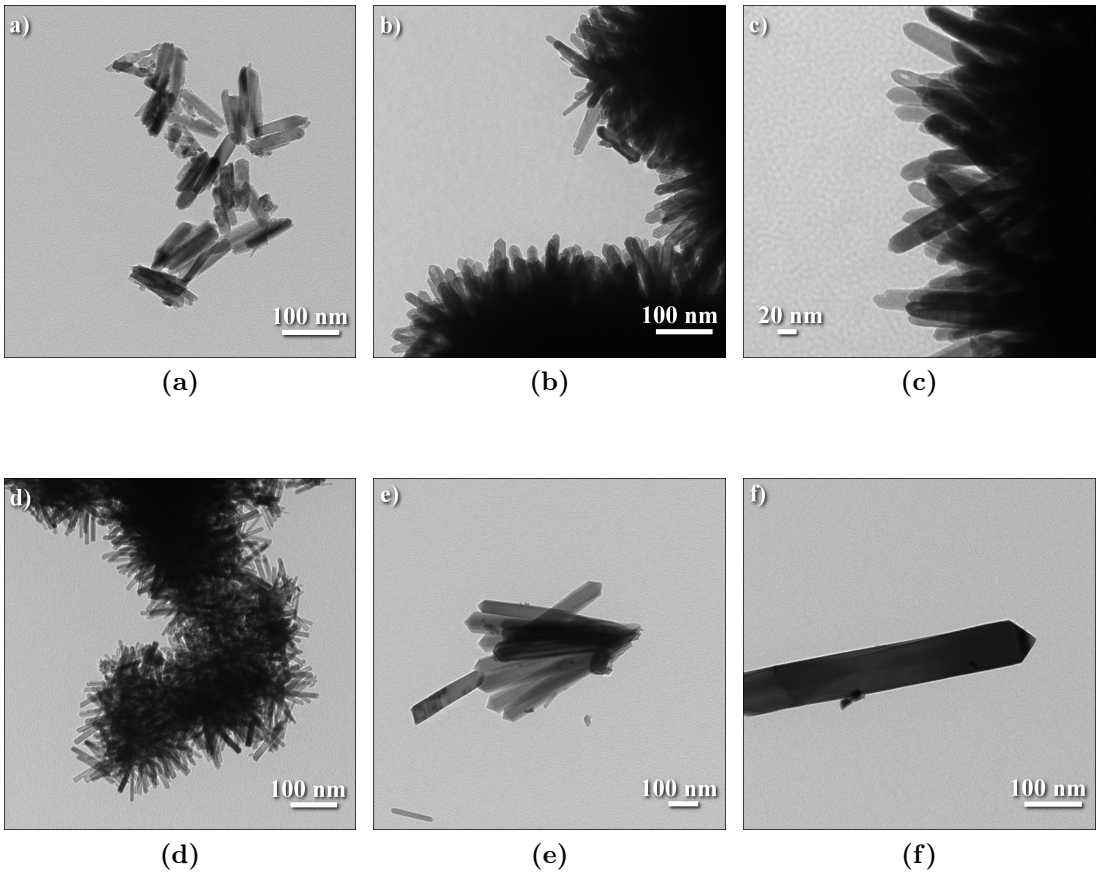

Figure 4.7: TEM micrographs of the obtained rod-shaped materials. The images correspond to reaction times of 15 (a), 20 (b), 30 (c), 45 (d), 60 (e) and 90 min (f).

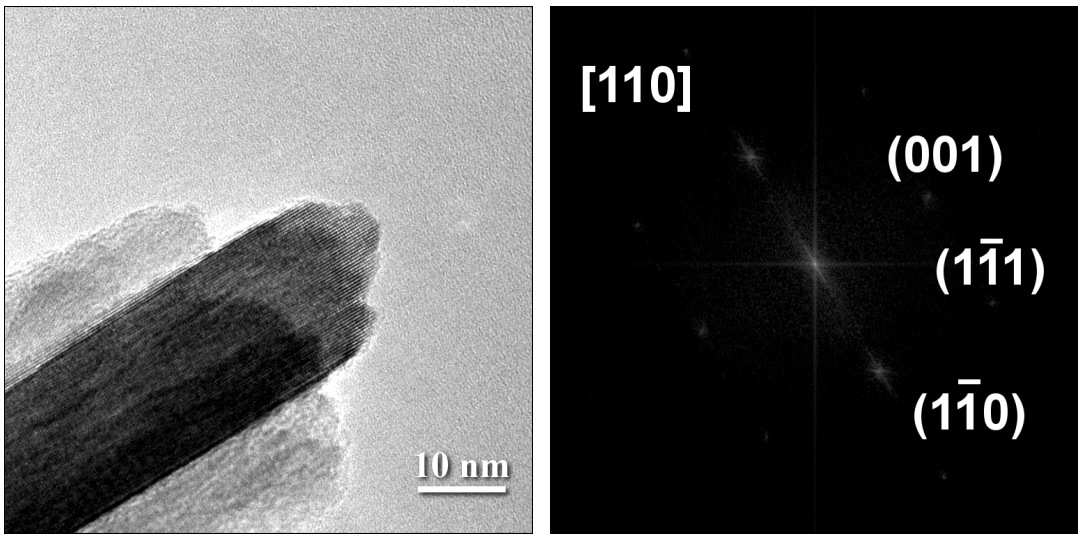

(a) **(b)**

Figure 4.8: (a) HR-TEM picture of a SnO_2 nanorod obtained after 15 min of reaction time. (b) Fourier transform with indices for the corresponding reciprocal lattice points according to the crystal structure model of Cassiterite.

Figure 4.9 shows HR-TEM pictures of SnO_2 nanorods obtained after 20 min of reaction time. The Fourier transforms in Figure 4.9 (b) clearly indicate that the crystals are terminated by the 020 faces but not the 110 face as expected for Cassiterite. However, in this case, the growth direction is [001] as well. The edges of the rod are not well defined. Upon increasing the reaction time (30 and 45 min), the nanoparticles grow in size (length and width) and the crystallinity increases (see Figure 4.10). In addition, less nanorods with an orientation that differs from [001] as the growth direction and {110} as the enclosing faces are found in the samples [25].

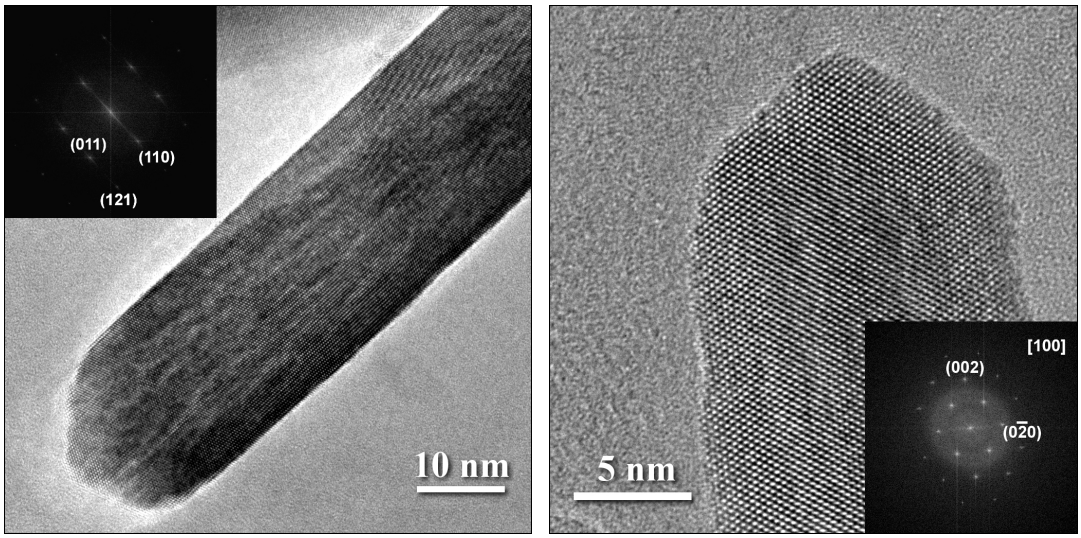

(a) **(b)**

Figure 4.9: HR-TEM pictures of SnO_2 nanorods (20 min), insets show Fourier transformation and indexing of the corresponding reciprocal lattice points (cassiterite).

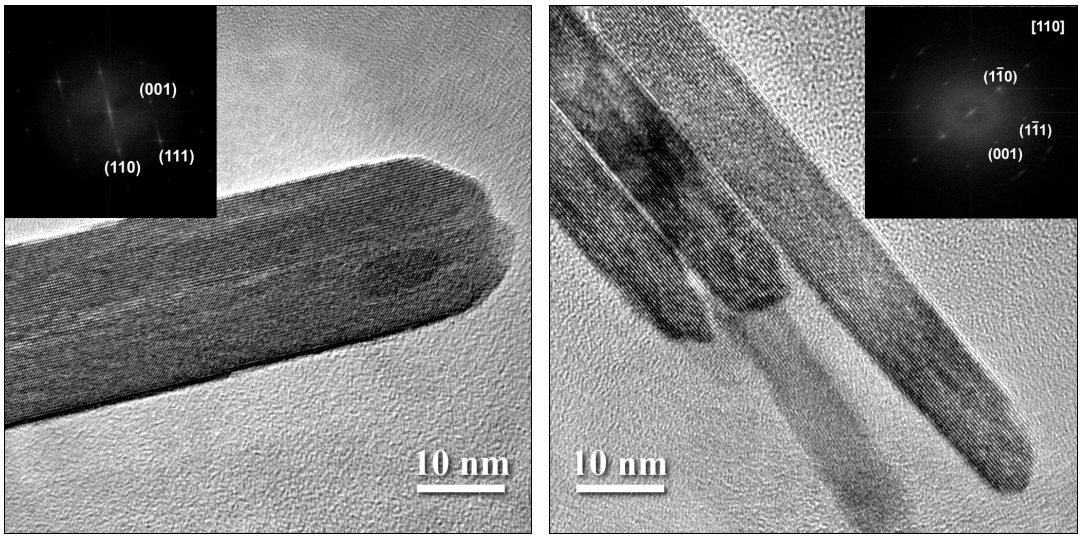

(a) **(b)**

Figure 4.10: HR-TEM pictures of SnO_2 nanorods after 30 min (a) and 45 min (b) insets show Fourier transformation and indexing of the corresponding reciprocal lattice points (Cassiterite).

It was noted that the cation of the base has a great influence on the particle growth [25]. The enclosing faces of a crystal are usually those with the lowest growth rate (i.e. the lowest surface energy) [31]; the surface energy is strongly affected by foreign ions adsorbed to the crystal faces. The adsorption energies of the alkali metal cations decrease with increasing atomic number. In general, the growth of Cassiterite-type SnO_2 is anisotropic with a rod-like morphology. This morphology, however, is only observed if crystallization is carried out under equilibrium conditions, i.e. at high temperature and long crystallization times. Under the conditions described here these optimum growth conditions are certainly not met. Therefore spherical or non-anisotropic morphologies are observed in the early stages of the crystallization. The high adsorption probability of Na^+ cations on the 110 face (also compared to the other crystal surfaces) facilitates the rod formation even under *non-optimum* conditions.

After a reaction time of 60 min, almost all of the investigated nanorods are enclosed by the 110 crystal faces of SnO_2 which is known to be the most stable surface of the Cassiterite/rutile structure-type in aqueous or basic solution due to its polarity [32–34] (see Figure 4.11). These results are in line with studies of the thermal dehydration of a SnO_2 gel by Harrison and Guest [35] using infrared (IR) spectroscopy and X-ray diffraction.

Crystalline bulk SnO_2 exhibits (110), (101) and (100) planes in the ratio 3:1:1. A reaction time of 90 min eventually leads to a sample that consists almost entirely (see Figure 4.12) of highly crystalline SnO_2 nanorods with a [001] growth direction, enclosing faces from the {110} zone and clearly pronounced edges and tips (see Figure 4.13). The Fourier transform of this image shows sharp bright spots, indicating a high degree of crystallinity. The results can be interpreted in terms of hydroxylated exposed 100, 101 (both of which contain clusters of three hydroxyl groups attached to each surface tin atom) and 110 (which contains both isolated and geminal pairs of hydroxyl groups

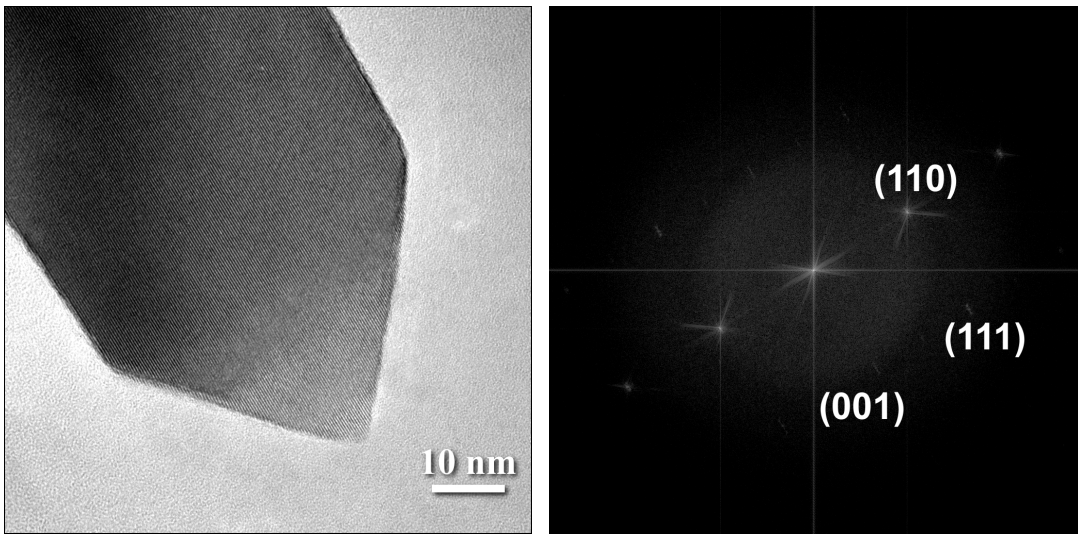

(a) **(b)**

Figure 4.11: Nanorods after 60 min (a) and FFT showing the enclosing crystal faces (b)

attached to surface tin atoms, unidentate hydroxyl groups whose Sn-O bond axis is orthogonal to the plane, [defined in Ref. [35] as terminal OH groups] and geminal pairs of hydroxyl groups attached to surface tin atoms) crystal planes of the rutile structure, the former ones predominating.

In summary, one can clearly show that the growth process of the nanorods starts from initially formed crystalline materials after very short reaction times (15 and 20 min). However, many crystal morphologies, like spheres and cubes, are found in the samples, and the anisotropic structures do not yet exhibit very pronounced edges and tips. In addition, orientations that differ from the most prominent growth direction [001] with {110} zone as the lateral limit are found.

Reaction times of 30 min and more lead to nanorods in higher quantities (containing less morphological impurities) with well defined edges and tips that look smoother and "rounder". The overall crystallite size (determined from the XRD analyses) only increases slowly. After another 15 min (a total of 45 min) the crystal size increases faster

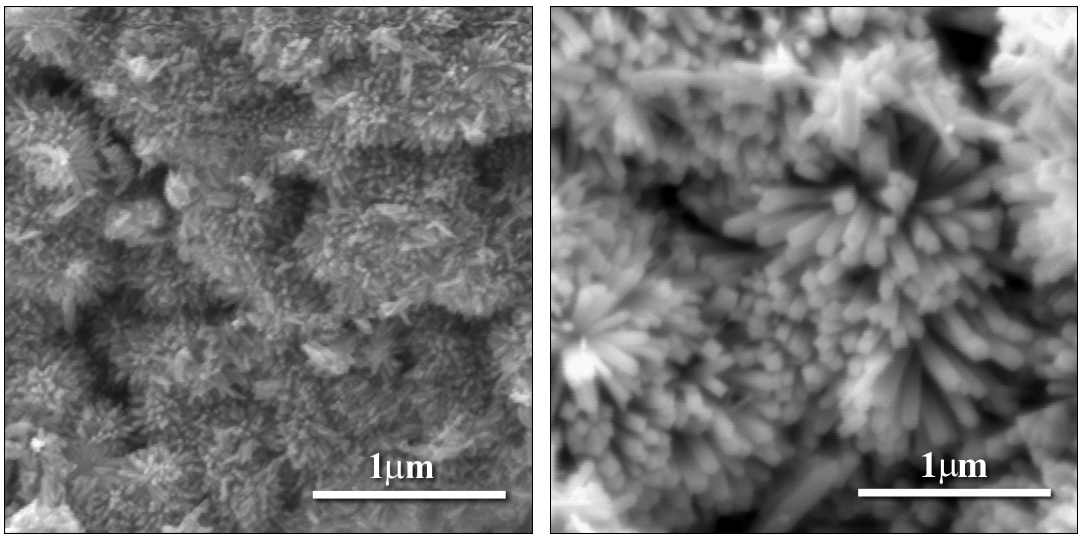

(a) **(b)**

Figure 4.12: (a) SEM overview picture of nanorods after 20 min; (b) SEM overview picture of nanorods after 90 min.

which points to a faster volume growth of the rods and a further improved morphological homogeneity (see Figure 4.7 (d)). The edges and tips are more pronounced. Upon even longer reaction times (60 and finally 90 min) a significant increase in both, the size of the rods (see TEM pictures and XRD fits) and the crystallinity, is observed. The edges and especially the tips are very clearly pronounced and always oriented along the enclosing {110} -faces. Therefore, a morphological growth process is proposed, starting from ill-defined anisotropic rod-shaped structures proceeded by Ostwald ripening (see Figure 4.14). As long as there is amorphous and ill-defined SnO_2 present, the growth of SnO_2 nanocrystals proceeds fast. After this reservoir of reactive material is used up, crystal growth proceeds more slowly as a re-dissolution and re-crystallization process of the crystals is required. The critical factor is the chemical potential of the individual nanocrystal; in a dynamic process only well-ordered and defect-free crystals are formed eventually.

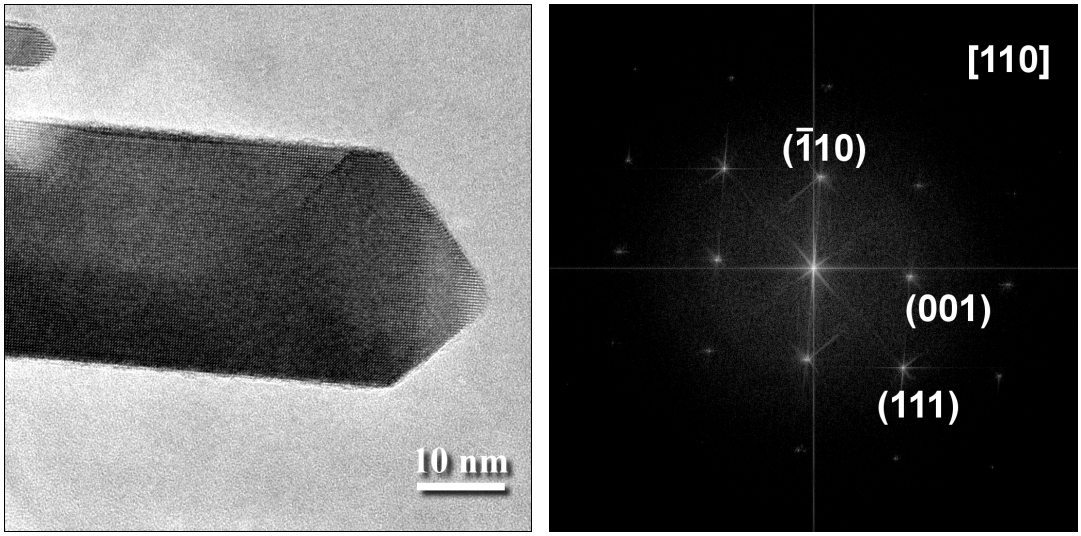

(a) **(b)**

Figure 4.13: (a) HR-TEM picture of a nanorod heated for 90 minutes. (b) Fourier transformation and indexing of the corresponding reciprocal lattice points (cassiterite).

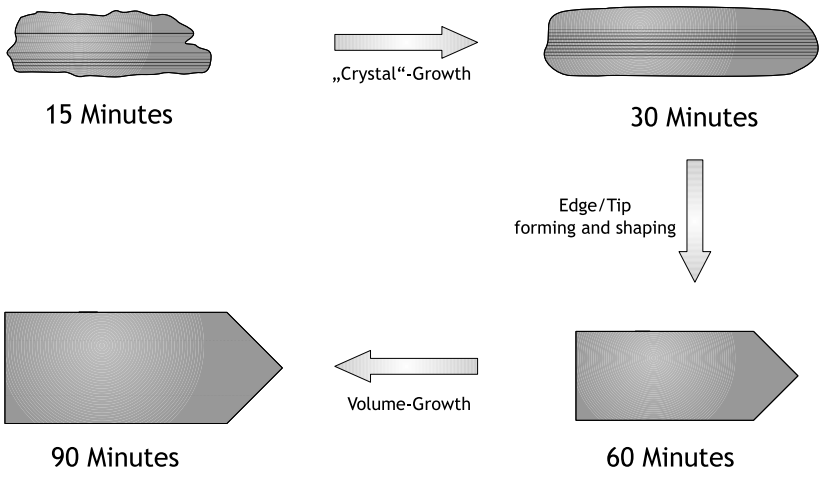

Figure 4.14: Proposed growth evolution of the SnO_2 nanorods.

Since many applications of tin dioxide are found in optoelectronic devices, the optical properties of the various nanostructured SnO_2 samples were investigated using Raman and IR spectroscopy. Raman spectra were recorded from samples after 15 minutes of growth time, because only here the relevant phonon modes can be detected. The corresponding spectra are shown in Figure 4.15.

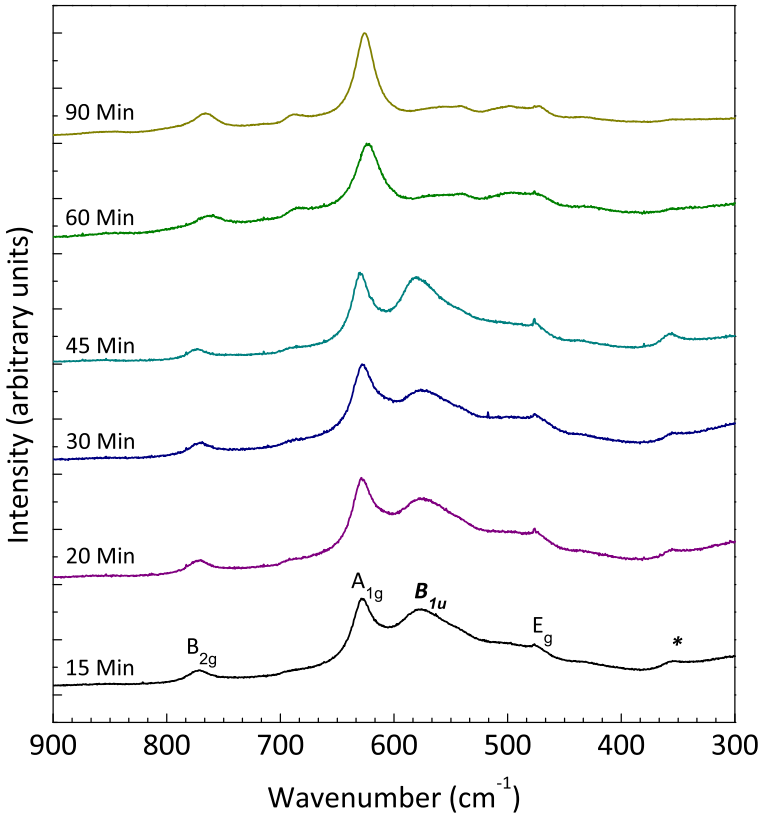

Figure 4.15: Raman-spectra of the samples prepared at 46 bar.

It is evident that the Raman behavior of the materials changes with increasing size of the anisotropic particles. The Raman active modes A_{1g}, B_{2g} and E_g appear in all samples at around $626\,cm^{-1}$, $769\,cm^{-1}$ and $474\,cm^{-1}$ respectively (Table 4.1 for the exact positions for each sample). In addition to these modes which can also be found

in bulk SnO_2, the samples containing smaller nanorods as well as smaller particles (rods at the beginning of the growth process) exhibit features in the Raman spectra that are typical for very small crystallite sizes. Those modes, B_{1u} and the mode marked with (*) can only be found in samples where the surface to volume ratio is large, making the surface modes more prominent in comparison to the (bulk) volume modes. The bands are around $576\,cm^{-1}$ and $354\,cm^{-1}$ respectively. As the nanorods grow in size and only the tip was/is small enough to show "surface" modes, these Raman modes disappear, which agrees with other reports found in the literature [36–38]. It also points towards the fact that the samples become more homogeneous since fewer morphological side-products are found, i.e. that the sample consists only of larger nanorods.

Table 4.1: Exact positions of the various Raman modes observed in the samples

	Raman mode (cm^{-1})					
Sample	*	$\mathbf{E}_g$	$\mathbf{B}_{1u}$	$\mathbf{A}_{1g}$	$\mathbf{A}_{2u}$	$\mathbf{B}_{2g}$
15 min	355	477	576	628	694	771
20 min	355	476	573	628	693	770
30 min	354	476	576	628	694	768
45 min	355	477	578	629	694	769
60 min	-	477	-	624	-	767
90 min	-	471	-	625	689	767

All SnO_2 samples exhibit an intense and broad IR absorption band in the range of 3600 to $2600\,cm^{-1}$ with a maximum at $3440\,cm^{-1}$ indicating the presence of adsorbed water (see Figure 4.17). Furthermore, all spectra show weak absorption bands at $2924\,cm^{-1}$, $2850\,cm^{-1}$ and $1635\,cm^{-1}$ arising from the KBr (see Figure 4.16). The absorption bands below $800\,cm^{-1}$ are assigned to the absorptions of the SnO_2.

As indicated in Ref. [39] for SnO_2 crystals in rutile structure with space group $P4_2/mnm$, the zone centre IR active modes in the point group D_{4h} are E_u $618\,cm^{-1}$ (TO) and $770\,cm^{-1}$(LO); A_{2u} at $477\,cm^{-1}$ (TO) and $705\,cm^{-1}$ (LO) (TO: mode of

transversal optical phonons; LO: mode of longitudinal optical phonons). The A_{2u} (TO) vibrations originate from the symmetric and anti-symmetric Sn-O-Sn stretching modes. For the present samples one of these absorptions is found around $500\,cm^{-1}$. The shift from the corresponding band at $477\,cm^{-1}$ (found in earlier studies in crystals of bulk SnO_2) [39] is due to different size and shape [40].

For the samples with a reaction time of 15, 60 and 90 min, a further band is observed at about $520\,cm^{-1}$, which is assigned to a surface vibration mode without specific symmetry. The 15 min, 20 min and 30 min reaction time samples have an absorption band at around $650\,cm^{-1}$. According to Ref. [41], this band corresponds to the E_u (TO) mode. Remarkably, the maximum shifts to higher wavenumbers upon increasing reaction time ($641\,cm^{-1}$, $649\,cm^{-1}$ and $652\,cm^{-1}$) indicating a higher crystallinity. The band also broadens with increasing reaction times (up to 45 min) where a second maximum at higher wave numbers arises ($657\,cm^{-1}$ and $662\,cm^{-1}$). The latter is assigned to be the A_{2u} (LO) mode.

With the increase of reaction time, a further maximum arises at higher wavenumbers which corresponds to the E_u(LO) (60 min: $630\,cm^{-1}$, $656\,cm^{-1}$ and $683\,cm^{-1}$; 90 min: $632\,cm^{-1}$, $656\,cm^{-1}$, $671\,cm^{-1}$ and $690\,cm^{-1}$), see Figure 4.17.

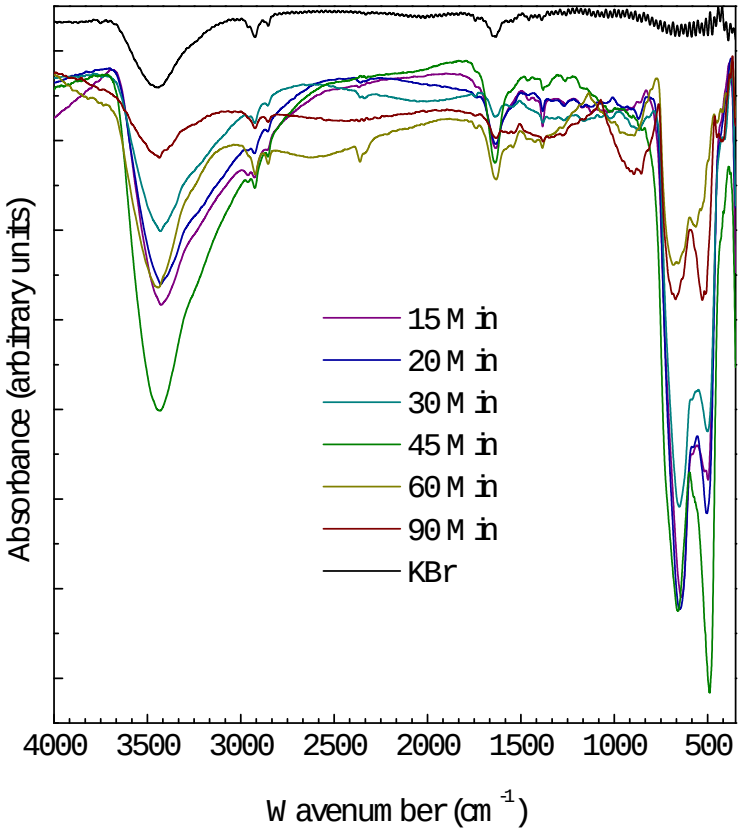

Figure 4.16: Normalized FT-IR-spectra of the samples prepared at 46 bar.

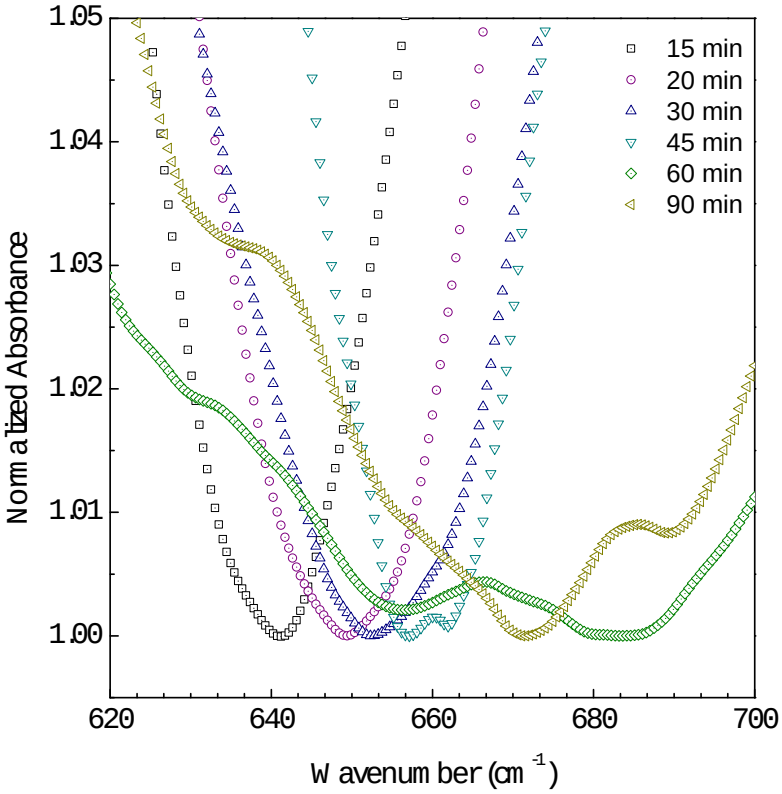

Figure 4.17: Normalized FT-IR-spectra (in the range between 600 and 700 cm^{-1}) of the samples prepared at 46 bar.

4.5 Conclusion

A simple and very fast microwave assisted reaction was used to monitor the growth process of SnO_2 nanocrystals by taking "snapshots" of reaction intermediates. X-Ray powder diffraction data clarified the phase composition and full pattern profile fitting (LeBail) gave a first hint towards the growth process of the one-dimensional nanostructures. (HR)-TEM measurements revealed that the SnO_2 nanorods start growing from crystalline yet ill-defined anisotropic (rod-like) structures. These structures grow by Ostwald ripening until the final morphology is reached (after 45-60 minutes). As long as there is amorphous SnO_2 present, the growth of SnO_2 nanocrystals proceeds fast. After this reservoir of reactive material is used up, crystal growth proceeds more slowly as a re-dissolution and re-crystallization process of the crystals is required. The optical properties of the products were investigated using FT-IR and Raman spectroscopy. It could be demonstrated that the IR and Raman behavior is closely related to the evolution of the growth process, i.e. with increasing reaction time the anisotropy increases until after 60 min the crystallization is complete.

References

[1] B. Falabretti and J. Robertson. Electronic structures and doping of SnO_2, $CuAlO_2$, and $CuInO_2$. *Journal of Applied Physics*, 102(12):123703–1, 2007.

[2] Y. J. Chen, X. Y. Xue, Y. G. Wang, and T. H. Wang. Synthesis and ethanol sensing characteristics of single crystalline SnO_2 nanorods. *Applied Physics Letters*, 87(23):3, 2005.

[3] B. Cheng, J. M. Russell, W. S. Shi, L. Zhang, and E. T. Samulski. Large-scale, solution-phase growth of single-crystalline SnO_2 nanorods. *Journal of the American Chemical Society*, 126(19):5972–5973, 2004.

[4] Z. H. Zhong, D. L. Wang, Y. Cui, M. W. Bockrath, and C. M. Lieber. Nanowire crossbar arrays as address decoders for integrated nanosystems. *Science*, 302(5649):1377–1379, 2003.

[5] Z. W. Pan, Z. R. Dai, and Z. L. Wang. Nanobelts of semiconducting oxides. *Science*, 291(5510):1947–1949, 2001.

[6] X. F. Duan, C. M. Niu, V. Sahi, J. Chen, J. W. Parce, S. Empedocles, and J. L.

Goldman. High-performance thin-film transistors using semiconductor nanowires and nanoribbons. *Nature*, 425(6955):274–278, 2003.

[7] Z. R. Dai, J. L. Gole, J. D. Stout, and Z. L. Wang. Tin oxide nanowires, nanoribbons, and nanotubes. *Journal of Physical Chemistry B*, 106(6):1274–1279, 2002.

[8] M. Law, H. Kind, B. Messer, F. Kim, and P. D. Yang. Photochemical sensing of NO_2 with SnO_2 nanoribbon nanosensors at room temperature. *Angewandte Chemie-International Edition*, 41(13):2405–2408, 2002.

[9] G. X. Wang, J. S. Park, M. S. Park, and X. L. Gou. Synthesis and high gas sensitivity of tin oxide nanotubes. *Sensors and Actuators B-Chemical*, 131(1, Sp. Iss. SI):313–317, 2008.

[10] H. Z. Wang, J. B. Liang, H. Fan, B. J. Xi, M. F. Zhang, S. L. Xiong, Y. C. Zhu, and Y. T. Qian. Synthesis and gas sensitivities of SnO_2 nanorods and hollow microspheres. *Journal of Solid State Chemistry*, 181(1):122–129, 2008.

[11] Y. L. Wang, X. C. Jiang, and Y. N. Xia. A solution-phase, precursor route to polycrystalline SnO_2 nanowires that can be used for gas sensing under ambient conditions. *Journal of the American Chemical Society*, 125(52):16176–16177, 2003.

[12] Y. S. He, J. C. Campbell, R. C. Murphy, M. F. Arendt, and J. S. Swinnea. Electrical and Optical Characterization of $SbSnO_2$. *Journal of Materials Research*, 8(12):3131–3134, 1993.

[13] L. Vayssieres and M. Grätzel. Highly ordered SnO_2 nanorod arrays from controlled aqueous growth. *Angewandte Chemie-International Edition*, 43(28):3666–3670, 2004.

[14] G. R. A. Kumara, K. Tennakone, I. R. M. Kottegoda, P. K. M. Bandaranayake, A. Konno, M. Okuya, S. Kaneko, and K. Murakami. Efficient dye-sensitize photoelectrochemical cells made from nanocrystalline Tin(IV) oxide-zinc oxide composite films. *Semiconductor Science and Technology*, 18(4):312–318, 2003.

[15] J. Qian, P. Liu, Y. Xiao, Y. Jiang, Y. Cao, X. Ai, and H. Yang. TiO_2-Coated Multilayered SnO_2 Hollow Microspheres for Dye-Sensitized Solar Cells. *Advanced Materials*, 21(36):3663–3667, 2009.

[16] H. J. Snaith and C. Ducati. SnO_2-Based Dye-Sensitized Hybrid Solar Cells Exhibiting Near Unity Absorbed Photon-to-Electron Conversion Efficiency. *Nano Letters*, 10(4):1259–1265, 2010.

[17] D. F. Zhang, L. D. Sun, J. L. Yin, and C. H. Yan. Low-temperature fabrication of highly crystalline SnO_2 nanorods. *Advanced Materials*, 15(12):1022–1025, 2003.

[18] H. Katsuki, A. Shiraishi, S. Komarneni, W. J. Moon, S. Toh, and K. Kaneko. Rapid Synthesis of Monodispersed α-Fe_2O_3 Nanoparticles from $Fe(NO_3)_3$ Solution by Microwave Irradiation. *Journal of the Ceramic Society of Japan*, 112(1307):384–387, 2004.

[19] S. Komarneni, M. C. D'Arrigo, C. Leonelli, G. C. Pellacani, and H. Katsuki. Microwave-Hydrothermal Synthesis of Nanophase Ferrites. *Journal of the American Ceramic Society*, 81(11):3041–3043, 1998.

[20] A. Michailovski, J. D Grunwaldt, A. Baiker, R. Kiebach, W. Bensch, and G. R. Patzke. Studying the Solvothermal Formation of MoO_3 Fibers by Complementary In Situ EXAFS/EDXRD Techniques. *Angewandte Chemie-International Edition*, 44(35):5643–5647, 2005.

[21] L. Qin, J. Xu, X. Dong, Q. Pan, Z. Cheng, Q. Xiang, and F. Li. The template-free synthesis of square-shaped SnO_2 nanowires: the temperature effect and acetone gas sensors. *Nanotechnology*, 19(18), 2008.

[22] EVA 10.0, 2003.

[23] R. W. Cheary and A. Coelho. A fundamental parameters approach to X-ray line-profile fitting. *Journal of Applied Crystallography*, 25(2):109–121, 1992.

[24] A. Coelho. TOPAS Academic, V.1.0, 2004.

[25] A. Birkel, N. Loges, E. Mugnaioli, R. Branscheid, D. Koll, S. Frank, M. Panthöfer, and W. Tremel. Interaction of Alkaline Metal Cations with Oxidic Surfaces: Effect on the Morphology of SnO_2 Nanoparticles. *Langmuir*, 26(5):3590–3595, 2010.

[26] R. G. Pearson. Absolute electronegativity and hardness: application to inorganic chemistry. *Inorganic Chemistry*, 27(4):734–740, 1988.

[27] S. Pal and K. R. S. Chandrakumar. Critical Study of Local Reactivity Descriptors for Weak Interactions: Qualitative and Quantitative Analysis of Adsorption of Molecules in the Zeolite Lattice. *Journal of the American Chemical Society*, 122(17):4145–4153, 2000.

[28] R. G. Pearson. Hard and soft acids and bases, HSAB, part 1: Fundamental principles. *Journal of Chemical Education*, 45:581–587, 1968.

[29] A. Alfarra, E. Frackowiak, and Béguin F. The HSAB concept as a means to interpret the adsorption of metal ions onto activated carbons. *Applied Surface Science*, 228(1-4):84–92, 2004.

[30] M. Wisniewski and P. A. Gauden. The HSAB principle as a means to interpret the reactivity of carbon nanotubes. *Applied Surface Science*, 255(9):4782 – 4786, 2009.

[31] R. Gross. Zur Theorie des Wachstums- und Lösungsvorganges kristalliner Materie. In *Abh. d. math.-phys. Klasse der sächs. Ges. der Wiss.*, volume 35, pages 137–202. Leipzig, 1918.

[32] G. Lagaly, O. Schulz, and R. Zimehl. *Dispersionen und Emulsionen: Eine Einführung in die Kolloidik feinverteilter Stoffe einschließlich der Tonminerale*. Steinkopff, Darmstadt, 1997.

[33] P. I. Sorantin and K. Schwarz. Chemical Bonding in Rutile-Type Compounds. *Inorganic Chemistry*, 31(4):567–576, 1992.

[34] J. Muscat, V. Swamy, and N. M. Harrison. First-principles calculations of the phase stability of TiO_2. *Physical Review B*, 65(22), 2002.

[35] P. G. Harrison and A. Guest. Tin oxide surfaces. Part 17. - An infrared and thermogravimetric analysis of the thermal dehydration of Tin(IV) oxide gel. *Journal of the Chemical Society - Faraday Transactions I*, 83(Part 11):3383–3397, 1987.

[36] V. Subramanian, W. W. Burke, H. Zhu, and B. Wei. Novel Microwave Synthesis of Nanocrystalline SnO_2 and Its Electrochemical Properties. *Journal of Physical Chemistry C*, 112(12):4550–4556, 2008.

[37] J. X. Zhou, M. S. Zhang, J. M. Hong, and Z. Yin. Raman spectroscopic and photoluminescence study of single-crystalline SnO_2 nanowires. *Solid State Communications*, 138(5):242–246, 2006/5.

[38] L. Abello, B. Bochu, A. Gaskov, S. Koudryavtseva, G. Lucazeau, and M. Roumyantseva. Structural Characterization of Nanocrystalline SnO_2 by X-Ray and Raman Spectroscopy. *Journal of Solid State Chemistry*, 135(1):78–85, 1998.

[39] H. Zhang, Y. Liu, K. Zhu, G. Siu, Y. Xiong, and C. Xiong. Fourier transform infrared characterization of nanometre SnO_2. *Journal of Physics: Condensed Matter*, 10(48):11121, 1998.

[40] J. Zhu, Z. Lu, S. T. Aruna, D. Aurbach, and A. Gedanken. Sonochemical Synthesis of SnO_2 Nanoparticles and Their Preliminary Study as Li Insertion Electrodes. *Chemistry of Materials*, 12(9):2557–2566, 2000.

[41] X. S. Peng, G. W Zhang, L. D. and. Meng, Y. T. Tian, Y. Lin, B. Y. Geng, and S. H. Sun. Micro-Raman and infrared properties of SnO_2 nanobelts synthesized from Sn and SiO_2 powders. *Journal of Applied Physics*, 93(3):1760–1763, 2003.

5

Microwave-assisted Synthesis of SnO_2 Nanoparticles and their Application in Dye-Sensitized Solar Cells

5.1 Abstract

Tin (IV) oxide nanoparticles with a variety of morphologies for the application as anode material in dye-sensitized solar cells were prepared using a simple, fast and energy saving microwave-assisted reaction. Morphology control was achieved through the variation of the precursor base which is known to have a strong influence on the growth process of SnO_2 nanostructures. The obtained materials were investigated using X-ray diffraction (XRD), transmission electron microscopy (TEM) and scanning electron microscopy (SEM). BET isotherms were applied to determine the surface area. A simple and cheap way to prepare a semiconducting paste, needed for the coating of the photoanode, is developed and presented. Finally, the photovoltaic performance of the synthesized nanoparticles in dye-sensitized solar cells was investigated. Very high efficiencies of up to 2.8% could be achieved, which is among the highest reported values for cells based on unmodified SnO_2 nanomaterials.

5.2 Introduction

The applied nanostructures, including their materials properties and the interfaces in dye-sensitized solar cells [1–3] (DSSCs) are considered to be one of the major factors in determining the photovoltaic performance of these types of cells. In particular, efficient charge transport in the semiconductor, i.e. low recombination rates and scattering at the interface are required [4, 5].

In the most efficient DSSCs, TiO_2 nanoparticles are widely used as photoanodes and substrates for dye molecules due to their high device performance, based on large surface area and an appropriate band-gap position [2, 6–8]. However, other oxides [9] such as ZnO [10, 11], Nb_2O_5 [12, 13] and SnO_2 [10, 14–16] have also been used. Tin oxide is a stable, n-type, wide band-gap semiconductor [17] (E_g = 3.6 eV, at 300 K) with excellent optical and electrical properties [18], such as fast electron conductivity [19–21] (that are orders of magnitudes higher than TiO_2) and high stability, even under long-term UV-radiation [22]. Nanostructured SnO_2 materials have been extensively investigated as regards their applications in DSSCs [23].

However, SnO_2-based DSSCs were developed with less success in comparison to other semiconductors, and the power conversion efficiencies of cells employing SnO_2 photoelectrodes reported so far are inferior to those of TiO_2 [15]. This has mostly been attributed to the faster electron recombination in SnO_2 layers and less strong adsorption of dyes with acidic carboxyl groups [4, 24]. Additionally, in the case of SnO_2, low V_{oc} values are usually observed. This has been attributed to the intrinsically lower energy of the conduction band level, compared to TiO_2 [7, 25–27]. Since the open circuit voltage is a crucial factor in the performance of the dye-sensitized solar cell, attempts are made to improve this low V_{oc}.

Theoretically, however, SnO_2 electrodes can achieve similar or better performance if the mentioned interfacial problems could be overcome. One possibility to optimize the properties is through surface modification of nanomaterials or morphology control [15, 16, 22, 24, 28]. In this chapter, the investigation of the performance of different SnO_2 nanostructures in DSSCs will be presented. Samples possessing different morphologies have been prepared using a fast, facile and energy-efficient microwave-assisted technique. The electrochemical properties, such as charge transport in the SnO_2-based anode and SnO_2/electrolyte interface properties, were elucidated using current-voltage characteristics measurements as well as IPCE (incident photon-to-current conversion efficiency).

5.3 Experimental

5.3.1 Materials

All materials were used without further purification or treatment. $SnCl_4 \cdot 5\ H_2O$ (98%) was purchased from Sigma Aldrich. The precursor base solutions were prepared by mixing the appropriate amounts of NaOH (≥99%), KOH (≥90%), Tetramethylammonium hydroxide (TMAH; 25% w/w in water) and NH_4OH (25%), all Sigma Aldrich, with MilliQ water. Ethanol (p.A.) was purchased from Carl Roth and VWR. PEG 400 and PEG 20000 were obtained from Sigma Aldrich. Triton-X-100 was obtained from Acros Organics. Chemicals used for the fabrication of the solar cells included, MPII (1-methyl-3-propylimidazoliumiodide, C-TRI), N719 (Solaronix), tBP (4-tertbutylpyridine, Aldrich), and GuSCN (guanidinium thiocyanate, Sigma). Acetonitrile and t-butanol were obtained from Sigma-Aldrich.

5.3.2 Preparation of SnO_2 Nanoparticles

Nanoparticles were prepared using a microwave-assisted method. The detailed procedure for this method was derived from syntheses described in our previous work [29]: In a typical procedure, 3.5 ml 0.5 M tin(IV) chloride solution in water and 3.5 ml 5 M NaOH (or KOH or TMAH[1] or NH_4OH) were mixed together with 12.5 ml of an ethanol/water mixture with a ratio of 1 to 1 (v/v). After several minutes of stirring, the reaction mixture was transferred into a 100 ml Teflon liner and finally sealed in a CEM XP-1500 microwave vessel. After a heating ramp of 10 minutes, the reaction mixture was allowed to react in the microwave for 2 hours at an internal pressure of 46 bar, corresponding to a temperature of 240°C. After cooling down radiatively, the obtained white-gray powders were separated by centrifugation (9000 rpm) and washed several times with water and ethanol. Finally, the powder was dried at 75°C overnight.

5.3.3 Materials Characterization

X-ray diffraction

X-ray diffraction (XRD) patterns were recorded using a Siemens D5000 instrument with CuKα_1 radiation (Ge(220) monochromator) and a Braun M50 position sensitive detector in transmission geometry. Samples were prepared between two "Scotch Magic" films. Phase analyses were performed according to the PDF-2 database (PDF-2, Release 2004, JCPDS - International Centre for diffraction Data (2004)) using EVA 10.0 [30]. Anisotropic peak broadening due to anisotropic crystallite shape was modeled within the fundamental parameter approach [31, 32] determining individual crystallite sizes CS_{hkl} for any reflection (hkl) according to the quadratic form:

[1] Due to the lower concentration, 6.25 ml of TMAH solution were used. The other amounts were adjusted accordingly to reach the same total volume of 19.5 ml

$$CS_{hkl} = 1/norm. \cdot (\underline{h^T} \cdot \underline{C} \cdot \underline{h}) \tag{5.1}$$

with $\underline{h}$ = (hkl) and $\underline{C_{ij}} = (a_i)^{1/2} \cdot (a_j)^{1/2}$ being the second rank symmetric tensor of the square roots of the crystallite dimensions in directions i and j, respectively [33].

Electron Microscopy

The products were characterized by means of transmission electron microscopy (TEM) using a Philips 420 instrument with an acceleration voltage of 120 kV. Samples for TEM measurements were prepared from ethanolic suspensions of the samples. A few drops of the ultrasonicated suspension were administered onto a Cu grid coated with an amorphous carbon layer. Scanning electron microscopy was performed using a FEI Nova nanoSEM under high vacuum mode.

Film Thickness Measurements

The film thickness on the FTO substrate was measured using a Keyence VK-8710 laser microscope and a surface profiler (alpha-step IQ, TENCOR). Surface morphology was checked by optical microscopy (OM).

Dye-Loading Amount

To determine the amount of dye adsorbed on the photoanode, the N719 dye loaded SnO_2 photoanodes were immersed into 10 mM NaOH for 12 hrs at 30°C. Subsequently, the absorption spectra were measured and the intensity of the most intense band in the region 505-515 nm was compared.

Surface Area

Surface areas of the various SnO_2 morphologies were evaluated from BET analysis using a QuantaChrome Autosorb 6B instrument applying a multipoint BET measurement.

5.3.4 Solar Cell Fabrication

Paste Preparation

100-150 mg of the SnO_2 nanoparticles were dispersed in a mixture of EtOH (0.5 ml) and Triton-X-100 (2 drops). PEG400 (8 drops) was then added and the solution was placed in an ultrasound bath for 1 hour. Subsequently, 2 drop of PEG20k dissolved in water (5.5 g in 10 ml) were added and the mixture was homogenized in a ball-mill for 45 minutes.

Device Fabrication

The photoanodes were deposited using the "doctor-blade" method, applying the prepared semiconductor paste on the FTO substrates (sheet resistance 8 Ω/sq., Pilkington) and sintered at 450°C for 30 minutes.

Subsequently, the electrodes were dipped into a 0.3 mM solution of N719 (cis-bis(isothiocyanato)bis(2,2'-bipyridyl-4,4'-dicarboxylato)-ruthenium(II) bis-tetrabutylammonium, Solaronix) in acetonitrile and tert-butanol (1:1 v/v) for 18 hours at 30°C and then rinsed with acetonitrile and dried with a nitrogen gas flow.

The electrolyte was composed of 0.1 M LiI, 0.6 M MPII, 0.05 M I_2, 0.5 M tBP and 0.05 M GuSCN in acetonitrile. The Pt counter electrode was prepared by thermal decomposition of 0.01 M H_2PtCl_6, spin-coated onto the FTO substrate (heating: 450°C for 30 minutes). Two holes were drilled into the Pt counter electrode for an easy electrolyte injection. Surlyn (25 μm, Solaronix) was used as a spacer between the

photoanode and Pt counter electrode. The Surlyn was attached around the active area and then sealed by heat-pressing at 90°C and a pressure of about $1.8\,\mathrm{kg \cdot cm^{-2}}$. As a last step, the electrolyte was filled in through one of two holes in the Pt counter electrode and finally the holes were sealed with Surlyn film and another cover glass. A scheme is shown in Figure 5.1.

5.3.5 Solar Cell Characterization

The photovoltaic performance of the cells based on SnO_2 nanostructures was characterized by current-voltage (J-V) measurements and incident photon-to-current conversion efficiency (IPCE). Current-voltage characterization of the DSSC was carried out using a Keithley Model 2400 source meter and solar simulator with 300 W Xenon arc-lamp (Newport) under 1 sun illumination (AM 1.5, $100\,\mathrm{mW \cdot cm^{-2}}$). The light intensity was calibrated according to a silicon solar cell (PV measurements, Inc.). For the best cells, a light shading mask was placed on top of the residual area of the front-side FTO substrate to prevent an overestimation of power conversion efficiency. The quantum efficiency of the cells was analyzed by IPCE (incident photon-to-current conversion efficiency, PV measurements, Inc.).

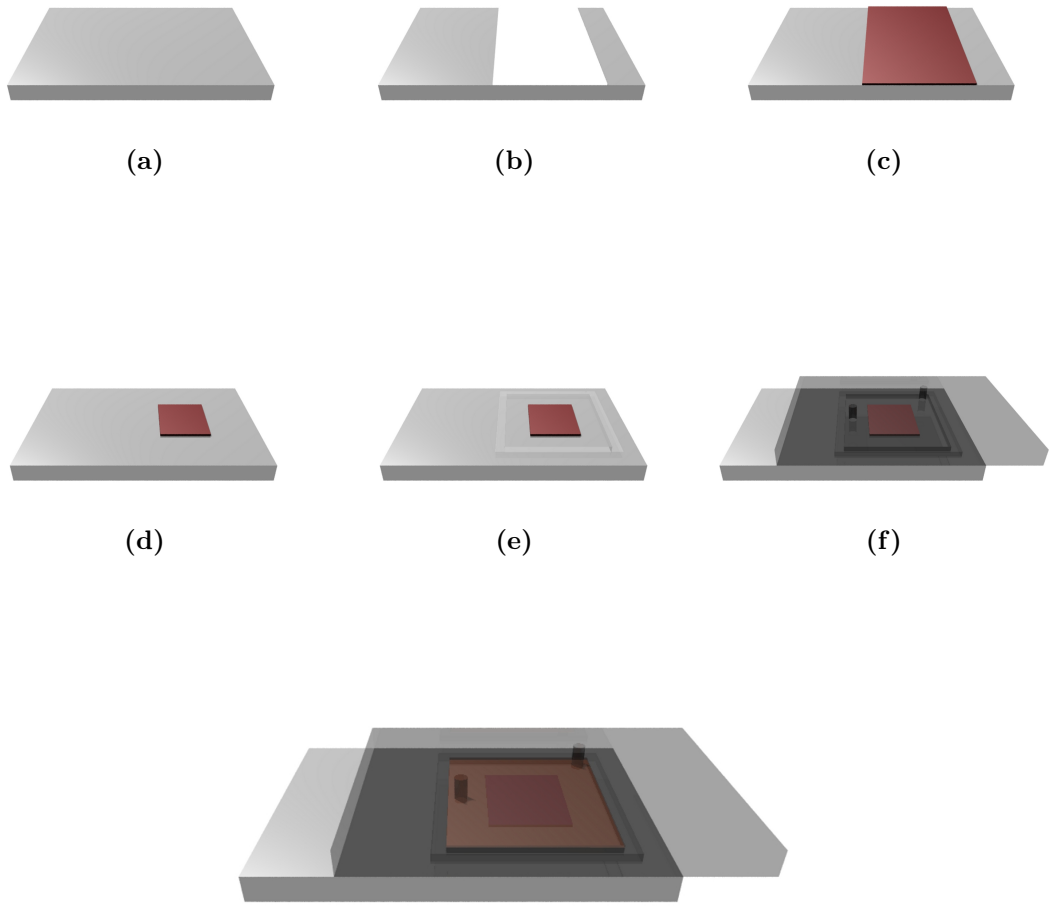

Figure 5.1: Scheme of the various assembly steps of a solar cell: (a) represents the bare FTO substrate; (b) shows the photoanode after the "doctor-blading"; (c) subsequently, the anode is loaded with the dye and cut down to the usual active area of 0.25 cm^2, shown in (d); the Surlyn-spacer is added (e) and the counter electrode is placed on top (f); the electrolyte is added through the two holes in the counter electrode (g). Finally, these holes are sealed with another Surlyn strip and a thin glass disc (not shown).

5.4 Results and Discussion

All the samples were first subject to phase determination by means of X-ray powder diffraction. Figure 5.2 shows that all precursor cations yield phase pure SnO_2 (cassiterite PDF-2, entry (41-1445) space group: $P4_2/mnm$). Full profile pattern fitting was applied to confirm the structural parameters of the samples, as well as to determine the crystallite sizes and to obtain a first hint of the morphological features (such as anisotropy). The results are presented in Table 5.1. The reflection profiles of the sample prepared with NH_4OH are all very broad, indicating the very small crystallite size of the particles. No hint for anisotropy is found since all three refined crystallite sizes are approximately the same, pointing to isotropic particles. A comparison with the values obtained for the three other samples shows that all of them exhibit at least some anisotropy in the [001] direction. Additionally, the reflection profiles are much narrower, indicating a larger crystallite size, see Table 5.1.

Table 5.1: Refined crystallite sizes derived from LeBail fits. The errors correspond to the threefold of the e.s.d. values.

Precursor	**CS_A /nm**	**CS_B /nm**	**CS_C /nm**
NaOH	14.9 ± 0.27	16.5 ± 0.30	34.7 ± 0.57
KOH	25.5 ± 0.69	28.4 ± 0.75	43.7 ± 1.20
TMAH	10.0 ± 0.24	13.2 ± 0.27	27.3 ± 0.54
NH_4OH	8.7 ± 0.12	9.7 ± 0.12	8.7 ± 0.15

To further elucidate the morphology of the obtained nanomaterials, transmission electron microscopy was applied. Figure 5.3 shows the TEM micrographs of the various prepared products, obtained by the use of different precursor bases. Using NaOH, homogeneous bundles of nanorods can be found throughout the sample. Only very few isolated rods are found. If KOH is used as the precursor base, the anisotropic character of the sample decreases, meaning that in addition to smaller rods, spherical

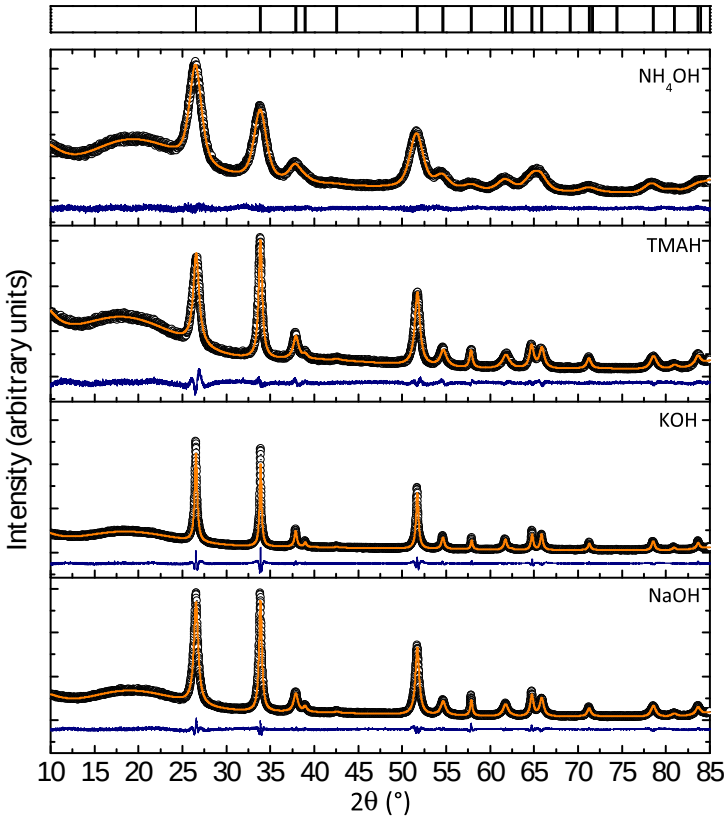

Figure 5.2: X-ray powder diffraction data and full pattern profile fitting of the data obtained from samples employing different morphologies. The bars on top represent the calculated d-values for SnO_2.

particles and larger plates can be found in the sample. TMAH leads also to a mixture of particles, platelets and rod-like structures. The most interesting feature in this sample is the formation of larger platelets consisting of inter-connected smaller particles, see Figure 5.3 (c). As observed in earlier studies [29], if NH_4OH is used as the precursor base in the synthesis of SnO_2 nanomaterials, small, spherical particles (approx. 8 nm in diameter) that are rather monodisperse are obtained. It can be concluded that the trends in morphology that are observed after standard solvothermal reactions are maintained during the microwave synthesis, however in a much shorter reaction time[2].

[2]From now on, the different morphologies and cells using these materials will be referred to as "NaOH", "KOH" cell *etc.*, see Table 5.2

Table 5.2: Summary of the obtained morphologies. Precursor refers to the base that has been used in the microwave-assisted synthesis of SnO_2 nanomaterials.

Precursor	Morphology
NaOH	Bundles of nanorods
KOH	Rods, spheres and plates
TMAH	Spheres, few rods, Platelets
NH_4OH	Spherical particles

The prepared nanoparticles with different morphologies were then tested for their performance as an anodematerial in dye-sensitized solar cells.

As a first step of the fabrication of the device, the prepared semiconductor paste was coated to the glass substrate using the "doctor-blade" method. SEM images were recorded to ensure that all cells exhibit good film quality and to guarantee a high degree of reproducibility. Figure 5.4 shows the top-view scanning electron micrographs of the sintered photoanodes.

All of the films show a reasonable smooth surface and very few cracks or voids. The ball-milling step reduces the amount of larger particle-agglomerates significantly. However, especially the film prepared with nanorod-shaped particles shows some residual agglomerates, due to the fact that the rods grow in an inter-connected fashion (see the TEM images in Figure 5.3 (a)).

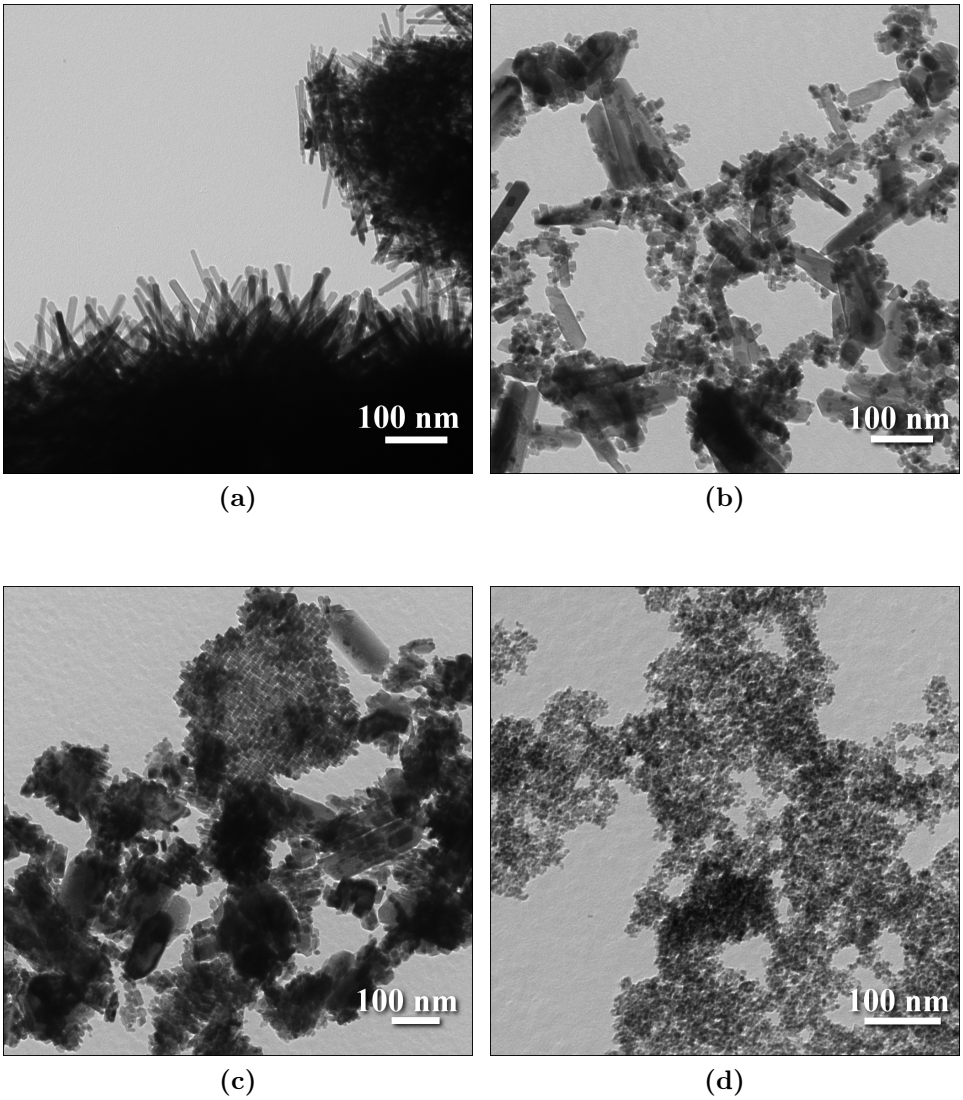

Figure 5.3: TEM micrographs of the as-prepared various morphologies obtained using a microwave-assisted route; (a) shows the nanorods obtained with NaOH and (b) the morphologies prepared with KOH. (c) shows the sample obtained with TMAH; (d) depicts the spheres prepared with NH_4OH.

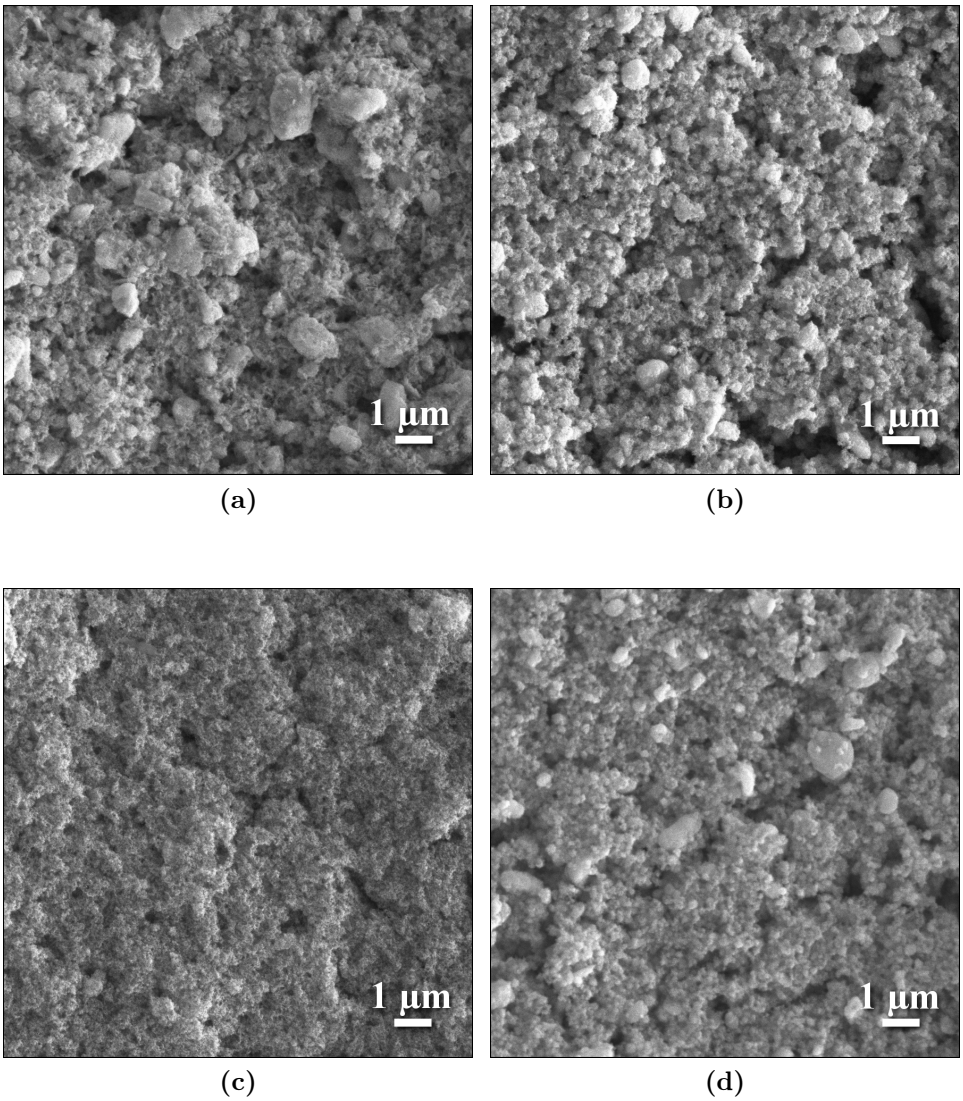

Figure 5.4: Top-view SEM pictures of the prepared photoanodes applying the various morphologies. The used precursor bases have been (a) NaOH, (b) KOH, (c) TMAH and (d) NH_4OH.

Cross-sectional SEM (Figure 5.5) images prove that the films stick nicely to the FTO substrate and do not exhibit larger irregularities. All of the prepared photoanodes show a good film quality and comparable thicknesses, usually in the range of 8-10 μm. Variations in the thickness have been compensated by a sufficient statistic, meaning that even if the film prepared with nanorods was slightly thinner or thicker than the other films, those cells still showed the highest efficiency. The same is true for the other comparisons, see Table 7.1 in the appendix.

To gain a better insight into the factors that influence the photovoltaic performance of the different products, the surface area of the different morphologies and the dye loading amount of the films has been determined, see Table 5.3.

Table 5.3: BET surface area and dye-loading amount of SnO_2 nanoparticles with different morphologies.

Precursor	**BET surface** $/\mathbf{m^2 \cdot g^1}$	**Adsorbed Dye** $/\mathbf{mol \cdot cm^{-3}}$
NaOH	51	$9.1 \cdot 10^{-5}$
KOH	66	$9.0 \cdot 10^{-5}$
TMAH	69	$9.5 \cdot 10^{-5}$
NH_4OH	149	$1.1 \cdot 10^{-4}$

The surface area determined by multipoint BET measurements agrees well with the expected trend: When there are more smaller particles present in the sample, the surface area increases, due to the increase in surface-to-volume ratio. Therefore, according to the BET measurements, the samples that have been prepared with NH_4OH (i.e. the small spheres) possess a surface area that is almost three times as large as those of the nanorod material, that has been prepared using NaOH as the precursor base.

Interestingly, the average amount of dye that is loaded onto the photoanodes employing the different morphologies is almost the same, only a slightly larger amount is found to be adsorbed onto the samples with the highest surface area. That means that despite the larger surface area of the samples consisting of small spherical nano-

particles, there is not significantly more dye adsorbed onto the surface of the anode. The determination of the reason for this behavior (e.g. like surface modification originating from the precursor base) is the topic of ongoing research. It can be noted that all differences in current density are most likely not caused by the amount of adsorbed dye, because this value is the same for all morphologies.

The IPCE (incident photon-to-current conversion efficiency) of the cells are presented in Figure 5.6. The values for samples prepared with NaOH (bundles of nanorods) and KOH (mixture of rods, plates and spheres) show a very high conversion efficiency ($\sim$ 50%) at around 525-530 nm which corresponds to the absorption maximum of the dye. This agrees well with the observed, high J_{sc} values for these samples, see Table 5.4. Cells with anodes employing the "TMAH" sample (mixture of rods, platelets and spheres) and the small spheres (prepared with NH_4OH) exhibit lower values.

Figure 5.7 and Table 5.4 show the current-voltage characteristics of the best set of cells. It should be emphasized again that the observed trend is valid for all cells and is also true for any variations in film thickness or dye-loading amount, meaning that the cells prepared with nanorods always performed the best whereas the cells prepared with small, spherical particles showed always the lowest conversion efficiency.

Table 5.4: I-V data on the measured solar cells. Ref. 1 provides the data obtained from a cell made with a "home-made" TiO_2-paste, Ref. 2 shows the values that are observable with a commercially available paste.

Precursor	**ØThickness /μm**	**V_{oc} /V**	**J_{sc} /mA · cm^{-2}**	**FF**	**Eff. /%**
NaOH	10	0.477	11.58	0.51	2.8
KOH	9	0.365	11.60	0.43	1.8
TMAH	8	0.363	10.00	0.48	1.7
NH_4OH	9	0.338	9.90	0.38	1.3
Ref. 1	15	0.752	9.60	0.69	5.0
Ref. 2	15	0.701	13.30	0.71	7.3

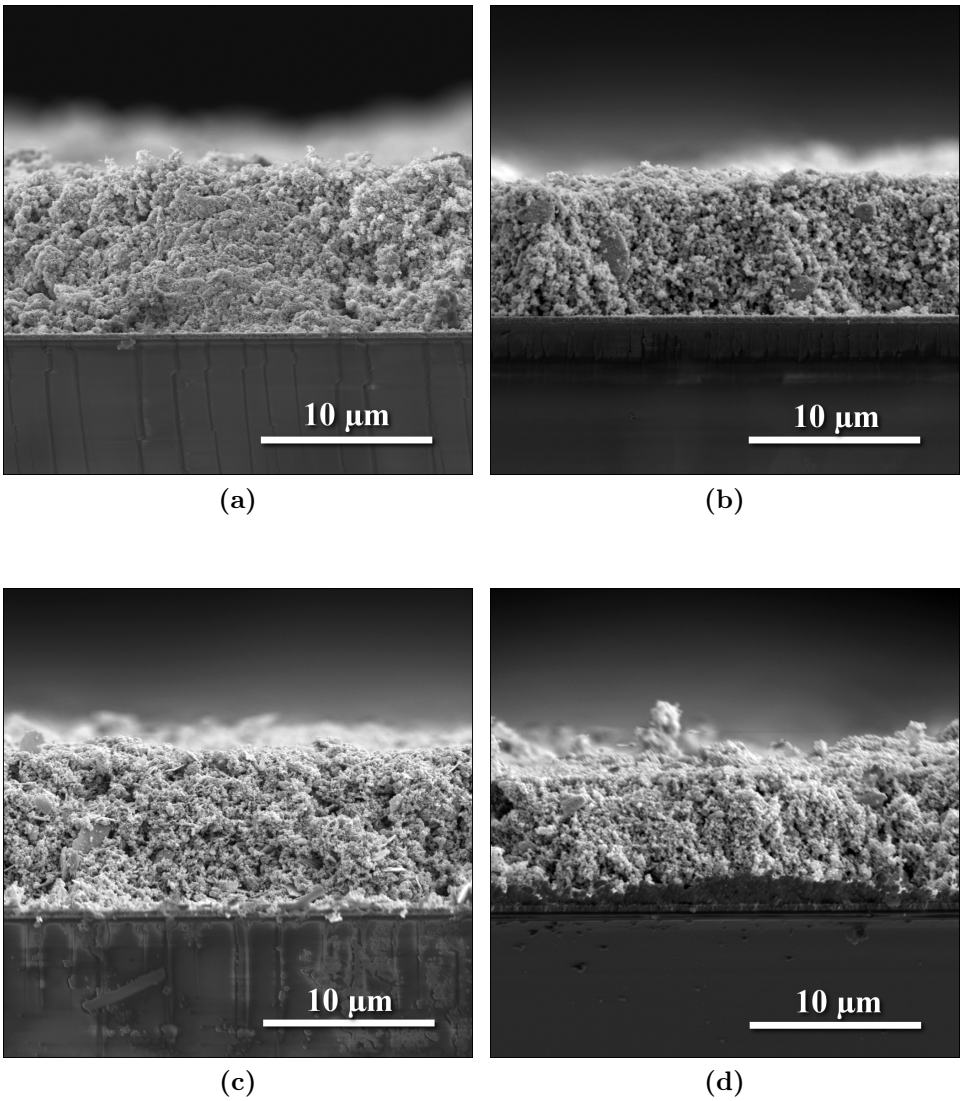

(a) **(b)**

(c) **(d)**

Figure 5.5: Cross-sectional scanning electron microscopy pictures of the prepared photoanodes applying the various morphologies. The used precursor bases have been (a) NaOH, (b) KOH, (c) TMAH and (d) NH_4OH.

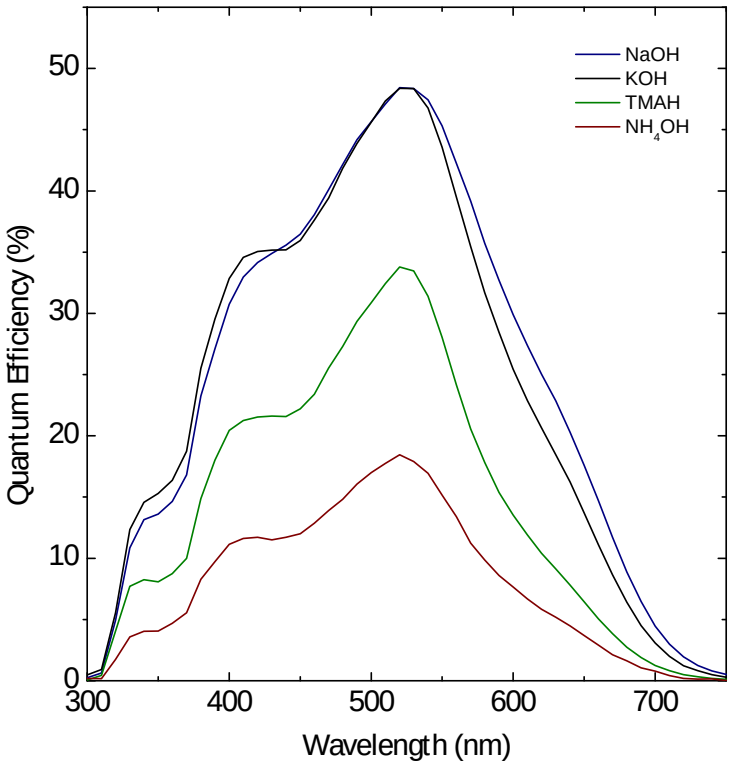

Figure 5.6: IPCE data of the best set of cells.

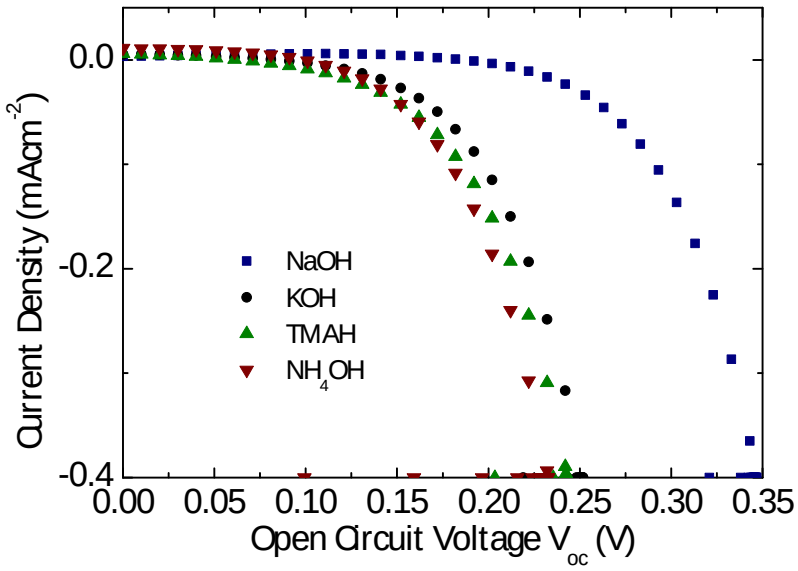

(a)

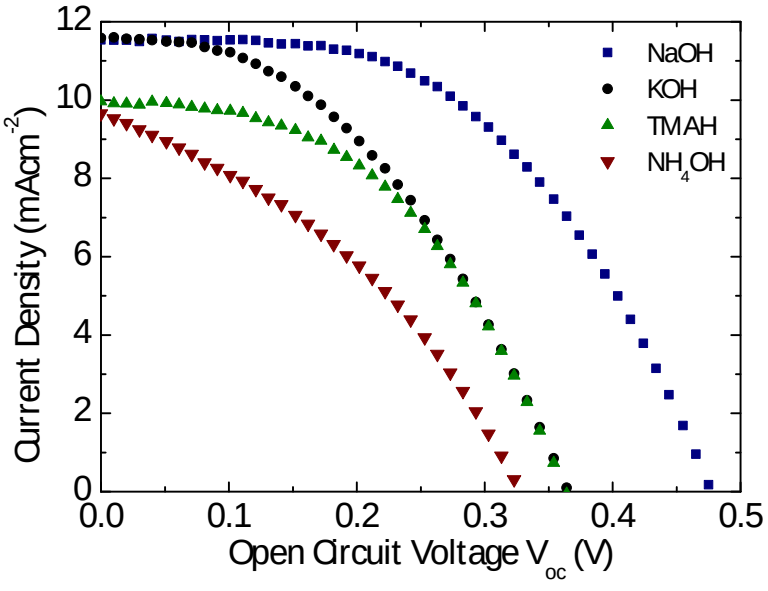

(b)

Figure 5.7: Current-voltage characteristics of the best set of cells. (a) shows the dark current, (b) the behavior under illumination.

The most striking result is the very high V_{oc} that can be observed in the case of the electrode that employs SnO_2 nanorods. The value of 477 mV is very close to the theoretical maximum, if one keeps in mind that V_{oc} is determined by the energy difference between the Fermi level of the semiconductor and the redox-potential of the electrolyte (I_3^-/I^-). The position of the conduction band of SnO_2 has been determined to be approximately 0 - 0.1 V (vs. normal hydrogen electrode, NHE), which means that it is almost 0.5 V lower than that of TiO_2 [25–27]. The redox-potential of the I_3^-/I^- - couple lies in the range between 0.4 - 0.53 V (vs. NHE) [34, 35], meaning that in the case of the electrode that employs the nanorods, almost no recombination losses occur. A further explanation for this behavior is the change in the flat-band potential in anisotropic SnO_2 particles [36].

This is also evident in the dark current measurements; here, the samples that have been prepared with NaOH show a clear shift (almost 150 mV) in the onset of the dark current, see Figure 5.7(a). If the cells are fabricated with anodes consisting of particles that have been prepared with nanoparticles with different morphologies show slightly lower V_{oc} values. They follow basically the trend: the more smaller particles are present, the lower the open-circuit voltage is; thus, a mixture of different morphologies (KOH, TMAH) shows almost the same value, whereas the small spheres show the lowest V_{oc}.

The measured J_{sc} values are in good agreement with the obtained IPCE measurements. Since all of the semiconducting films seemed to adsorb the same amount of dye, despite the difference in morphology and therefore surface area, comparable values would be expected if the electron transport was equally efficient in every sample. However, due to the difference in the IPCE values, a lower current, compared to the other samples, is expected for the "TMAH" and "NH_4OH" cells.

This is exactly what the data show: The samples employing nanorods and a mixture of rods, plates and small spheres (the sample that has been prepared with KOH as the precursor base) show the highest current densities, with values of 11.60 $mA \cdot cm^{-2}$. This rivals almost the current flowing in a sample prepared with a commercially available TiO_2 paste, proving the very efficient electron injection and transport through the photoanode. The current decreases as the amount of isotropic particles increases. This can be attributed to the higher trapping-probability for an electron in a porous network of smaller particles.

The fill factor, which gives an estimation of the parasitic losses within a cell (due to the internal resistances) is above 35% in all cells. Again, the highest value is observed in the "NaOH" devices, whereas the "NH_4OH" cells exhibited the lowest fill factor. The "KOH" and "TMAH" cells show intermediate values. This can be attributed to the fact that in the "NH_4OH" case, higher electron recombination rates and higher internal/interfacial resistances occur. This is surpressed more efficiently in the "NaOH" samples.

Possessing remarkably high V_{oc} and J_{sc} values, an overall efficiency of 2.8% (measured without a shading mask) is achieved in a cell that employs bundles of nanorods as the photoanode. This is among the highest values known for a SnO_2 based cell, in combination with the I_3^-/I^- electrolyte and the N719 dye as the sensitizer. Efficiencies for the cells employing the three other morphologies are all well above 1%, again proving the high qualitiy of the films and devices [16, 36] investigated in this study.

5.5 Conclusion

It could be demonstrated that SnO_2 nanoparticles with various morphologies, prepared using a fast and energy-efficient microwave-assisted reaction pathway, are suitable materials to be used as the photoanode in dye-sensitized solar cells. The products were investigated using X-ray powder diffraction and transmission electron microscopy. As a first step towards the device, an easy and cheap way to fabricate the "semiconducting paste", i.e. the paste that is used to coat the anode onto the conductive glass substrate, was established. This method is only based on cheap and widely available chemicals and does not require extensive materials processing. The films were investigated using scanning electron microscopy to prove the quality of the semiconducting layer. Subsequently, the photoanodes were tested in a dye-sensitized solar cell using the N719 dye and the standard I_3^-/I^- redox couple. Cells employing bundles of nanorods showed the best efficiency values, reaching up to 2.8%. This was attributed to the low rate of recombination losses at the interface and a possible shift in the flat-band potential due to the anisotropic morphology, as well as very efficient electron transport through the network consisting of inter-connected nanorods. A more detailed investigation of the factors that influence the efficiency, as well as to achieve even higher efficiencies, e.g. through surface modifications ("core-shell" anodes) is the topic of ongoing research.

References

[1] B. O'Regan and M. Grätzel. A low-cost, high-efficiency solar cell based on dye-sensitized colloidal TiO_2 films. *Nature*, 353(6346):737–740, 1991.

[2] M. Grätzel. Dye-Sensitized Solar Cells. *Journal of Photochemistry and Photobiology C-Photochemistry Reviews*, 4(2):145–153, 2003.

[3] M. Grätzel. Solar Energy Conversion by Dye-Sensitized Photovoltaic Cells. *Inorganic Chemistry*, 44(20):6841–6851, 2005.

[4] A. N. M. Green, E. Palomares, S. A. Haque, J. M. Kroon, and J. R. Durrant. Charge Transport versus Recombination in Dye-Sensitized Solar Cells Employing Nanocrystalline TiO_2 and SnO_2 Films. *Journal of Physical Chemistry B*, 109(25):12525–12533, 2005.

[5] A. J. Frank, N. Kopidakis, and J. van Lagemaat. Electrons in nanostructured TiO_2 solar cells: transport, recombination and photovoltaic properties: Michael Graetzel Festschrift, a tribute for his 60th Birthday, Dye Sensitized Solar Cells. *Coordination Chemistry Reviews*, 248(13-14):1165–1179, 2004.

[6] A. Hagfeldt, G. Boschloo, L. Sun, L. Kloo, and H. Pettersson. Dye-Sensitized Solar Cells. *Chemical Reviews*, 2010.

[7] M. Grätzel. Photoelectrochemical cells. *Nature*, 414(6861):338–344, 2001.

[8] Y. Ooyama and Y. Harima. Molecular Designs and Syntheses of Organic Dyes for Dye-Sensitized Solar Cells. *European Journal of Organic Chemistry*, 2009(18):2903–2934, 2009.

[9] R. Katoh, A. Furube, T. Yoshihara, K. Hara, G. Fujihashi, S. Takano, S. Murata, H. Arakawa, and M. Tachiya. Efficiencies of electron injection from excited N3 dye into nanocrystalline semiconductor (ZrO_2, TiO_2, ZnO, Nb_2O_5, SnO_2, In_2O_3) films. *Journal of Physical Chemistry B*, 108(15):4818–4822, 2004.

[10] K. Tennakone, G. R. A. Kumara, I. R. M. Kottegoda, and V. P. S. Perera. An efficient dye-sensitized photoelectrochemical solar cell made from oxides of tin and zinc. *Chemical Communications*, (1):15–16, 1999.

[11] M. Law, L. E. Greene, J. C. Johnson, R. Saykally, and P. Yang. Nanowire dye-sensitized solar cells. *Nature Materials*, 4(6):455–459, 2005.

[12] K. Sayama, H. Sugihara, and H. Arakawa. Photoelectrochemical Properties of a Porous Nb_2O_5 Electrode Sensitized by a Ruthenium Dye. *Chemistry of Materials*, 10(12):3825–3832, 1998.

[13] F. Lenzmann, J. Krueger, S. Burnside, K. Brooks, M. Grätzel, D. Gal, S. Rühle, and D. Cahen. Surface Photovoltage Spectroscopy of Dye-Sensitized Solar Cells with TiO_2, Nb_2O_5, and $SrTiO_3$ Nanocrystalline Photoanodes: Indication for Electron Injection from Higher Excited Dye States. *Journal of Physical Chemistry B*, 105(27):6347–6352, 2001.

[14] I. Bedja, S. Hotchandani, and P. V. Kamat. Preparation and Photoelectrochemical Characterization of Thin SnO_2 Nanocrystalline Semiconductor Films and Their Sensitization with Bis(2,2'-bipyridine)(2,2'-bipyridine-4,4'-dicarboxylic acid)ruthenium(II) Complex. *The Journal of Physical Chemistry*, 98(15):4133–4140, 1994.

[15] H. J. Snaith and C. Ducati. SnO_2-Based Dye-Sensitized Hybrid Solar Cells Exhibiting Near Unity Absorbed Photon-to-Electron Conversion Efficiency. *Nano Letters*, 10(4):1259–1265, 2010.

[16] J. Qian, P. Liu, Y. Xiao, Y. Jiang, Y. Cao, X. Ai, and H. Yang. TiO_2-Coated Multilayered SnO_2 Hollow Microspheres for Dye-Sensitized Solar Cells. *Advanced Materials*, 21(36):3663–3667, 2009.

[17] B. Falabretti and J. Robertson. Electronic structures and doping of SnO_2, $CuAlO_2$, and $CuInO_2$. *Journal of Applied Physics*, 102(12):123703–1, 2007.

[18] E.E. Kohnke. Electrical and optical properties of natural stannic oxide crystals. *Journal of Physics and Chemistry of Solids*, 23(11):1557 – 1562, 1962.

[19] C. G. Fonstad and R. H. Rediker. Electrical Properties of High-Quality Stannic Oxide Crystals. *J. Appl. Phys.*, 42(7):2911–2918, 1971.

[20] M. S. Arnold, P. Avouris, Z. W. Pan, and Z. L. Wang. Field-Effect Transistors Based on Single Semiconducting Oxide Nanobelts. *The Journal of Physical Chemistry B*, 107(3):659–663, 2003.

[21] Z. M. Jarzebski and J. P. Marton. Physical Properties of SnO_2 Materials. *Journal of the Electrochemical Society*, 123(9):299C–310C, 1976.

[22] M. K. I. Senevirathna, P. Pitigala, E. V. A. Premalal, K. Tennakone, G. R. A. Kumara, and A. Konno. Stability of the SnO_2/MgO dye-sensitized photo electrochemical solar cell. *Solar Energy Materials and Solar Cells*, 91(6):544–547, 2007.

[23] S. Ferrere, A. Zaban, and B. A. Gregg. Dye sensitization of nanocrystalline tin oxide by perylene derivatives. *Journal of Physical Chemistry B*, 101(23):4490–4493, 1997.

[24] A. Kay and M. Grätzel. Dye-sensitized core-shell nanocrystals: Improved efficiency of mesoporous tin oxide electrodes coated with a thin layer of an insulating oxide. *Chemistry of Materials*, 14(7):2930–2935, 2002.

[25] K. Vinodgopal, Idriss Bedja, and Prashant V. Kamat. Nanostructured Semiconductor Films for Photocatalysis. Photoelectrochemical Behavior of SnO_2/TiO_2 Composite Systems and Its Role in Photocatalytic Degradation of a Textile Azo Dye. *Chemistry of Materials*, 8(8):2180–2187, 1996.

[26] R. W. Fessenden and P. V. Kamat. Rate Constants for Charge Injection from Excited Sensitizer into SnO_2, ZnO, and TiO_2 Semiconductor Nanocrystallites. *The Journal of Physical Chemistry*, 99(34):12902–12906, 1995.

[27] D. E. Scaife. Oxide semiconductors in photoelectrochemical conversion of solar energy. *Solar Energy*, 25(1):41–54, 1980.

[28] J. Liu, T. Luo, S. Mouli T, F. Meng, B. Sun, M. Li, and J. Liu. A novel coral-like porous SnO_2 hollow architecture: biomimetic swallowing growth mechanism and enhanced photovoltaic property for dye-sensitized solar cell application. *Chemical Communications*, 46(3):472–474, 2010.

[29] A. Birkel, N. Loges, E. Mugnaioli, R. Branscheid, D. Koll, S. Frank, M. Panthöfer, and W. Tremel. Interaction of Alkaline Metal Cations with Oxidic Surfaces: Effect on the Morphology of SnO_2 Nanoparticles. *Langmuir*, 26(5):3590–3595, 2010.

[30] EVA 10.0, 2003.

[31] A. Coelho. TOPAS Academic, V.4.1, 2007.

[32] R. W. Cheary and A. Coelho. A fundamental parameters approach to X-ray line-profile fitting. *Journal of Applied Crystallography*, 25(2):109–121, 1992.

[33] M. Panthöfer. in preparation. *Journal of Applied Crystallography*, 2010.

[34] M. Wang, N. Chamberland, L. Breau, J.-E. Moser, R. Humphry-Baker, B. Marsan, S. M. Zakeeruddin, and M. Grätzel. An organic redox electrolyte to rival triiodide/iodide in dye-sensitized solar cells. *Nature Chemistry*, 2(5):385–389, 2010.

[35] A. Kay, R. Humphry-Baker, and Michael Grätzel. Artificial Photosynthesis. 2. Investigations on the Mechanism of Photosensitization of Nanocrystalline TiO_2 Solar Cells by Chlorophyll Derivatives. *The Journal of Physical Chemistry*, 98(3):952–959, 1994.

[36] S. Gubbala, V. Chakrapani, V. Kumar, and M. K. Sunkara. Band-Edge Engineered Hybrid Structures for Dye-Sensitized Solar Cells Based on SnO_2 Nanowires. *Advanced Functional Materials*, 18(16):2411–2418, 2008.

6 Electrochemical Synthesis of Porous SnO_2

6.1 Abstract

The formation of porous tin oxide materials through anodic oxidation has been studied. As a first step, an optimization of the electrolytic polishing of bare tin foil has been established. This was achieved by careful tuning of the reaction parameters from methods known to the literature. In order to form the porous oxidic layer, the polished foil was subject to an electrochemical treatment. X-ray diffraction has been applied to determine the phase composition of the prepared porous structures. Using different electrolyte compositions and through the variation of certain reaction parameters such as the time, voltage, temperature *etc.*, a change in the morphology, i.e. as the pore shape and wall thickness has been observed. This has been investigated by means of laser microscopy and scanning electron microscopy.

6.2 Introduction

The synthesis and characterization of self-ordered materials of so-called valve-metals have attracted a lot of attention over the past years. The most prominent metal among them (i.e. aluminum) has been studied for decades [1–3]. For aluminum, all sorts of different preparation techniques are available and the materials properties, such as the pore diameter, are very well tunable. In addition, in recent years other materials such as titanium [4–6], niobium [7, 8] and zirconium [9, 10] have been found to form ordered structures under the right experimental conditions. This opens whole new fields of applications, since now not only the morphology is tunable, but there are also additional materials, others than aluminum oxide, available. Therefore, the search for ordered arrays of other metal oxides is a very vivid area of science.

Although the use of an anodic oxidation to form porous SnO_2 has been reported before [11], no self-organized ordered structure with a defined pore-size and distribution has been achieved yet. This arrangement is of special importance since it might facilitate many processes on which some of the applications of SnO_2 rely [12, 13]. One-dimensional membranes could be used as electrodes [14] with a clearly defined electron conduction pathway in solar cells. These membranes could also improve the gas sensing abilities of these SnO_2 since they offer a large surface area and a defined flow-direction for the gas molecules [15]. Herein, it was systematically investigated how the variation of different reaction parameters, that are crucial to the growth of porous tin oxide structures influences the obtained morphology. The products were studied using X-ray diffraction and various microscopy techniques. It could be shown that with the careful choice of the electrolyte, a certain amount of morphology control is possible. The search for an ordered array of SnO_2 nanotubes, possibly achievable by carefully tuning the reaction parameters, is the subject of ongoing research.

6.3 Experimental

6.3.1 Materials

All starting materials were used without further purification. Commercially available tin foils with different thicknesses (0.125 mm, 0.25 mm and 0.5 mm) and purity grades (at least 99.9%) were purchased from ABCR. The foil was cut down to a diameter of 20 or 15 mm using a stamping tool. The polishing solution was composed of 1-butanol (99%, Acros Organics), methanol (p.A., Sigma-Aldrich), perchloric acid (70%, Sigma-Aldrich) and Millipore water (18.2 MΩ) [4]. Chemicals used in the electrolyte included oxalic acid (p.A., Merck), sulfuric acid (95-97%, Sigma-Aldrich), phosphoric acid (≥85 wt.%, Merck) and potassium oxalate monohydrate (p.A., Acros). Ethylene glycol (99%, EG) was purchased from ChemPur, diethylene glycol (99%, DEG) and tetraethylene glycol (99%, TEG) were obtained from Sigma-Aldrich. Graphite electrodes with different diameters were supplied by C. Conradty, Nürnberg.

6.3.2 Experimental Setup

The voltage was supplied using a *Voltcraft PSP 1204* power source from Conrad Electronics. Different voltages were used during the reaction, the current was always limited to 750 mA. The reactions were carried out in a homemade electrochemical cell consisting of a massive copper block (diameter 10 cm) with a connector to the external circuit. The foil was placed in the center of the copper block and then covered with a Teflon vessel. This vessel had a circular hole in the bottom part (diameter 20 or 15 mm) and a rubber ring as isolation. Finally, the two parts were connected to prevent leakage of the electrolyte, using six screws. A schematic drawing is presented in Figure 6.1.

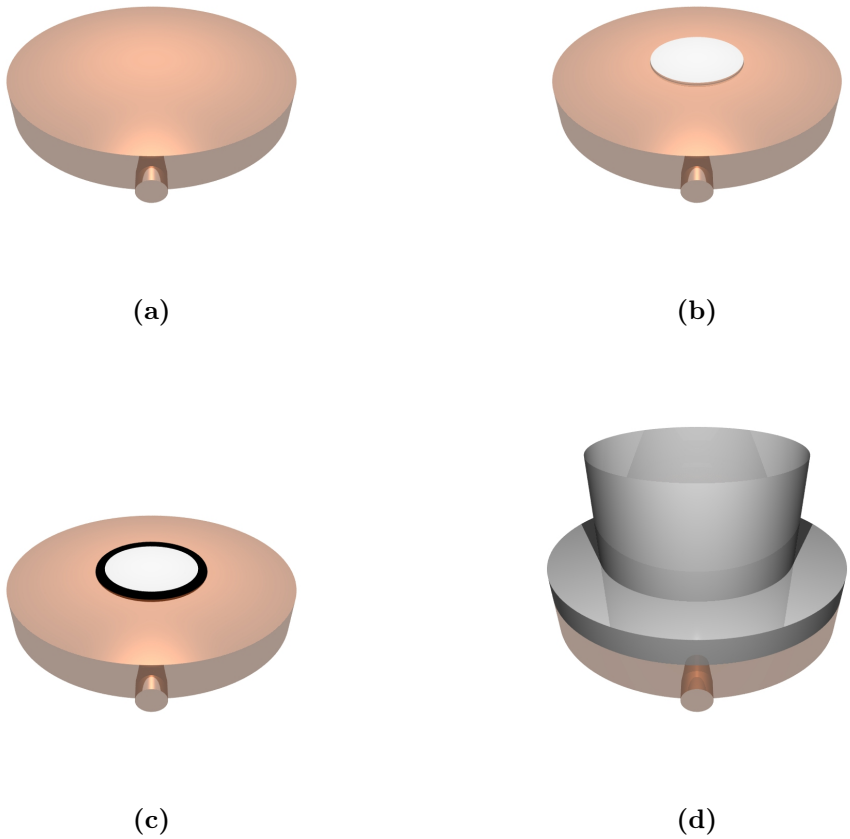

(a) **(b)**

(c) **(d)**

Figure 6.1: Scheme of the experimental setup. (a) shows the bare copper block, (b) the foil placed in the middle, (c) the rubber ring as isolation and (d) the Teflon vessel on top of the metal foil. The screws that are used to connect the copper and Teflon part have been omitted for clarity.

6.3.3 Sample Preparation

Electrolytical polishing was performed modifying a method described earlier [4, 16, 17]. The electrolyte was composed of a mixture of methanol, 1-butanol, $HClO_4$ and water. The solution consisted of 562.5 ml MeOH, 375 ml BuOH, 53.6 ml 70% $HClO_4$ and 8.9 ml of water.

The bare metal foil was treated at a constant voltage between 40 and 50 V at room temperature. 25 - 30 ml of the cold polishing solution were filled into to the experimental setup and the graphite electrode (diameter: 0.5 cm) was positioned at the bottom of the Teflon vessel, slightly off center and thus not overlapping with the tin foil. The polishing was performed in 5-7 steps, lasting usually 20, 12, 8, 4, 2 and finally 5 seconds.

The anodic oxidation was carried out in the same reaction cell, applying different voltages, electrolyte compositions and reaction times. The distance between the anode and cathode was kept at around 2 cm with the graphite cathode being centered above the metal foil.

6.3.4 Characterization

Electron Microscopy

Scanning electron microscopy (SEM) pictures were obtained using high vacuum mode SEM (Nova NanoSEM; FEI Company, Eindhoven, the Netherlands) and a FEI NovaNano FEG-SEM 630. The anodized metal foils were attached to an aluminum stub using an adhesive conductive carbon tape and were additionally contacted on the surface with an adhesive copper band.

Laser Microscopy

Laser microscopic pictures were recorded using a Keyence VK-8710 laser microscope equipped with a movable x-y stage. The surface roughness was calculated according to equation 6.1:

$$R_q = \sqrt{(\frac{1}{N} \cdot \sum (z(x) - < z >)^2)} \tag{6.1}$$

X-ray Powder Diffraction

X-ray diffraction patterns (XRD) were recorded using a Bruker AXS D8 Discover powder diffractometer (CuKα radiation, graphite monochromator) equipped with a 2D HiStar detector. Phase analyses were performed according to the PDF-2 using Bruker AXS EVA 10.0 [18]. Crystallites sizes, intensity alterations due to preferred orientation and anisotropic reflection profile broadening due to anisotropic morphologies were determined by means of LeBail fits [19] and Rietveld refinements [20], respectively, applying the fundamental parameter approach using TOPAS Academic V4.1 [21].

6.4 Results and Discussion

The first step in the fabrication of ordered porous materials is the removal of any surface impurities (chemical as well as morphological); meaning the preparation of a flat and smooth surface. This is usually achieved through an electrolytical polishing procedure during which, through the application of an external voltage, the surface impurities are removed. Figure 6.2 shows a fotographic image of a foil before and after the electrochemical treatment. It is clearly visible that the surface roughness has decreased dramatically. Whereas the untreated foil possesses clear manufacturing signs, such as scratches from the roll-milling process, the polished foil exhibits a more mirror-like finish. This is due to the higher reflectivity of the visible light and is a result of the smoother surface.

(a) **(b)**

Figure 6.2: (a) Tin foil as-purchased from the manufacturer (after cutting to size) (b) tin foil after electropolishing.

A closer look at the surface using laser microscope images confirms this observation, see Figure 6.3. The pristine tin foil shows a lot of rough areas with dents and peaks. The preferential direction of the roll-milling process is observable (scratches that run through the foil). In comparison to that, the polished foil shows a very smooth and homogeneous surface over larger areas.

This is only interrupted at grain boundaries. These borders between neatly polished areas do not vanish, even after multiple repetitions of the polishing steps.

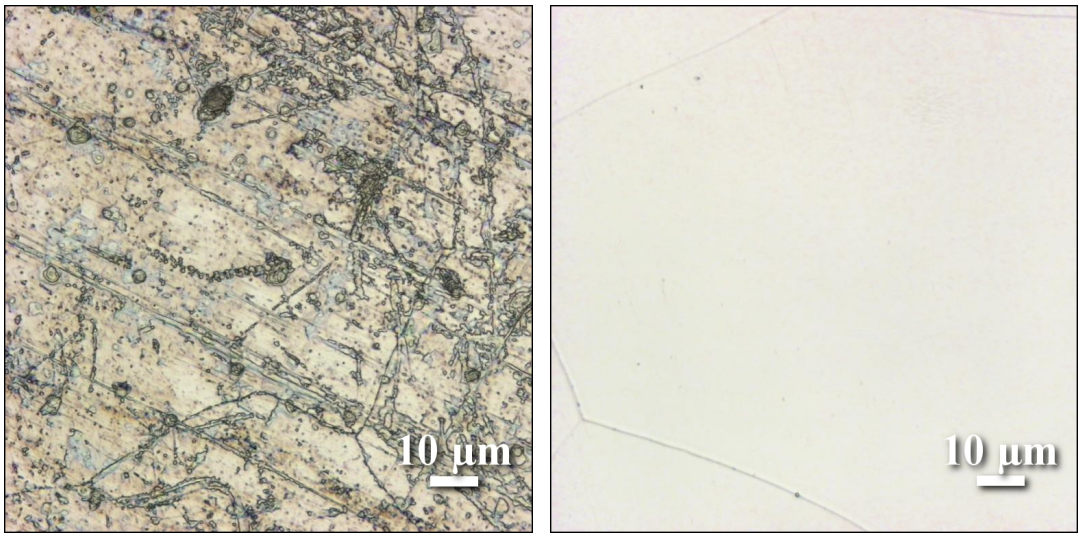

(a) **(b)**

Figure 6.3: An image with 100x magnification showing: (a) Tin foil as-purchased from the manufacturer and (b) tin foil after electropolishing.

The surface of the unpolished foil shows many surface irregularities, like "bumps" and "valleys", some of them reaching peak values of up to 12 μm. This results in a total surface roughness of $R_q = 0.26\,\mu$m. The polishing reduces this value dramatically. As it can be seen in Figure 6.4 (b), the surface is almost perfectly flat. This is true for most areas of the polished sample, only at the aforementioned grain boundaries, minor "valleys" can be found. The average R_q decreases to $0.03\,\mu$m, at some very smooth regions even down to $R_q = 0.01\,\mu$m.

Scanning electron microscope images provide further hints that the surface has been smoothened. A comparison (Figure 6.5) between the micrograph of an unpolished foil with the polished metal clearly shows that after the polishing, no more height irregularities are found over a range of several micrometers. This stands in contrast to the rough surface of the bare tin foil.

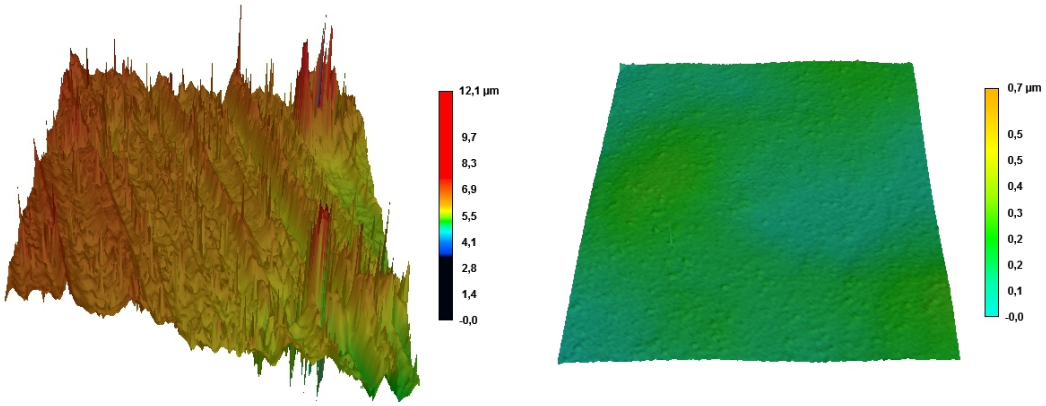

(a) **(b)**

Figure 6.4: Laser-microscopical height-image with 100x magnification showing: (a) Tin foil as it has been purchased from the manufacturer (after cutting to size); (b) Tin foil after electropolishing.

The polished foil was now subject to electrochemical oxidations using various electrolyte compositions, voltages and reaction times, see Tables 6.1, 6.2 and 6.3.

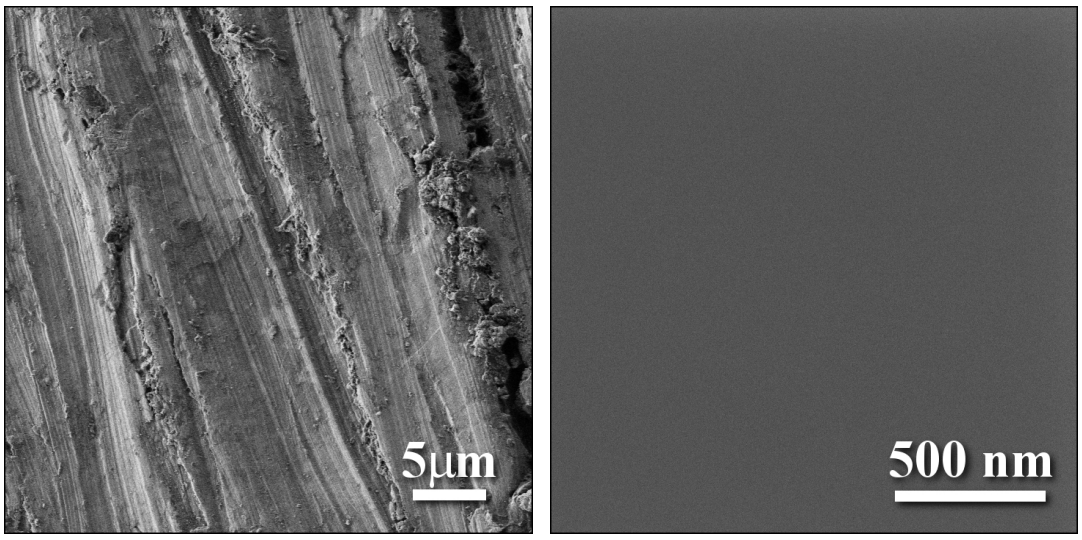

(a) **(b)**

Figure 6.5: SEM micrographs of (a) Tin foil as it has been purchased from the manufacturer; (b) Tin surface after electropolishing.

6.4.1 Electrolytes based on Oxalic Acid

Table 6.1: Anodizations performed with oxalic acid electrolytes.

Solvent	**Conc. /mol · l^{-1}**	**Voltage /V**	**Time /min**
H_2O	0.5	5	5
H_2O	0.5	10	5
H_2O	0.5	10	10
H_2O, EG	0.25	5	5
H_2O, DEG	0.25	5	5
H_2O, DEG	0.25	7.5	5
H_2O, TEG	0.25	5	5

The first set of investigated electrolyte was based on oxalic acid dissolved in different solvents, derived from Ref. [11], see Table 6.1. The acquired data have shown that the formed product on the tin surface is depending on the voltage that is applied to the system as well as the used solvent.

At 5 V, using an aqueous electrolyte and after a reaction time of 5 minutes (a gas evolution was observed during the reaction), "grains" become clearly visible on the surface of the tin foil. On top of these grains, a colorless layer which consists of $Sn(C_2O_4)$ is formed, see the X-ray powder diffraction data in Figure 6.6 (a) and the laser microscopic image in Figure 6.7. Similar observations are made at a reaction time of 10 minutes.

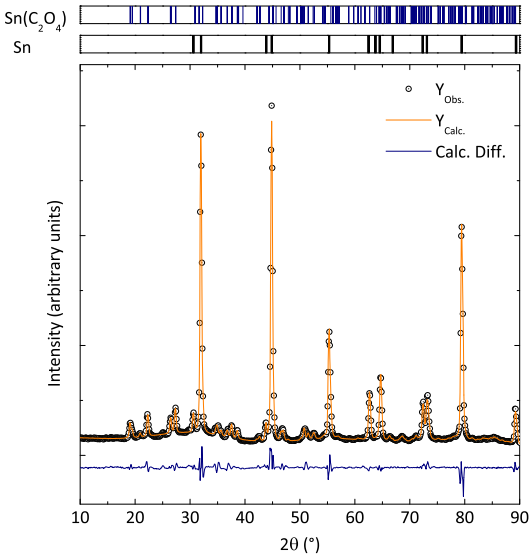

(a)

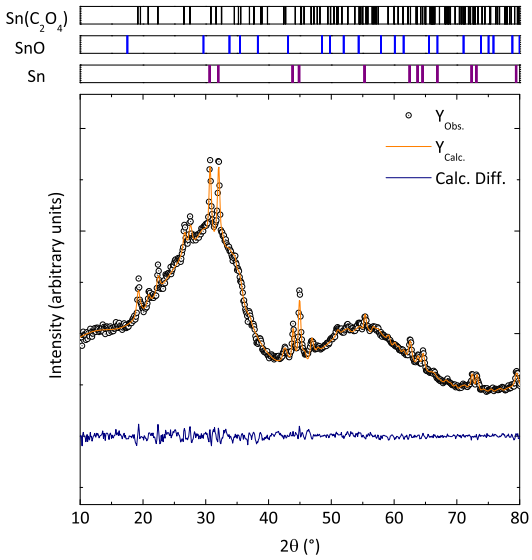

(b)

Figure 6.6: X-ray powder diffraction data and LeBail fitting of the data obtained from (a) a tin oxalate layer on top of the polished tin foil and (b) the brown layer containing the amorphous precursor phase. The bars on top represent the calculated d-values for reflexes of tin, tin oxide and tin oxalate.

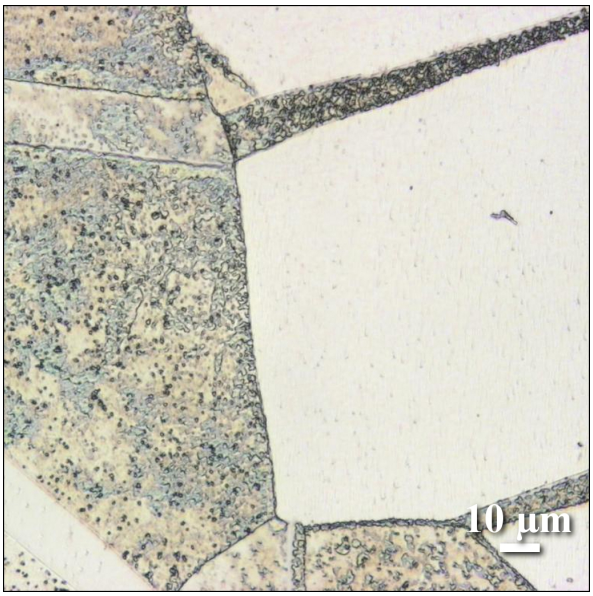

Figure 6.7: Laser microscopic image of a tin foil anodized for 5 minutes. The electrolyte consisted of 0.5 M oxalic acid, dissolved in water.

An increase of the voltage to 10 V, with the reaction time remaining the same, reduces the formation of tin oxalate visible to the eye. On the surface of the tin foil, a black-brown layer is formed. However, some colorless domains are still present. As shown in Figure 6.6 (a), X-ray diffraction data reveal that the colorless parts consist of tin oxalate while the brownish-black film contains an amorphous phase, possibly SnO [11] or tin(II) hydroxide hydrate. The reflections that are attributed to bare tin result from the tin foil underneath the porous layer. SEM micrographs of the film formed with a voltage of 10 V reveal the porous nature of the film. It shows irregularly shaped pores with a diameter in the range of 50-200 nm. No ordering is observed, the pores form a random array, see Figure 6.8.

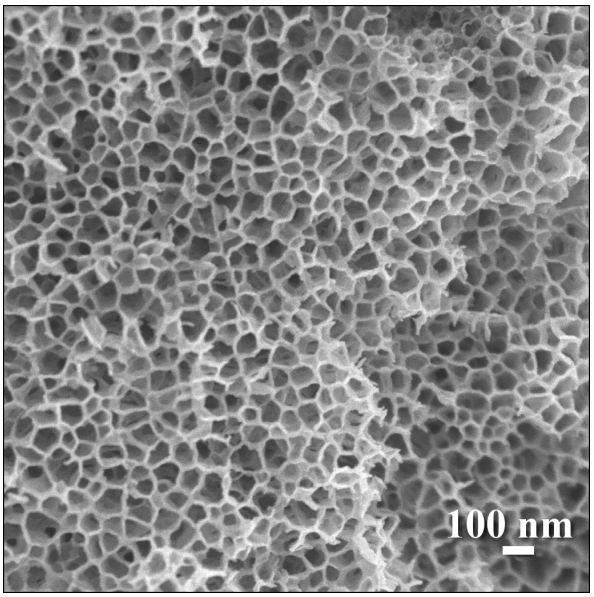

Figure 6.8: SEM micrograph of a film prepared by anodization with an electrolyte consisting of oxalic acid dissolved in H_2O.

The samples prepared with 0.25 M oxalic acid, dissolved in water and ethylene glycol (ratio 1:1 v/v) showed a shimmering greenish-red surface. As it can be seen in the SEM micrograph (Figure 6.9), no ordered porous film was obtained.

The shimmering color of the film is attributed to the formation of a very thin oxidic layer on top of the tin foil that reflects and refracts the light.

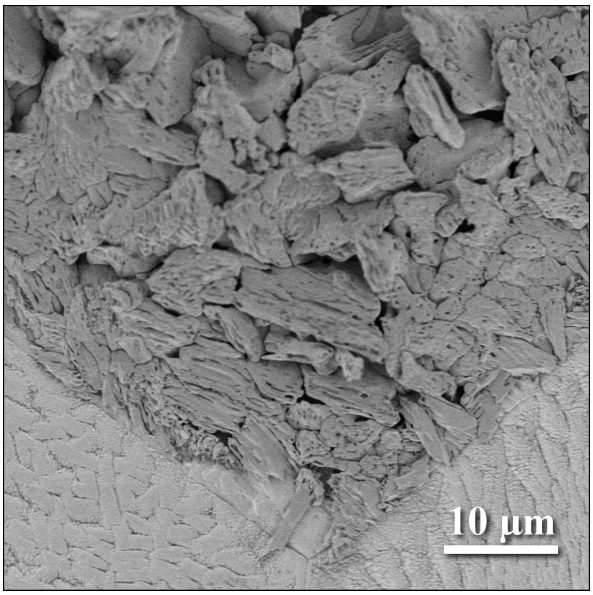

Figure 6.9: SEM micrograph of a film prepared by anodization. The electrolyte consisted of oxalic acid dissolved in water and ethylene glycol.

To increase the viscosity of the electrolyte in order to decrease the gas evolution rate and to reduce the growth speed of the porous film, due to the slower diffusion in a more viscous solvent, ethylene glycol is exchanged with di-ethylene glycol (DEG). One can observe again a shimmering greenish-red film on top of the polished tin foil. The SEM image shows a more regular porous structure, than it has been obtained with ethylene glycol, see 6.10 (a). An increase of the voltage by 50% to 7.5 V does not change the morphology significantly, see 6.10 (b).

If the viscosity is further increased (DEG is exchanged with TEG), a greenish-shiny layer is formed. However, no significant improvement in the surface ordering or porosity can be achieved, see Figure 6.10 (c).

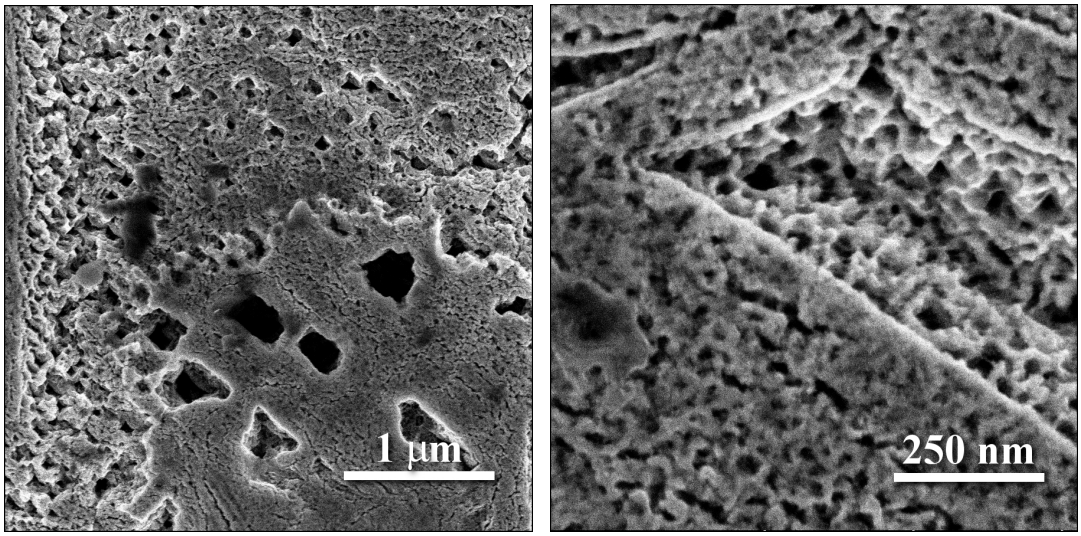

(a) **(b)**

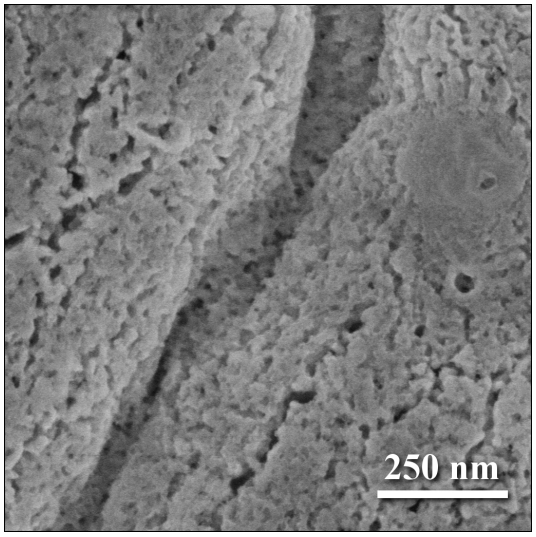

(c)

Figure 6.10: SEM micrograph of a film prepared by anodization. The electrolyte consisted in (a) and (b) of oxalic acid dissolved in water and di-ethylene glycol. In (c) tetraethylene glycol was used instead. The used voltages were 5 V (a), 7.5 V (b) and 5 V (c).

A different approach to control the morphology of the nanoporous structure was to adjust the pH. Therefore, a buffer of oxalic acid, potassium oxalate and water has been used as the electrolyte, see Table 6.2.

Table 6.2: Anodizations performed with oxalic acid buffer solutions.

pH	Ratio Acid/Oxalate	Voltage /V	Time /min
2-3	1	10	5
4-5	0.1	10	5
5-6	0.01	10	5

The data have revealed that a change in the pH does not change the obtained morphology significantly, except it appears that the pores formed at a more acidic pH are etched on the edges. The length-scale of ordering, however is the same in all samples. The SEM micrographs (Figure 6.11) show two porous films prepared with oxalate buffer solutions at different pH - values.

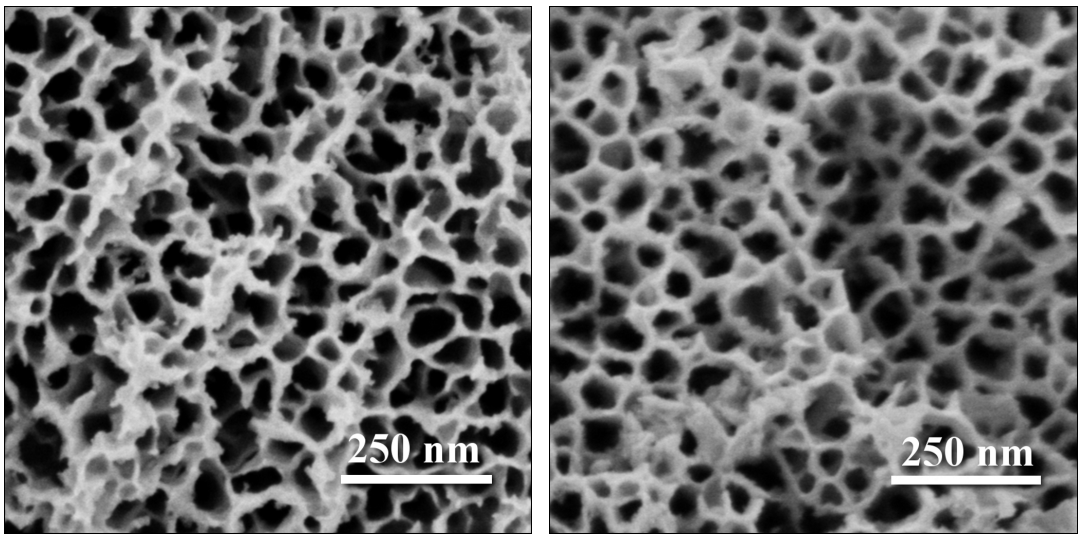

(a) **(b)**

Figure 6.11: SEM pictures of a porous film prepared with an oxalic acid/oxalate buffer. The pH of the reaction mixture was (a) 2-3 and (b) 5-6.

As it has been mentioned in the introduction, many applications in which porous structures are used do not only depend on the morphology, but also on the materials. Therefore, a sintering step after the anodization was performed to transform the as-prepared porous layer (which consists of tin oxalate and an amorphous phase) into SnO_2. This was achieved by a thermal treatment at 350°C for 2 hours. However, problems arise due to the fact that the conversion temperature of the as-prepared materials into SnO_2 lies above the melting point of tin metal (231.93°C).

After the heat-treatment, the color of the porous layer changes from brownish-black to colorless with a shiny-blue layer on top. The heating step has also led to the deformation of the film on top of the tin substrate, causing the porous layer to change its shape. The tin itself has molten and solidified again and therefore lost its circular/flat form as well. This drastic change in shape of both, the film and the supporting tin foil, make further applications more difficult. Still, X-ray powder diffraction data (Figure 6.12) confirm that after 2 hours at 350°C, most of the film has transformed into SnO_2. Still some residual oxalate can be found as well as some reflexes of tin which originate from the foil underneath the porous film. To complete the transition into tin(IV) oxide, a longer heating time and higher temperatures would be necessary.

SEM micrographs show that despite the detachment of the film from the supporting tin foil, the film retains its porous morphology, see Figure 6.13. Some modulations are visible that might be due to the melting of the supporting tin foil.

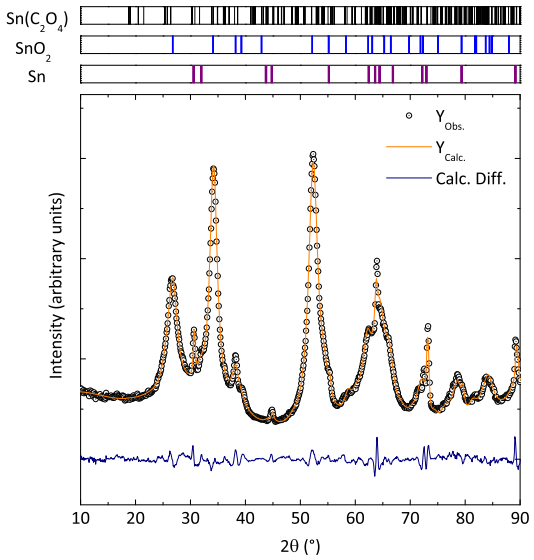

Figure 6.12: X-ray powder diffraction data and LeBail fit of the data obtained from a heated film.

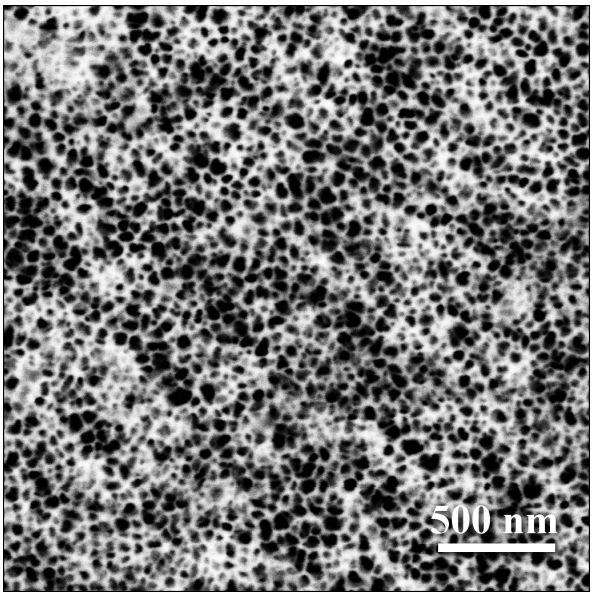

Figure 6.13: SEM image of the surface of a sintered film, prepared with an oxalic acid based electrolyte.

The use of electrolytes containing oxalic acid has led to the formation of crystalline tin oxalate as an undesired side-product during the reaction. To avoid this, alternative electrolytes based on other acids have been investigated.

6.4.2 Electrolytes based on other Acids

Table 6.3: Anodizations performed with other electrolytes.

Electrolyte	**Conc. /mol · l^{-1}**	**Voltage /V**	**Time /min**
H_3PO_4 in EG	0.25	10	60
H_3PO_4 in TEG	0.25	10	60
H_2SO_4 in EG	0.25	10	60
H_2SO_4 in EG	0.05	10	1500

Electrolytes that are based on other acids such as phosphoric acid and sulfuric acid were used to grow the porous films. Sulfuric acid electrolytes usually have led to the anodic destruction of the film, if the concentration is too high, e.g. 0.25 M. For lower concentrations (0.05 M), even at prolonged reaction times, no porous surface layer could be observed.

Phosphoric acid based solutions, on the other hand, did lead to the formation of a shiny, brownish-green film on top of the tin foil. X-ray diffraction data (Figure 6.14) show that, in addition to the reflections originating from the tin foil, there is an amorphous phase formed (the LeBail fit was carried out using the structural model of SnO). SEM investigations revealed that the majority of the surface is covered with a solid layer, see Figure 6.15 (a). Only in voids, where the surface layer has "cracked" open, a structure similar to those obtained with oxalic acid based electrolytes can be found. However, the pores seem to possess thicker pore walls and their shape is more spherical than in samples prepared with oxalic acid, see Figure 6.15 (b). The pore diameter observed in these samples is comparable to the diameter in the samples anodized with oxalic acid. In both cases the diameter lies in the range of 50 - 200 nm.

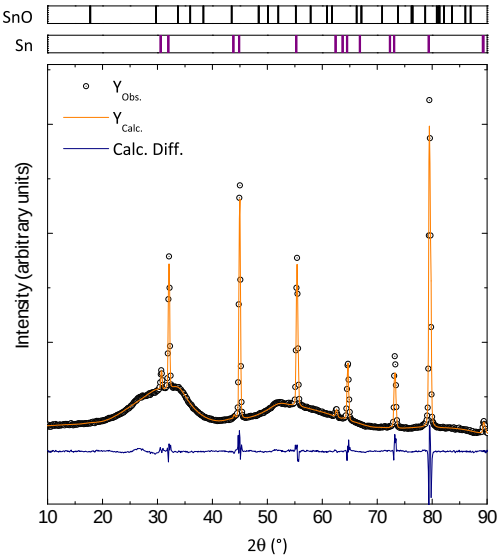

Figure 6.14: X-ray powder diffraction data and LeBail fit of the data obtained from film prepared with a phosphoric acid electrolyte. The bars on top represent the calculated 2θ-values for reflections of tin and tin oxide.

A heat treatment of 450°C for 2 hours has again led to melting of the tin foil and a subsequent detachment and deformation of the (now colorless) film. The film has become very fragile, however the original features (the continuous film with porous "islands") remains. Cracks originating from the detachment process are also clearly visible, see Figure 6.16.

In order to use the advantages of both, oxalic acid and phosphoric acid (i.e. a large area of porous structures with a more defined, round shape), the combination of different acidic electrolytes was investigated. A mixture of 0.5 M oxalic acid in water and 0.75 M H_3PO_4 in ethylene glycol yielded the best results. A brown layer is formed on top of the polished tin foil after an anodization at 10 V for 60 minutes. No shininess has been observed this time, pointing towards the fact that there is no continuous layer on top.

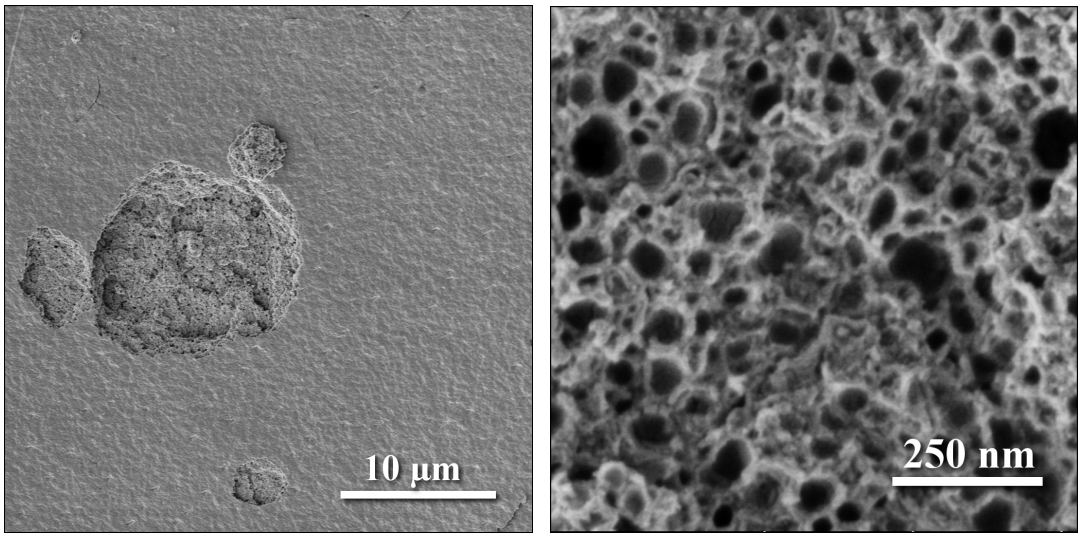

(a) **(b)**

Figure 6.15: SEM picture of a porous film prepared with a H_3PO_4-based electrolyte. (b) shows a magnified image of the porous void in (a).

The pore size and shape resembles the samples prepared only with phosphoric acid. However, as shown in Figure 6.17, no increase in ordering or homogeneity of the pores can be obtained. Due to the very small amount of sample, no X-ray data could be recorded.

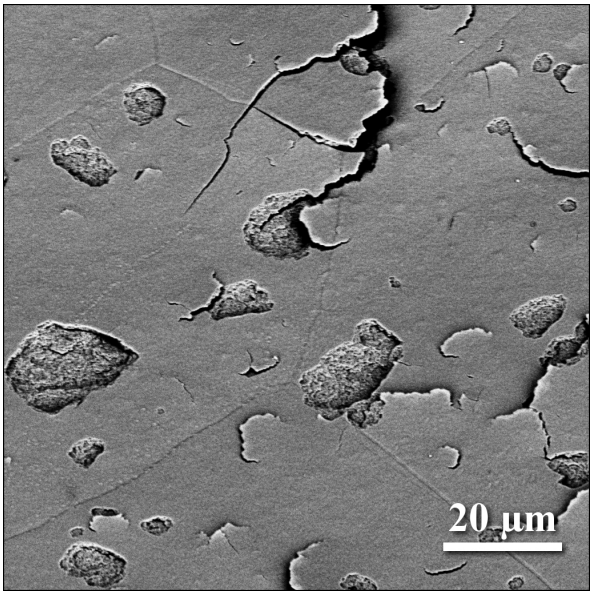

Figure 6.16: SEM pictures of a porous film prepared with a H_3PO_4-based electrolyte, after the sintering step. The sintering was performed at 450°C for 2 hours.

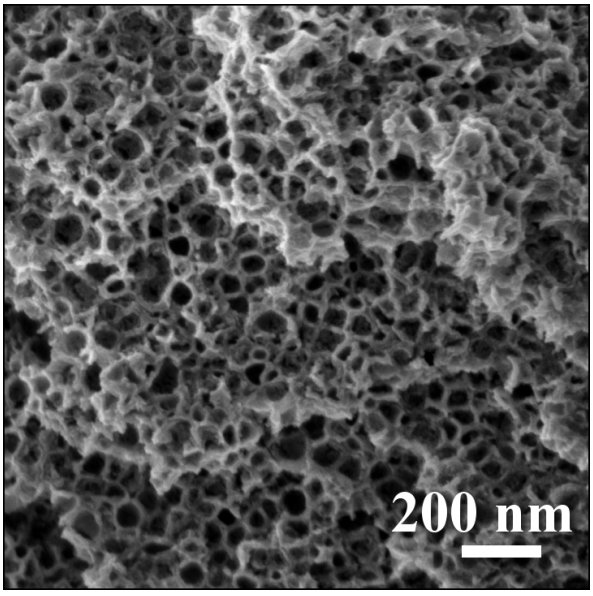

Figure 6.17: SEM picture of a porous film prepared with a mixed acidic electrolyte.

6.5 Conclusion

An easy and fast electropolishing procedure for commercially available tin foils has been established. Making use of an electrolyte based on alcohols and perchloric acid, a short, multistep polishing procedure has led to very smooth and clean surfaces. The second achievement was the successful preparation of porous structures on top of the polished tin foil. Scanning electron microscopy has revealed that electrolytes based on oxalic acid and phosphoric acid (or a combination of both) lead to the formation of a porous film. Using X-ray powder diffraction data, it could be shown that in the first step of the anodization, in oxalic acid electrolytes, a mixture of tin(II) oxalate and an amorphous precursor phase forms. The formation of the oxalate has not been observed in earlier studies in the literature. These phases can be transformed into SnO_2 by a subsequent heating step. The morphology is maintained during this step. However, due to the low melting point of metallic tin, this treatment deforms the as-prepared foils and leads to the detachment of the porous layer. The careful optimization of the reaction parameters to eventually obtain an array of ordered nanopores is the topic of ongoing research.

References

[1] F. Keller, M. S. Hunter, and D. L. Robinson. Structural Features of Oxide Coatings on Aluminum. *Journal of The Electrochemical Society*, 100(9):411–419, 1953.

[2] H. Masuda and K. Fukuda. Ordered Metal Nanohole Arrays Made by a Two-Step Replication of Honeycomb Structures of Anodic Alumina. *Science*, 268(5216):1466–1468, 1995.

[3] H. Masuda, F. Hasegwa, and S. Ono. Self-Ordering of Cell Arrangement of Anodic Porous Alumina Formed in Sulfuric Acid Solution. *Journal of The Electrochemical Society*, 144(5):L127–L130, 1997.

[4] Y. Shin and S. Lee. Self-Organized Regular Arrays of Anodic TiO_2 Nanotubes. *Nano Letters*, 8(10):3171–3173, 2008.

[5] A. Benoit, I. Paramasivam, Y. C Nah, P. Roy, and P. Schmuki. Decoration of TiO_2 nanotube layers with WO_3 nanocrystals for high-electrochromic activity. *Electrochemistry Communications*, 11(4):728–732, 2009.

[6] J. M. Macák, H. Tsuchiya, and P. Schmuki. High-Aspect-Ratio TiO_2 Nan-

otubes by Anodization of Titanium. *Angewandte Chemie International Edition*, 44(14):2100–2102, 2005.

[7] I. Sieber, H. Hildebrand, A. Friedrich, and P. Schmuki. Formation of self-organized niobium porous oxide on niobium. *Electrochemistry Communications*, 7(1):97–100, 2005.

[8] J. Choi, J. H. Lim, S. C. Lee, J. H. Chang, K. J. Kim, and M. A. Cho. Porous niobium oxide films prepared by anodization in HF/H_3PO_4. *Electrochimica Acta*, 51(25):5502–5507, 2006.

[9] Y. Shin and S. Lee. A freestanding membrane of highly ordered anodic ZrO_2 nanotube arrays. *Nanotechnology*, 20(10):105301, 2009.

[10] L. Guo, J. Zhao, X. Wang, R. Xu, and Y. Li. Synthesis and growth mechanism of Zirconia nanotubes by anodization in electrolyte containing Cl^-. *Journal of Solid State Electrochemistry*, 13:1321–1326, 2009.

[11] H.-C. Shin, M. Liu, and J. Dong. Porous Tin Oxides Prepared Using an Anodic Oxidation Process. *Advanced Materials*, 16(3):237–240, 2004.

[12] N. Barsan, M. Schweizer-Berberich, and W. Göpel. Fundamental and practical aspects in the design of nanoscaled SnO_2 gas sensors: a status report. *Fresenius' Journal of Analytical Chemistry*, 365(4):287–304, 1999.

[13] P. G. Harrison and M. J. Willett. The Mechanism of Operation of Tin(IV) Oxide Carbon-Monoxide Sensors. *Nature*, 332(6162):337–339, 1988.

[14] J. R. Jennings, A. Ghicov, L. M. Peter, P. Schmuki, and A. B. Walker. Dye-Sensitized Solar Cells Based on Oriented TiO_2 Nanotube Arrays: Transport, Trapping, and Transfer of Electrons. *Journal of the American Chemical Society*, 2008.

[15] Y. J. Chen, X. Y. Xue, Y. G. Wang, and T. H. Wang. Synthesis and ethanol sensing characteristics of single crystalline SnO_2 nanorods. *Applied Physics Letters*, 87(23):3, 2005.

[16] I. Epelboin. Über den Mechanismus des Elektropolierens. *Zeitschrift für Elektrochemie*, 62(6-7):813–818, 1958.

[17] A. W. Moulen. The Electrolytic Polishing of Lead-Tin Alloys for Microscopic Examination. *Journal of the Electrochemical Society*, 99(6):133–136, 1952.

[18] EVA 10.0, 2003.

[19] A. LeBail, H. Duroy, and J. L. Fourquet. Ab-initio structure determination of $LiSbWO_6$ by X-ray powder diffraction. *Materials Research Bulletin*, 23(3):447–452, 1988.

[20] H. Rietveld. A profile refinement method for nuclear and magnetic structures. *Journal of Applied Crystallography*, 2(2):65–71, 1969.

[21] A. Coelho. TOPAS Academic, V.4.1, 2007.

7 Summary and Outlook

The aim of the work presented in this thesis was to gain insight into the growth process of SnO_2 nanomaterials. This knowledge should then be used to control the synthesis of these materials.

In **chapter 2**, it was demonstrated that the morphology of SnO_2 nanostructures which can be obtained in a simple, template-free solvothermal synthesis is strongly depending on the used precursor (base)cation. Among the alkaline metals, only the Na^+ cation is capable of promoting the growth of highly anisotropic particles at elevated temperatures. The higher homologes, such as potassium, rubidium and cesium (and also TMAH) lead to ill-defined particle mixtures, particularly at temperatures around 200°C. If ammonia is used as the precursor base, one can observe nearly monodisperse, spherical particles. This trend is also valid at temperatures near 250°C. Although in this case the cations K^+ and Rb^+ are capable of promoting one-dimensional growth (due to more suitable crystallization conditions), yet still only Na^+ yields well-defined nanorods. This correlation between the cation and the morphology was attributed to the decreasing adsorption-energy (E_{Ad}) and -probabilities of the base cations on the 110 surface of SnO_2, which is the most stable and therefore exposed surface of SnO_2.

The main interaction energy between the oxide surfaces and the adsorbed cations is the Coulomb interaction. This interaction is mainly determined by the charge-to-radius-ratio of the adsorbed ions and therefore explicable in terms of the Pearson concept of hard and soft acids and bases (HSAB).

Chapter 3 explored how a simple one-step reaction pathway can be used to prepare SnO_2 - $Na_2Sn(OH)_6$ "core-shell" nanorods. X-ray powder diffraction points towards the fact that two different phases, SnO_2 and $Na_2Sn(OH)_6$, are present. The obtained TEM micrographs confirm that a core-shell structure has formed, which can be confirmed by (HR)-transmission electron microscopy images. An EDX (energy dispersive X-ray spectroscopy) line-scan across one core-shell nanorod reveals the fact that the shell material seems to be amorphous, however it contains a higher amount of oxygen and sodium than the core, which consists of SnO_2. Due to this obvious contradiction in the observed data, a more detailed study is necessary.

Having demonstrated that the precursor cations influence the reaction and are not merely spectator ions, **chapter 4** deals with the question of how the morphological growth of SnO_2 nanorods takes place. Therefore, a fast microwave-assisted reaction technique was used. This reaction method made it possible to "quench" the different stages that occur during the growth of one-dimensional nanomaterials. A time-dependent study has revealed that these nanorods start growing from crystalline, yet ill-defined anisotropic (rod-like) structures. These structures then grow further by Ostwald ripening until the final morphology is reached after a reaction time of 45-60 minutes. Initially, this process is supported by an amorphous SnO_2-precursor reservoir and the growth of the nanocrystals proceeds fast. Once this reservoir of reactive material is emptied, crystal growth proceeds more slowly since a re-dissolution and re-crystallization process of the crystals is required. The optical properties of the products were also investigated using infrared and Raman spectroscopy.

It was demonstrated that the IR and Raman behavior is closely related to the evolution of the growth process, i.e. with increasing reaction time the anisotropy increases until after 60 min the crystallization is complete.

Chapter 5 describes how various SnO_2 nanostructures performed as anode material in dye-sensitized solar cells. Combining the knowledge obtained in the previous chapters, a fast and energy-efficient microwave synthesis was used to prepare SnO_2 nanomaterials. Morphology control was achieved using different precursor cations (Na^+, K^+, TMAH and NH_4^+). To use these materials in a solar cell device, an easy way to prepare a semiconductor paste (which is used to prepare the photoanode employing the so-called "doctor-blading" technique) has been established. The preparation is based on a mixture of water, ethanol, PEG 400 and PEG 20000. All manufactured films showed a very good quality and sufficient dye-loading. Interestingly, the amount of dye that has been loaded onto the samples is almost the same for all morphologies, despite the fact that their surface areas differ significantly. The solar cell devices have achieved efficiencies of up to 2.8% which is remarkably high for a nanostructured SnO_2 photoanode. Among all morphologies investigated, the cells that employ nanorods have been the most efficient ones. This was attributed to the fact that the connection between the particles, i.e. nanorods in this particular case, is very suitable for a fast electron transfer towards the electrode, as a result of the decrease in grain-boundaries and defined electron conduction pathways in such one-dimensional systems.

The focus from the preparation of rod-like particles and their application in solar cells was then shifted towards a different approach to obtain nanostructured SnO_2. This is presented in **chapter 6**. As a first step, an electropolishing step for commercially available tin foil has been established. This is used to smoothen the surface for the subsequent anodization step and to get rid of possible surface impurities. The polishing was achieved by employing a multistep electrochemical treatment.

These very flat surfaces were subject to anodizations using various electrolytes, voltages and reaction times. The use of oxalic acid as well as potassium oxalate in different solvents such as water and ethylene glycol at low voltages and short reaction times has led to the formation of nanoporous films with irregular formed pores with varying diameters. If phosphoric acid was used on similar conditions, a porous structure with thicker pore-walls was observed. However, up to date, no ordered array of well-defined nanopores or -tubes has been found. Therefore, an optimization of the reaction parameters is the crucial next step in the future development of this type of reaction.

It can be concluded that the work presented in this thesis improved the insight into the growth processes of (1D)-nanostructures and the parameters that influence this reaction. This knowledge is fundamental to the preparation of SnO_2 nanomaterials with different morphologies. These materials have proven themselves as suitable anode materials to be used in dye-sensitized solar cells, reaching efficiencies of up to 2.8%.

Future work in this particular field of science includes further investigations of the performance of SnO_2 nanostructures in other parts of a dye-sensitized solar cell, i.e. a potential additive to the electrolyte. Then, a more careful examination of the factors that have led to the formation of SnO_2 - $Na_2Sn(OH)_6$ "core-shell" materials is needed because these compounds could also offer an alternative to be used as anode materials in dye-sensitized solar cells.

Appendix

Table 7.1: I-V data of the measured solar cells

Sample	**Area** (cm^{-2})	$\mathbf{V}_{oc}$ (V)	$\mathbf{J}_{sc}$ ($mA \cdot cm^{-2}$)	**FF**	**Eff.** (%)
abP060Na	0.250	0.448	10.60	0.44	2.1
abP060K	0.249	0.439	8.80	0.45	1.8
abP060TMAH	0.248	0.424	8.80	0.45	1.7
abP060NH$_3$	0.246	0.386	10.00	0.40	1.5
abP065Na	0.253	0.448	11.30	0.43	2.2
abP065K	0.249	0.395	11.50	0.40	1.8
abP065TMAH	0.250	0.417	8.40	0.49	1.7
abP065NH$_3$	0.250	0.376	8.70	0.37	1.2
abP070Na	0.258	0.477	11.58	0.51	2.8
abP070-2Na	0.260	0.417	11.80	0.46	2.3
abP070K	0.254	0.365	11.60	0.43	1.8
abP070-2K	0.256	0.394	12.60	0.46	2.3
abP070TMAH	0.255	0.363	10.00	0.48	1.7
abP070-2TMAH	0.257	0.358	9.80	0.47	1.6
abP070NH$_3$	0.258	0.338	9.90	0.38	1.3
abP070-2NH$_3$	0.258	0.346	9.80	0.39	1.3

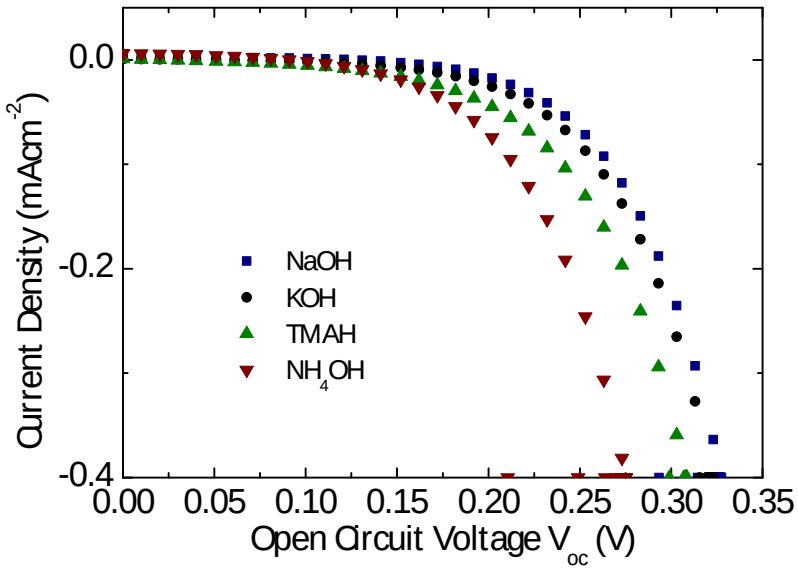

(a)

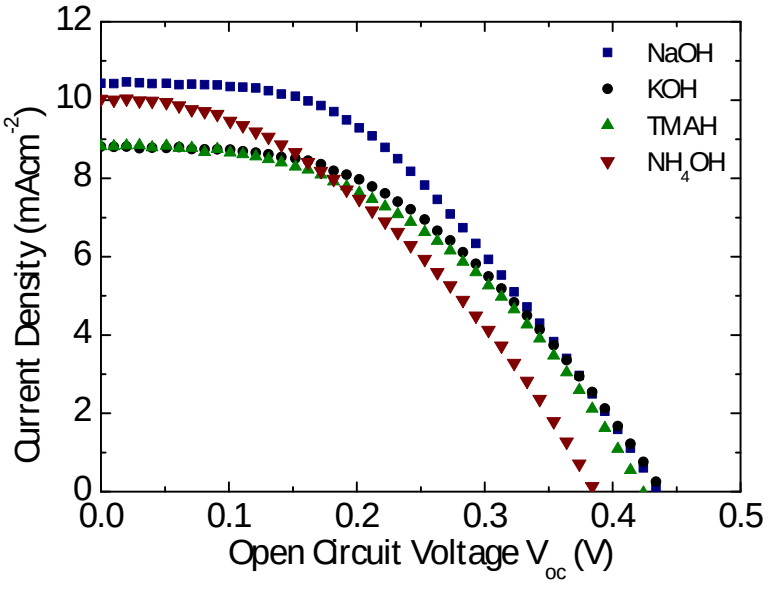

(b)

Figure 7.1: Current-voltage characteristics of abP060. (a) shows the dark current, (b) the behavior under illumination.

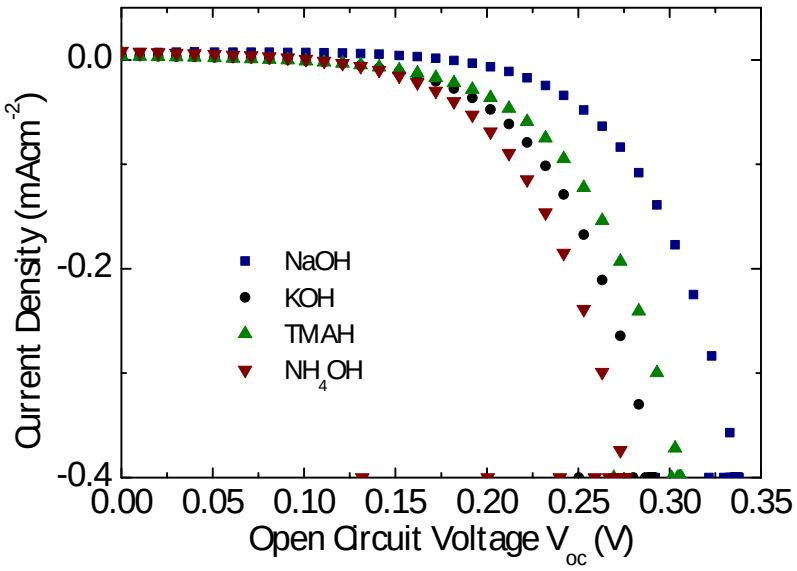

(a)

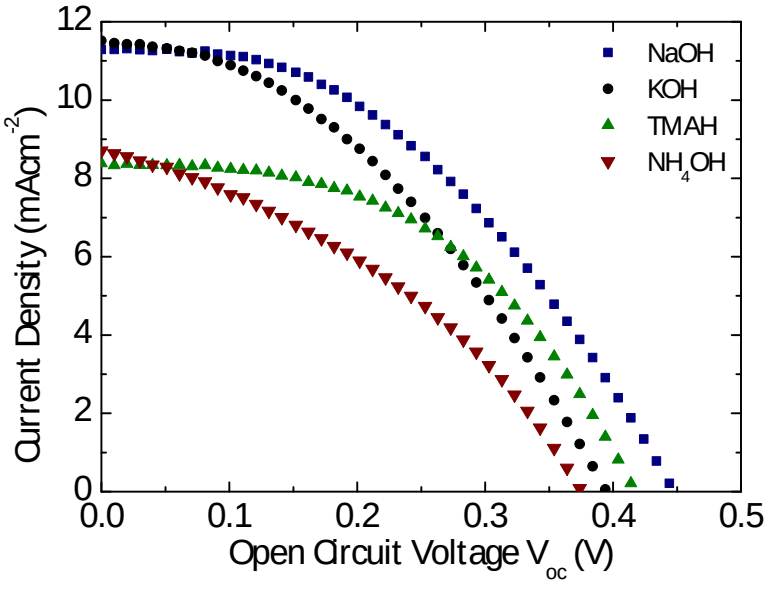

(b)

Figure 7.2: Current-voltage characteristics of abP065. (a) shows the dark current, (b) the behavior under illumination.

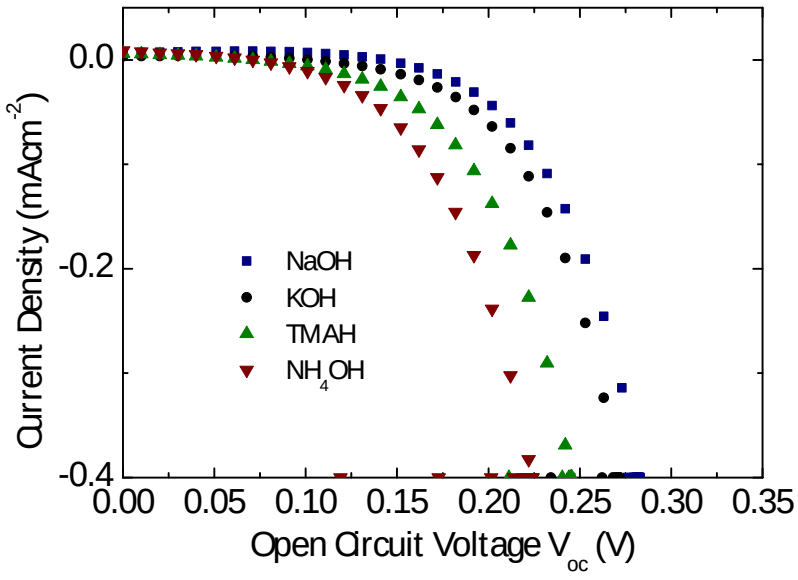

(a)

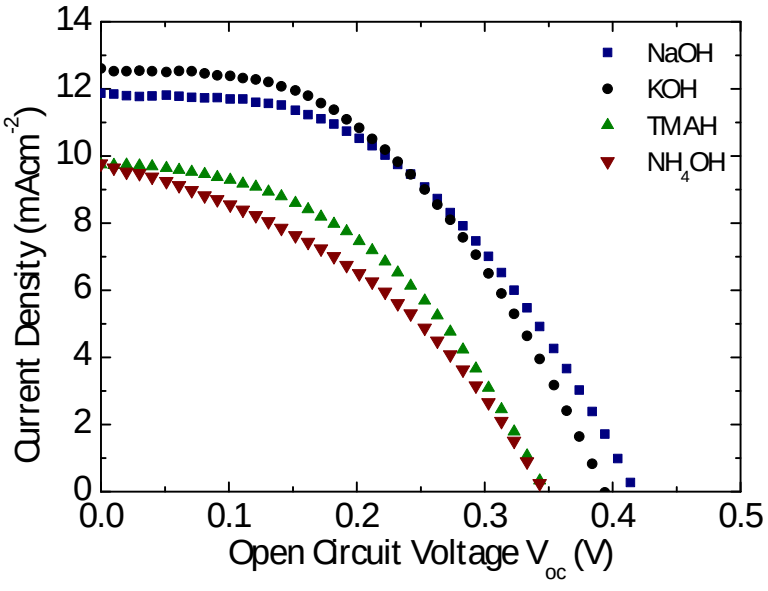

(b)

Figure 7.3: Current-voltage characteristics of abP070-2. (a) shows the dark current, (b) the behavior under illumination.

List of Figures

List of Tables

List of Publications

[1] **A. Birkel**, N. Loges, E. Mugnaioli, R. Branscheid, D. Koll, M. Panthöfer, S. Frank, and W. Tremel "Interaction of Alkaline Metal Cations with Oxidic Surfaces: Effect on the Morphology of SnO_2 Nanoparticles." *Langmuir*, 26(5):3590-3595, 2010.

[2] **A. Birkel**, A. A. Mikhailovsky and A. K. Cheetham "Infrared to Visible Upconversion Luminescence Properties in the System Ln_2BaZnO_5 (Ln = La, Gd)." *Chemical Physical Letters*, 477(4-6):325-329, 2009.

[3] **A. Birkel**, F. Reuter, D. Koll, S. Frank, R. Branscheid, M. Panthöfer, E. Rentschler and W. Tremel "The Interplay of Crystallization Kinetics and Morphology during the Formation of SnO_2 Nanorods: Snapshots of the Crystallization from fast Microwave Reactions " *submitted.*

[4] S. Frank, L. Steidl, S. A. L. Weber, M. Panthöfer, **A. Birkel**, D. Koll, R. Berger, W. Tremel and R. Zentel "Electrodeposition of ZnO Nanorods on Opaline Replica as Hierarchically Structured Systems" *submitted.*

[5] **A. Birkel**, Y.-G. Lee, D. Koll, X. Van Meerbeek, S. Frank, M.-J. Choi, Y.-S. Kang, K. Char and W. Tremel "Fast Microwave-assisted Synthesis of SnO_2 Nanoparticles and their Application in Dye-Sensitized Solar Cells" *in preparation.*

[6] C. S. Birkel, T. Claudio, M. Panthöfer, **A. Birkel**, D. Koll, G. Kieslich, J. Schmidt, R. Hermann, and W. Tremel "Compaction of Nanostructured $Zn_{1+x}Sb$ by Spark Plasma Sintering and Characterization of Obtained Pellets." *in preparation.*

[7] C. S. Birkel, T. Claudio, D. Bessas, M. Schwall, M. Panthöfer, **A. Birkel**, D. Koll, G. Kieslich, C. Felser, J. Schmidt, R. Hermann, and W. Tremel "Compaction of Nanostructured $FeSb_2$ by Spark Plasma Sintering and Characterization of Obtained Pellets" *in preparation.*

So: Feierabend, Emma!

Lukas, der Lokomotivführer